IMPROVED MODELING OF ROTARY
MOMENTUM MASS TRANSPORT EQUIPMENT

Fredrik Nyholm

Master's Thesis

Supervisor: Frank Pettersson

Laboratory of Process and Systems Engineering

Faculty of Science and Engineering

Åbo Akademi University

June 2020

Aut viam inveniam

aut faciam

Abstract

Pumps, compressors and turbines are vital parts of any process plant. Thus, accurate modeling of these machines is crucial for a dynamic process simulator, especially if the simulator is used for operator training. The operation of the machines is usually described by operating curves provided by the manufacturer, but these are strictly valid only for the set of process conditions they were created for. Accurately predicting the performance of the machines outside of the design conditions can be a challenging endeavor.

ProsDS is a software used by NAPCON to construct operator training simulators. In order to improve the performance of the compressors in these simulators, a new dynamic model for a centrifugal compressor was developed in ProsDS during the course of this thesis. The developed model was based on dimensionless operating curves defined by the head coefficient and the exit flow coefficient. Simple calculation of the outlet temperature and power consumption was also included.

The stability of the developed model was verified by dynamic ramp tests of the operating conditions. Furthermore, the accuracy of the developed model was determined by performing process data tests. The results were promising and, in most cases, an improvement from the performance of the currently implemented model, although some further development of the new model is needed to reach a fully acceptable accuracy of the performance.

Table of Contents

Preface

This thesis was carried out as a collaboration between the NAPCON business unit of Neste Engineering Solutions Oy and the Thermal and Flow Engineering subject at the Laboratory of Process and Systems Engineering of Åbo Akademi University. While this work took its time to finish and seemed rather challenging at times, it was definitely an interesting and educational endeavor.

Firstly, I would like to thank NAPCON for offering this interesting topic for a thesis, which combined both theoretical aspects and practical application and included cooperation between several of the company's disciplines. My deepest gratitude goes to my supervisor, Docent Frank Pettersson, for his interest in this thesis, for impeccable practical facilitation of my work and for always having his door open for discussing both the thesis and a plethora of completely different topics. I also want to extend my thanks to my instructors from NAPCON, M.Sc. Teemu Saarinen and M.Sc. Niina Turunen, for their regular support and guidance during the entire process, despite their busy schedules.

I also wish to thank Docent Leif Hammarström for clarifications regarding the current implementations of the pump and compressor models in ProsDS as well as general insights on the modeling of these machines, M.Sc. Teemu Liikala for help with formulating the compressor calculations in Lisp and implementation in ProsDS and M.Sc. Juha Lauttamus for input from an equipment design point of view, as well as for providing equipment data for the compressors. Without their help this thesis would have turned out quite differently and certainly taken a lot longer to finish.

Lastly, I would like to thank my family for their continuous support and my fellow students for making my time at Åbo Akademi the unforgettable journey it turned out to be.

Fredrik Nyholm
Turku, Midsummer's Eve 2020

Nomenclature

Roman

Notation	Description
A	Efficiency coefficient varying with Mach number
B	Efficiency coefficient varying with Mach number
C	Specific heat capacity
CV	Valve flow coefficient
D	Outer diameter
E	Efficiency coefficient varying with Mach number
F	Form loss coefficient
H	Head
I	Number of impeller blades
K	Stodola coefficient
M	Mach number
MW	Molecular weight
N	Impeller speed
$NPSH$	Net positive suction head
P	Power
R	Universal gas constant
Rxn	Stage reaction
S	Suction specific speed
SG	Specific gravity

T	Temperature
U	Impeller tip speed
V	Volume
W	Work
X	Generalized compressibility function
Y	Generalized compressibility function
Z	Compressibility
a	Sonic speed
b	Width of fluid element, impeller blade height
d	Diameter
f	Leakage factor
g	Gravitational acceleration
h	Specific enthalpy
k	Hub narrowing
m	Polytropic temperature exponent
n	Polytropic exponent, polytropic index
p	Pressure
r	Radius
s	Work input factor
u	Velocity
v	Specific volume
x	Fraction
z	Height

A single dot accent over a variable denotes a flow, e.g. $\dot{V}$ for volumetric flow rate.

Greek

Notation	Description
ΔH	Enthalpy difference
Δh	Specific enthalpy difference
Δp	Pressure difference
Δs	Empiric correction parameter
Δz	Difference in elevation
Π	Pressure ratio
Ω	Impeller speed in rad/s
α	Vane angle
β	Angle between impeller blade tip and the tangent to the direction of its motion
γ	Polytropic co-efficient
η	Efficiency
κ	Ratio of specific heats, isentropic exponent
ξ	Mole
ρ	Density
σ	Critical cavitation number
φ	Flow coefficient
ψ	Head coefficient
ω	Angular velocity

Subscripts

Notation	Description
0	Absolute, surrounding
1	Inlet
2	Impeller exit
3	Outlet
A	Actual
L	Leakage
R	Required
RP	Rated point
S	Specific
T	Temperature
V	Volume
ad	Adiabatic
avg	Average
c	Choke point
corr	Correction
e	Electric
ent	Entropic
f	Friction
i	Input
inc	Inception
init.circ.	Initial circulation test case

int	Internal
is	Isentropic
l	Liquid phase
m	Molar
mech	Mechanical
max	Maximum
mcorr	Quantity related to the polytropic temperature exponent correction factor
min	Minimum
new	New state
p	Polytropic
peak	Point of peak efficiency
rated	Rated test case
ref	Reference state
rel	Relative
s	Suction
scaled	Scaled quantity
shaft	Machine shaft
surge	Condition at surge
steam	Steam phase
t	Tangential
u	Impeller tip speed
v	Virtual, vane
vap	Vapor

1 Introduction

NAPCON, a business unit of Neste Engineering Solutions, offers a dynamic, high fidelity process simulator as a part of their product portfolio geared towards revealing and utilizing the untapped potential of the customer's production, processes and professionals. The simulator is highly interactive, providing a safe yet intriguing training environment for the process operators. [1] The simulator is based on an in-house software called ProsDS, which is programmed in ANSI Common Lisp.

Pumps and compressors are a vital part of the processes of the manufacturing industry, which is demonstrated by the fact that around 60-65% of energy consumed by industry is used by machines driven by electric motors, many of which are pumps or compressors. [2, p. 28] [3, p. 534] Depending on the industry sector, some 12% (non-ferrous metal) to 63% (pulp and paper) of the consumed electricity is used by pumps, fans and compressors. [4, pp. 41, 59, 73, 88, 104, 116, 129, 146] Thus, accurate modeling of these machines is required in order to study startup, shutdown and capacity adjustment situations in the processes.

The driving force for this work from the company's side is precisely to make the process simulations more realistic by improving the modeling of rotary equipment such as pumps, compressors and turbines, and matching their function to real-world operations. It is seen as important to study both steady-state and dynamic simulation methods and apply these to a large operation regime in the dynamic simulation environment. Performance issues and typical fault scenarios of the mentioned equipment are also a point of interest for the company, to the extent needed in the operator training simulator. Equipment performance curves, local operations and other equipment parameters are expected to be analyzed and then implemented in the rotary equipment modeling in ProsDS. [5]

During initial discussions with the instructors the scope was limited so that literature studies of the pumps, compressors and turbines would be conducted. A model of the compressor would be constructed by using existing modeling options in ProsDS and tested in the simulator, later to be implemented to the source code by the software development team. Interest in the operation during shut-down, start-up and other peculiar operating points was again brought up, as was interest in the effect of variations in the rotation speed of the equipment. [6]

In order to acquire more specific details of the need for improvement, the simulator trainers at Neste were also interviewed. In their experience, the machines function in a decent manner when operated close to their design points. It had been noted that the temperatures behaved in an odd manner, rising too quickly. This issue was pronounced for piston machines, but also occurred for centrifugal machines. An interest in modeling of compressor surge and the improvement of the effects of changes in the composition of the compressed gas was mentioned. [7]

For further insights into the behavior of pumps and compressors, a senior process specialist at Neste was consulted. The differences between the operating curves of pumps and compressors, effect of rotating speed on the curves, limits for surge and stonewall for compressors, the affinity laws, net positive suction head curves and cavitation curves for pumps were suggested as subjects for further study. It was recommended that the focus remain on the operating curves and their behavior. [8]

2 Theory

In this chapter the theory behind the operation of pumps and compressors, along with some notes on the construction and classification of the machines, is presented. Focus lies on the centrifugal machines, the operating curves and their dependence on the operating conditions and affinity laws. Turbines are only briefly covered here, as they are rather shallowly dealt with in the studied chemical engineering literature. The reader would be well advised to look for a more in-depth review of the turbines in literature regarding the energy technology sector.

2.1 Pumps

Pumps are machines used for transport of liquids. The pumps are used in several different applications, ranging from administering small, accurately controlled flows of catalyst to reactors, to supplying processes with massive amounts of cooling water. The characteristics of the pumped fluids may also vary significantly, ranging from low viscous fluids to slurries of a non-Newtonian nature. This imposes a plethora of requirements on the pumps and, as a consequence, several different types of the machines have been developed. [9, p. 379]

Pumps can be divided into two main categories, namely centrifugal and piston, with other types of pumps considered as special cases. [10, p. 1] A more general classification system is the division into dynamic and displacement machines. In a dynamic pump energy is continuously added to increase the fluid velocity. As the velocity decreases at discharge, a pressure increase is produced. In displacement pumps energy is periodically added to a moveable boundary of an enclosed volume containing the fluid, resulting in a pressure increase. Dynamic pumps can be further divided into centrifugal and several special effect pumps, while displacement pumps are divided into reciprocating (e.g. piston and diaphragm pumps) and rotary (e.g. gear and lobe pumps). [11, pp. 1.2-4]

For positive displacement pumps, such as piston pumps, the delivered liquid volume is directly related to the piston displacement and directly increases with the revolution speed. It is not largely affected by the pressure or the properties of the pumped liquid. The liquid properties, such as viscosity, density and vapor pressure, as well as the type of liquid (Newtonian or non-Newtonian, single or multiple phase etc.), strongly influence the function of the centrifugal

pumps. These machines are also strongly influenced by the properties of the solids in a slurry. [9, p. 380]

The reciprocating pumps are typically used in applications that require higher pressures, while centrifugal pumps are used to deliver high volumetric flows. [11, p. 1.5] The majority of the pumps used in the chemical and petroleum industries are of the centrifugal type and of all pumps the centrifugal pumps account for 80%. [9, p. 379] [11, p. 9.101] [2, p. 28] Thus, the theory presented here will focus on centrifugal pumps.

The centrifugal pump consists of a casing, a vaned impeller, an inlet and an exit connecting the pump to the suction and discharge side piping. As Figure 1 shows, the liquid from the impeller may be discharged directly into a volute, which is a chamber gradually increasing in cross section with a tangential outlet. The impeller can also be surrounded by a diffuser ring, consisting of static guide vanes. The diffuser allows for a less abrupt change in the flow direction of the fluid, resulting in a more efficient conversion of the kinetic energy. [9, p. 397]
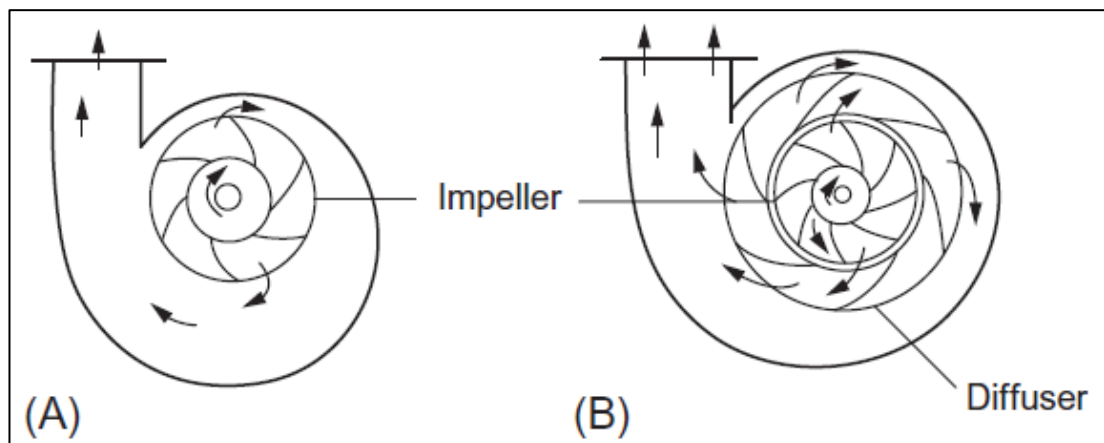

Figure 1. Centrifugal pump with a volute (A) and a diffuser (B). [9, p. 397]

The fluid is fed to the pump through the center of the rotating impeller, from where it is picked up by the impeller blades and thrown outward by centrifugal action. The liquid thus acquires a high kinetic energy, which is converted to potential energy in the form of a pressure difference between the suction and discharge side, as the flow velocity at the exit decreases. The tip angles of the impeller vanes are a central factor for the operating characteristics of the pump. The required vane angle in the diffuser is dependent on the volume flow, impeller rotation speed and impeller blade angles. The maximum operational efficiency is thus achieved only in a narrow range of conditions. [9, p. 397]

4

2.1.1 Performance map

The pressure rise delivered by the pump is commonly referred to as "head" and is usually given in bar or as meters of water column (i.e. the height the pump can raise water to). Virtual head H_v, also known as the ideal head or Euler head, is the head that would be gained if the fluid velocity at impeller exit would be exactly parallel to the blades. It is related to the actual input head H_i by Equation 1, where η_v is the vane efficiency. [12, p. 88]

$$H_i = \eta_v H_v \tag{1}$$

H_v is given by Equation 2, where r_2 is the impeller radius, ω is the angular velocity, g is the gravitational acceleration, $\dot{V}$ is the volume flow rate and b is the width of the fluid element. The angle β is the angle between the impeller blade tip and the tangent to the direction of its motion, as shown by Figure 2, where u_v is the velocity of the liquid relative to the vane, u_t is the tangential velocity of the vane tip and u_2 is the combination of these two (i.e. the velocity of the liquid). [9, pp. 398-400]

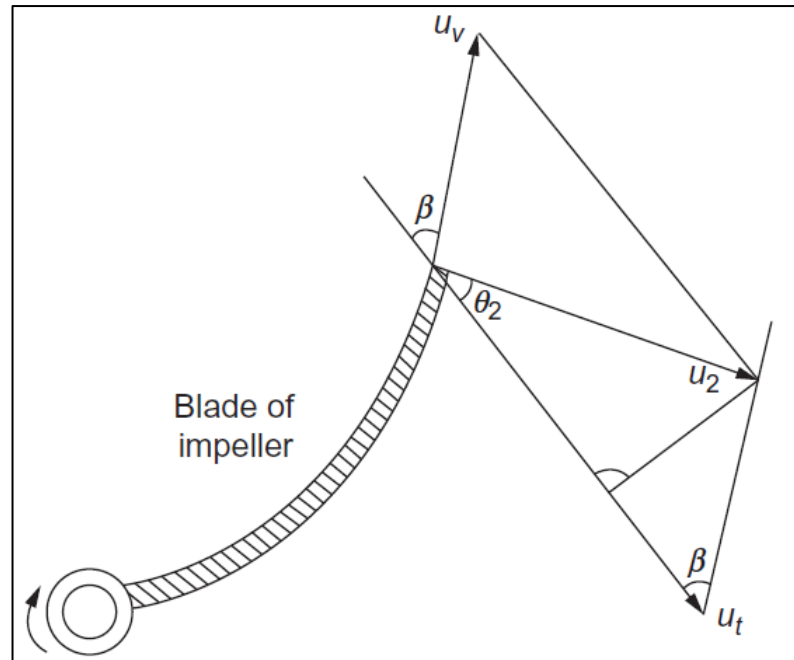$$H_v = \frac{r_2^2 \omega^2}{g} - \frac{\dot{V}\omega}{2\pi bg \tan \beta} \tag{2}$$

Figure 2. Velocity diagram. [9, p. 398]

The developed virtual head is proportional to the square of the radius and angular speed, while being independent of the density of the liquid. The pressure will thus be directly proportional to the density, following from Stevin's law, Equation 3, where p is pressure, ρ is density, and z is height (or here, head). For a given speed of rotation, there is a linear relation between the head developed and the volume flow rate. [9, pp. 398, 400]

$$p = \rho g z \tag{3}$$

The output of a pump is a function of its linear dimensions, the shape, number and arrangement of impellers, angular speed and the head against which it is operating. The specific speed N_s of a pump is given by Equation 4, and is a constant for geometrically similar pumps. Some other forms of the expression also exist, but this one is dimensionless. A typical form is to replace the angular speed ω with the impeller speed N, given in rpm. If the flowrate is given in US gallons per minute and the head in feet, the specific speed for a centrifugal pump frequently assumes values between 400 and 10 000, depending on the type of impeller. The specific speed may also be useful for indicating whether a single-stage pump is sufficient or not. For values below 1 000, the efficiency for a single-stage pump is low and multi-stage pumps should be considered. In general, a low specific speed results in low capacity and high specific speed in high capacity. [9, pp. 401-402] [13, pp. 200-201] [14, pp. 10.22-32]

$$N_s = \frac{\omega \dot{V}^{1/2}}{(g H_i)^{3/4}} \tag{4}$$

Equations 1 to 4 can then be used to calculate the produced head and pressure increase and to map their dependence of the volume flow. The characteristics of a pump are usually displayed in a plot with the head H, power P and efficiency η against the flow Q, as seen in Figure 3. The optimum operation condition is at the duty point, where the vertical line through maximum efficiency cuts the head curve. The efficiency remains reasonably constant when the pump is operating near optimum conditions. [9, pp. 402-403]
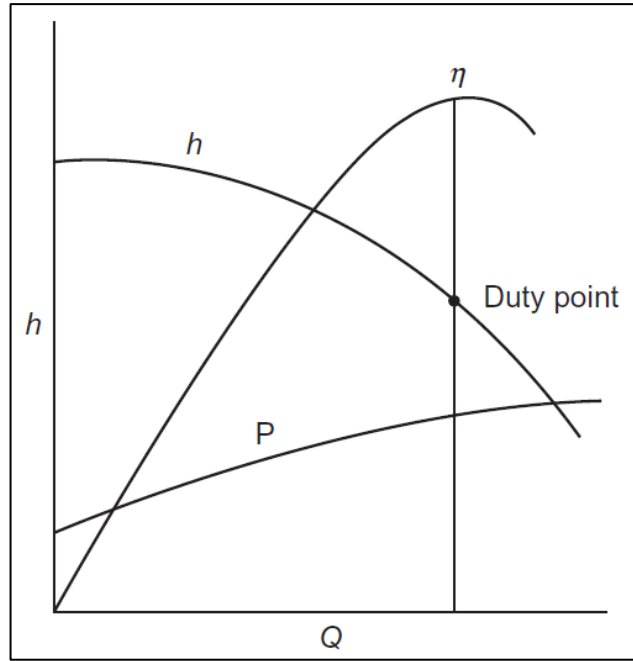
Figure 3. Plot of pump characteristics. [9, p. 402]

The so-called fan laws, also known as the affinity laws, can be used to recalculate the pump characteristics for different operating conditions and to calculate the characteristics for geometrically similar pumps. The laws take into account changes in angular speed, impeller diameter *d* and fluid density. Indices *ref* and *new* refer to the initial and the new condition, respectively. The new pressure difference is given by Equation 5, Equation 6 describes the new volume flow rate, while Equations 7 and 8 describe the new power and efficiency of the pump. [15, pp. 117-118] Equations 5 and 6 give an accurate approximation for the new pressure and flow rate, but Equations 7 and 8 give somewhat inaccurate approximations for the power and efficiency. [16]

$$\Delta p_{new} = \left(\frac{\omega_{new}}{\omega_{ref}}\right)^2 \left(\frac{d_{new}}{d_{ref}}\right)^2 \frac{\rho_{new}}{\rho_{ref}} \Delta p_{ref} \tag{5}$$

$$\dot{V}_{new} = \frac{\omega_{new}}{\omega_{ref}} \left(\frac{d_{new}}{d_{ref}}\right)^3 \dot{V}_{ref} \tag{6}$$

$$P_{new} \approx \left(\frac{\omega_{new}}{\omega_{ref}}\right)^3 \left(\frac{d_{new}}{d_{ref}}\right)^5 \frac{\rho_{new}}{\rho_{ref}} P_{ref} \tag{7}$$

$$\eta_{new} \approx \eta_{ref} \tag{8}$$

As can be seen from the affinity laws, the capacity and head for the same pump can be related to each other as in Equation 9. This means the head will change as the square of the liquid flow. [14, pp. 10.22-32]

$$\frac{\dot{V}_{new}^2}{\dot{V}_{ref}^2} = \frac{\Delta p_{new}}{\Delta p_{ref}} \qquad (9)$$

2.1.2 Cavitation

Should the pressure of the pumped liquid fall below its vapor pressure at any point in the pump, the liquid will start to vaporize. This is called cavitation. The phenomenon affects the process in three negative ways, namely by causing noise and vibration, damaging the process equipment and reducing the flow. The vaporization causes the density of the liquid-vapor mixture to decrease, leading to a reduction in the transport capacity of the pump. The vapor may also form pockets of gas. As these pockets collapse they send shockwaves through the fluid, which can rapidly cause mechanical damage to the pump. There are several ways to reduce cavitation and mitigate its negative effects. For example, damage to the equipment can be reduced by using harder materials in the construction and by directing the cavitating stream away from the walls. Careful attention must, thus, be paid when designing the pump, to make sure the minimum pressure that will arise at any point in the pump remains above the vapor pressure at the pumping temperature. [9, p. 404] [15, p. 129] [14, pp. 8.72-73]

The required net positive suction head $NPSH_R$, expressed as head of the liquid to be pumped, describes by how much the pressure at the suction point of the pump must exceed the vapor pressure at the pumping temperature in order to avoid cavitation. It is a function of the design parameters of the pump, such as characteristics of the liquid, total head, impeller speed, pump capacity and impeller design. $NPSH_R$ is given by the manufacturer as a curve relating it to capacity and impeller speed. As a rule of thumb, the $NPSH$ should be above 3m for capacities up to 100 m3/h and 6m beyond this capacity. The available net positive suction head $NPSH_A$ is calculated with Equation 10, where p_0 is the absolute pressure in the liquid reservoir, p_{vap} is the vapor pressure, z_0 is the height of the liquid level above the suction point and z_f is the head lost to friction. Here it is assumed that the liquid kinetic head can be converted to pressure head. The system must be designed so that $NPSH_A$ is greater than $NPSH_R$ during all operating conditions. An adequate margin for design can be obtained from Equations 11 and 12, using

the larger of the calculated values for $NPSH_A$. The required $NPSH$ depends on the pumped fluid, and, since water is considered as the standard fluid, various correction methods have been developed for evaluating $NPSH_R$ for other fluids. One such method is presented in Figure 4, where a reduction in $NPSH$ is displayed for various fluids over different temperatures and vapor pressures. The data displayed is for pure liquids and extrapolation outside of the shown ranges is likely inaccurate. [9, pp. 404-406] [13, p. 212] [14, pp. 10.22-32]

$$NPSH_A = \frac{p_0 - p_{vap}}{\rho g} + z_0 - z_f \tag{10}$$

$$NPSH_A = NPSH_R + 1.524 \, m \tag{11}$$
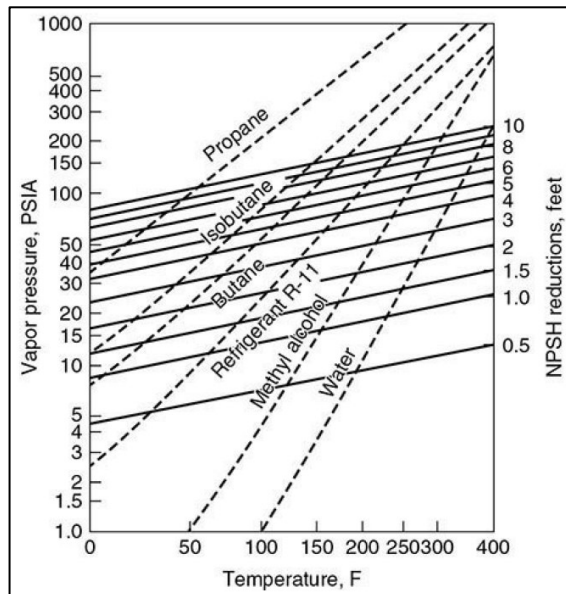
$$NPSH_A = 1.35 \times NPSH_R \tag{12}$$

Figure 4. Estimation of *NPSH* for various fluids. [14, pp. 10.22-32]

As previously mentioned, the limit for the onset of cavitation can also be monitored by directly studying the pressure at the suction side, as shown by Equation 13. Here p_s is the pressure at the suction side and $p_{s,min}$ is the minimum allowable suction pressure. The minimum pressure is described by Equation 14, where Δp_s is a characteristic value for every pump and is influenced by the rotation speed. [15, p. 129] This value may be given by the manufacturer, or it can be evaluated using Equation 15, where k is the hub narrowing and S is the suction specific speed. Note that the impeller speed has the unit $\frac{1}{min}$ here, the volume flow is in $\frac{m^3}{s}$. The hub narrowing is given by Equation 16, where d_n is the hub diameter of the impeller inlet and D_s is the outer diameter of the impeller inlet. [10, pp. 189, 195] The suction specific speed is useful in evaluating the suction limitations of the pump. It is either given by the manufacturer

or calculated with Equation 17. If S is not readily given by the manufacturer, it may be easiest to just use *NPSH*, as calculating S requires knowing *NPSH*. [11, p. 2.15] [14, pp. 10.22-32]

$$p_s > p_{s,min} \tag{13}$$

$$p_{s,min} = p_{vap} + \Delta p_s \tag{14}$$

$$\Delta p_s = \left(\left(\frac{\omega}{100}\right)^2 \frac{\dot{V}}{kS}\right)^{2/3} \tag{15}$$

$$k = 1 - \frac{d_n^2}{D_s^2} \tag{16}$$

$$S = 51.65 \times \frac{\omega \dot{V}^{1/2}}{NPSH^{3/4}} \tag{17}$$

Several dimensionless numbers for studying the inception of cavitation exist in the literature. For cavitation in a fluid flow a critical cavitation number at inception of cavitation, σ_{inc}, can be defined according to Equation 18, where u is the flow velocity. The number is characteristic for each piece of equipment and can be used to correlate equipment performance data. [14, p. 6.41]

$$\sigma_{inc} = \frac{p_s - p_{vap}}{\rho u^2 / 2} \tag{18}$$

For rotating equipment, the inlet tip velocity is often used instead of u. Perhaps more common for these types of machines is the use of inception suction specific speed S_{inc}, as defined by Equation 19, where Ω is the impeller speed in rad/s. This number represents the critical value for the suction specific speed at which cavitation first appears and is similar in concept to the critical cavitation number. Using the inception suction specific speed, it is possible to determine if the pump is operating under conditions close to cavitation. [17, pp. 278-279]

$$S_{inc} = \frac{\Omega \dot{V}^{0.5}}{\left(\frac{p_s - p_{vap}}{\rho}\right)^{0.75}} \tag{19}$$

2.1.3 Power consumption

The work required for pumping a liquid is given by Equation 20, where Δz is the difference in elevation, Δp is the pressure difference in the system, and Δp_f is the pressure drop due to losses. The shaft work required for the reversible process is given by Equation 21. A negative W indicates the need of a pump, whereas a positive value means a turbine could be used to extract energy. The head required from the pump is calculated with Equation 22. [13, pp. 206-207] [14, p. 4.10]

$$W = g\Delta z + \frac{\Delta p}{\rho} - \frac{\Delta p_f}{\rho} \tag{20}$$

$$W_{shaft} = \frac{\Delta p}{\rho} \tag{21}$$

$$H = \frac{W}{g} \tag{22}$$

As can be seen the energy required by the pump depends on the raised height of the fluid, pressure required at delivery point, flow resistance of the pipe, flow rate and the physical properties of the liquid (particularly density and viscosity). [9, p. 379] Increase in the viscosity of the fluid will increase the power required for generating the same head at the same flow rate, while lowering the efficiency of the pump. [14, pp. 10.22-32] Power developed by the pump is given by Equation 23, where $\dot{m}$ is mass flow. [9, p. 399]

$$P = \dot{m}H_v g \tag{23}$$

The power consumed by the pump when pumping an incompressible fluid is given by Equation 24, where Δp is the pressure difference developed by the pump. The total efficiency of the pump η is given by Equation 25, where η_{mech} is the mechanical efficiency of the pump and η_{int} is the pump's internal efficiency. [15, p. 110] [13, p. 480] If the work required by the pump is known, or if it is calculated from the produced head, the power consumed can be calculated with Equation 26. [13, p. 207]

$$P = \frac{\dot{V}\Delta p}{\eta} \tag{24}$$

$$\eta = \eta_{mech}\eta_{int} \tag{25}$$

$$P = \frac{W\dot{m}}{\eta} \tag{26}$$

2.2 Compressors

Compressors are in many ways similar to pumps. Both machines are used to transport fluids and, thus, share many similarities in both working principles and mechanical components. Same as for pumps, the basic division of compressors is also into displacement and dynamic machines. The displacement machines are constant volume, variable head compressors. They are not largely affected by the characteristics of the gas and, as the displacement pumps, are in general used for low flows or low molecular weight gases. Dynamic compressors are variable volume, constant energy machines. Contrary to displacement machines, they are significantly influenced by gas characteristics. Dynamic machines are typically used whenever possible, due to their lower maintenance costs. The dynamic machines can be divided into axial and centrifugal compressors. In this work, the focus lies on the centrifugal variant. [18, pp. 7-21]

The centrifugal compressor and centrifugal pump share the same central mechanical parts. The compressor consists of an impeller inside a casing, an inlet leading the gas to the impeller and an exit leading out from the volute surrounding the impeller. The impeller may also be surrounded by a vaned diffuser, but the diffusers in the machines used in the oil refining and petrochemical industries usually come without vanes. If the machine consists of multiple compression stages, the gas is led from the exit, through deswirling vanes, into the inlet of the next impeller. The energy of the gas is increased by increasing its speed, which is done by the impeller. The diffuser and volute then convert the speed to a pressure and temperature increase by efficiently reducing the fluid velocity. [14, p. 10.22] [18, pp. 21-22] [19, pp. 12-13] [20, pp. 41-43]

The compressor is characterized by its performance map, where the produced head (or discharge pressure), efficiency and required power are plotted against the inlet volume flow. The manufacturer usually provides a number of performance maps valid for varying inlet conditions.

The compressor has an operating range defined between the surge point and choke point. The surge point is the lower flow limit of stable operation and, at this point, the flow is reversed in the machine. When this occurs, all the forces acting on the compressor are reversed. In the worst case, this can lead to total destruction of the machine. At the choke point, or stonewall, the fluid flow reaches Mach 1, meaning the flow velocity is as high as the speed of sound in the fluid. At this point, the maximum flow through the unit at the current operating conditions has been reached. The choke condition causes a considerable drop in efficiency but does not

cause damage to the machine. The operating range decreases if the pressure ratio per stage or the number of stages is increased. [14, pp. 10.37-52]

2.2.1 Performance map

Transport of gases in pipes mainly follows the same theory as transport of liquids. The density of the gas, however, is often only a fraction of the density of the fluids. More importantly, it can also be heavily influenced by both the pressure and the temperature of the gas. This leaves its mark on the design and operation of gas transport equipment. The density of a gas can be calculated with Equation 27, where Z is the compressibility, R is the universal gas constant and MW is the molecular weight of the gas. [15, p. 136] When the desired pressure increase is so large a compressor is needed, the fluid can no longer be treated as incompressible. Instead, the changes in the thermodynamic state of the fluid must be considered when studying the machine. [15, p. 141]

$$\rho = \frac{MWp}{ZRT} \qquad (27)$$

Due to the variance in density for the gases, it is not practical to give the head developed by the compressor as meters of fluid column. Instead, it is commonly defined as the energy it takes to compress and deliver the gas from one energy level to the next and is given in Joule per kilogram. Additionally, the isothermal, isentropic (adiabatic) and polytropic compression processes all have their own corresponding heads and efficiencies. [18, pp. 53-54] Both the isothermal and isentropic curves can be regarded as idealized boundary cases. [15, pp. 142-146] As can be seen from Figure 5 and Figure 6, the polytropic curve lies to the right of both the isothermal and the isentropic curves. As the polytropic head also is an ideal reversible compression path, the actual compression curve lies still to the right of the polytropic curve, as seen in Figure 5. Notwithstanding this fact, of the presented curves the polytropic one is the best description of the actual compression curve. Figure 7 displays an approximation of the relative sizes of the isothermal, isentropic and polytropic heads. [18, p. 62]
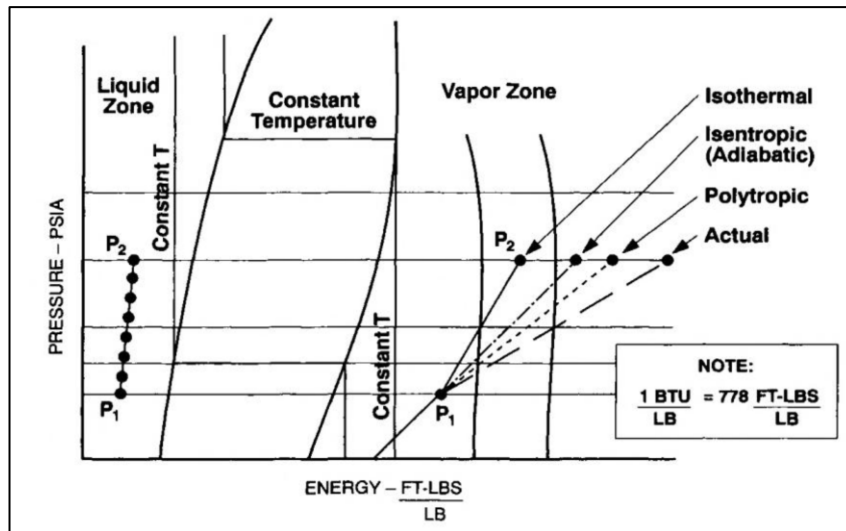
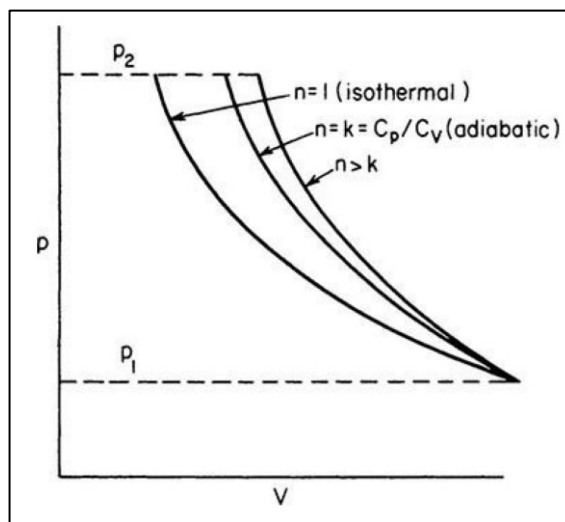Figure 5. Mollier diagram displaying the various compression processes. [18, p. 59]

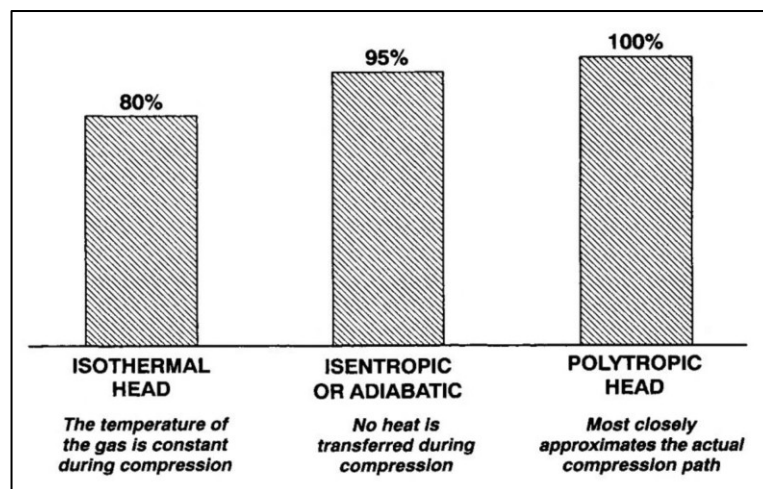Figure 6. Compression curves. [14, pp. 10.37-52]

Figure 7. Relative values of compression heads. [18, p. 60]

Most compressors operate along a polytropic curve approaching the adiabatic curve. The adiabatic curve is often used as a basis for compressor calculations, but as the polytropic head contains an efficiency term it is the one most used by the equipment manufacturers. [14, pp. 10.37-52] [18, p. 62] The adiabatic head is given by Equation 28 and the polytropic head is given by Equation 29, where the ratio of specific heats κ has been replaced by the polytropic index n and the average value of the inlet and outlet compressibility Z_{avg} is used. The polytropic efficiency, defined as the ratio of the polytropic work to the actual work required, is given by the ratio of the fractions containing κ and n, as shown by Equation 30. [13, p. 852] [14, pp. 10.37-52] [21, p. 103] Here, κ is the ratio of specific heats, given by Equation 31. C_p is the specific heat capacity of the fluid at constant pressure and C_V is the specific heat capacity at constant volume. [9, p. 40] As shown in Appendix E, the compressibility Z can be calculated with Equation 32, where V_m is the molar volume of the gas.

$$H_{ad} = ZRT_1 \frac{\kappa}{\kappa-1} \left(\left(\frac{p_3}{p_1}\right)^{(\kappa-1)/\kappa} - 1 \right) \tag{28}$$

$$H_p = Z_{avg} T_1 \frac{R}{MW} \frac{n}{n-1} \left(\left(\frac{p_3}{p_1}\right)^{(n-1)/n} - 1 \right) \tag{29}$$

$$\eta_p = \frac{(\kappa-1)/\kappa}{(n-1)/n} \tag{30}$$

$$\kappa = \frac{C_p}{C_V} \tag{31}$$

$$Z = \frac{pV_m}{RT} \tag{32}$$

In the industry, the compressors are monitored to follow up their performance and to reduce downtime and maintenance costs. This monitoring is often done by comparing process data from measurements to some form of simulation model. [20, p. 16] [22] Simulations can also be used for compressor system design. Dynamic simulators can be used to train process operators. Such simulations require a high-fidelity model of the compressor, of which the performance maps are a key component. The performance maps provided by the manufacturer, however, are only valid at the specific suction conditions and rotation speeds they were constructed for. [23] Thus, in order to model the whole operating range of the compressor, a method for predicting the performance maps for varying operating conditions is needed.

The affinity laws presented in Equations 5 to 8, also known as the fan laws, can be used for a crude approximation, but their accuracy significantly decreases as the molecular weight of the gas and the number of compression stages in the machine increase. As the compressors do not strictly follow the affinity laws, some modified version of the equations is needed for a proper prediction. [18, p. 72] [23] Several alternatives of varying complexity and accuracy for predicting the performance are available.

In general for compression and expansion, if the process follows an isothermal path, the product of the pressure and volume is constant, as shown in Equation 33. If the compression is polytropic, an exponent n is added, yielding Equation 34. The exponent n is the polytropic index and it takes a different value depending on the process conditions and the design of the machine. [13, pp. 81-82]

$$pV = constant \qquad (33)$$

$$pV^n = constant \qquad (34)$$

Like for the pump, the flow characteristics of the compressor can be described by certain dimensionless numbers. The specific speed N_S, similar to the suctions specific speed S for the pumps, describes the relation of the adiabatic head to the flow rate at various rotating speeds in geometrically similar machines. It is given by Equation 35. Another useful number is the specific diameter d_S, which describes the relation of the head and flow rate at various impeller diameters, according to Equation 36. [14, pp. 10.37-52]

$$N_S = \frac{\omega \dot{V}^{1/2}}{H_{ad}^{3/4}} \qquad (35)$$

$$d_S = \frac{H^{1/4} d}{\dot{V}^{1/2}} \qquad (36)$$

In dynamic simulation the machine is subjected to a wide range of operating conditions and, thus, the operating curve of the machine should be scaled smoothly in a user-friendly manner to match the governing conditions, while maintaining a sufficient accuracy of the predicted performance. As directly scaling the performance curves with the affinity laws is not viable for compressors, approaches that consider the vital machine and operating condition parameters influencing the compressor performance are needed for an accurate prediction of new performance curves. One option is the computationally heavy CFD simulation of the machine. Another approach would be to utilize empirical correlations for the predictions. However, both methods require detailed information of the machine geometry, which often is not readily available.

A third alternative is to convert the performance curve to a dimensionless form, from which performance curves at new operating conditions can be predicted. Here the head is converted into the head coefficient ψ. For the volume flow either the inlet flow coefficient φ_1 or the exit flow coefficient φ_3 is used. Using the inlet flow coefficient, an array of dimensionless curves is obtained and, as the impeller tip speed Mach number varies, the needed dimensionless curve can be interpolated or extrapolated from the curve array and the converted back to the sought performance curve in natural scale. The aim of utilizing the exit flow coefficient is to obtain a single dimensionless performance curve for the compressor, which can then be used to calculate all the curves in natural scale. The inlet flow coefficient is described as more of an external characteristic, while the exit flow coefficient is an internal component of the compressor. The advantage with both methods is that only the manufacturer performance curves, impeller diameter and blade tip height and knowledge of the governing process conditions are needed for the predictions. As both the impeller diameter and blade tip height are typically provided in the datasheet of the machine, the difficulties of obtaining information of the detailed geometry of the machine can be avoided. [22, p. 2] [19, pp. 133-135]

To make the dimensionless performance maps more robust, all the different regions of the map should be represented by an appropriate function. As the behavior of the curve differs between the surge, normal operation and stonewall sections, each section should be predicted by an own function with parameters fitted to the reduced data. Figure 8 shows a dimensionless polytropic head curve with the surge section described by an exponential function to the left of the vertical black line, the normal operation region described by a power function between the two vertical lines and the stonewall section described by a quadratic function to the right of the blue vertical line. The operating regions are marked in the same manner in Figure 9, which shows a dimensionless compressor power curve, where both the surge and stonewall sections are described by quadratic functions, while the section for normal operation is described by a power function. [23, p. 45]
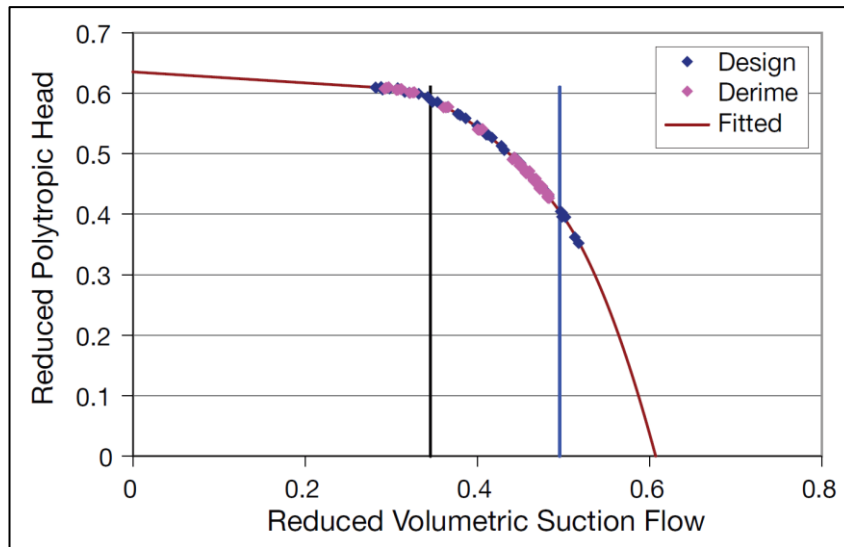
Figure 8. Sections of a dimensionless polytropic head curve depicted by different functions. [23]
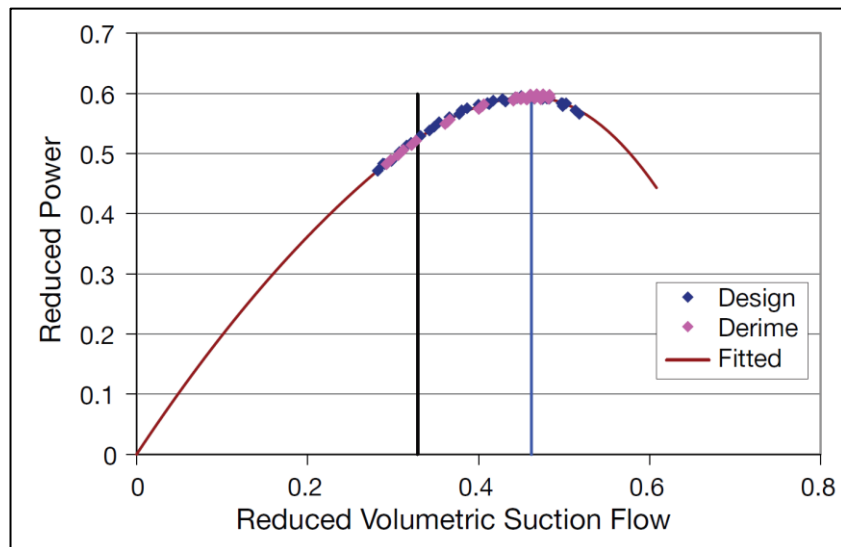

Figure 9. Sections of a dimensionless power curve depicted by different functions. [23]

2.2.1.1 Inlet flow coefficient

The presented inlet flow coefficient method requires the impeller diameter and the performance maps of the manufacturer, as well as the reference conditions for these, for transforming the curves to the dimensionless variant. The governing process conditions are needed for estimation of the new performance curves. [22, p. 2]

The performance of the compressor is influenced by inlet conditions such as temperature, compressibility, ratio of specific heats, molecular weight and impeller blade tip speed. The effects of all these variables are considered by the dimensionless tip speed Mach number, calculated by Equation 37, where U is the blade tip speed, given by Equation 38. Note that the rotation speed should be given as revolutions per second. If two sets of inlet conditions have equivalent Mach numbers, their dimensionless performance curves will also be the same. [22, pp. 2-4]

$$M_u = \frac{U}{\sqrt{\kappa_1 Z_1 T_1 \frac{R}{MW}}} \tag{37}$$

$$U = \pi d \omega \tag{38}$$

Conversion of the performance curves themselves is done by transforming the polytropic head into the dimensionless head coefficient ψ and the volumetric flow into the inlet flow coefficient φ_1. These conversions are done with Equations 39 and 40. [22, p. 4]

$$\psi = \frac{2H_p}{U^2} \tag{39}$$

$$\varphi_1 = \frac{4\dot{V}}{\pi d^2 U} \tag{40}$$

After the conversion, an array of dimensionless operating curves, each corresponding to a certain Mach number, has been obtained. One such array is shown in Figure 10. Using Equation 37, a new Mach number $M_{u,new}$ is calculated from the new inlet conditions. Based on the relation of the new Mach number to the Mach numbers of the previously calculated dimensionless curves, the full dimensionless curve, consisting of the new head coefficient ψ_{new} and the new inlet flow coefficient $\varphi_{1,new}$, is created by a curve approximation method, e.g. linear interpolation or cubic spline interpolation. [22, p. 5]
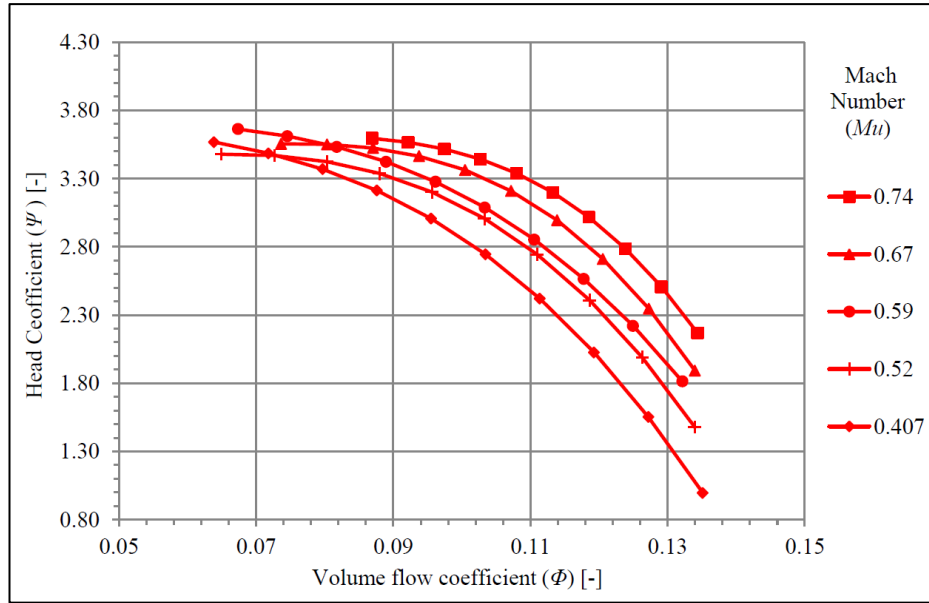
Figure 10. Dimensionless inlet flow coefficient operating curves. [22, p. 5]

Lastly, the actual new operating curve, consisting of $H_{p,new}$ plotted against $\dot{V}_{new}$, is calculated from the new dimensionless curve using Equations 41 and 42. [22, p. 6]

$$H_{p,new} = \psi_{new} \frac{U_{new}^2}{2} \tag{41}$$

$$\dot{V}_{new} = \varphi_{1,new} U_{new} d^2 \frac{\pi}{4} \tag{42}$$

When operating within the Mach numbers given in the design data, using this method the new polytropic head curves can be approximated within an accuracy of 3%. [22, pp. 1,6-7] The method does, however, have some weaknesses. It is strictly valid only if each stage of the compressor is treated separately. In addition, the accuracy of the prediction quickly deteriorates if the new dimensionless curves are extrapolated from those derived from the manufacturer data. [22, pp. 7-8]

2.2.1.2 Exit flow coefficient

If the head coefficient ψ is used in conjunction with the exit flow coefficient φ_3 instead of the inlet flow coefficient φ_1, the performance of each compressor stage can be presented in a single dimensionless curve for all conditions up to a critical Mach number. For Mach numbers above

the critical values, the curves will be reduced and lie to the left of the curve for the lower Mach numbers. During tests performed for two compressors, both the head coefficients and efficiencies could be presented in a single curve while operating below the critical Mach numbers, even as molecular weights of the compressed gas ranged from 29 g/mol to 365 g/mol. These curves are shown in Figure 11. The tests for one machine also showed that, even for the reduced curves, both the maximum head coefficient and the maximum efficiency occurred at a constant value of φ_3. For another machine, however, the maximum efficiency was not only reduced in magnitude, but also shifted to lower values of φ_3 when exceeding the critical Mach number. [24, pp. 93, 96-98] A central finding is that a single gas parameter does not affect the flow similarity. Rather, the combination of the parameters making up the tip speed Mach number is what counts as a flow similarity characteristic. [19, pp. 136-137]
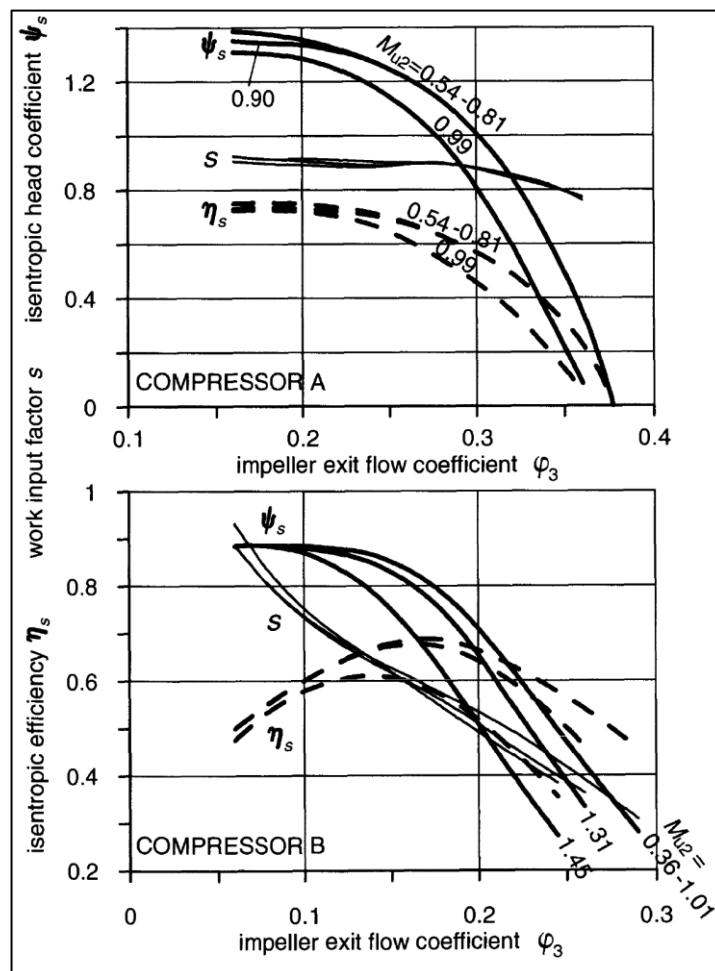
Figure 11. Exit flow coefficient performance curves for the second stage of two compressors. [19, p. 136]

To calculate φ_3 Equation 43 is used, where b_2 is the impeller blade tip height. Alternatively, φ_3 can be calculated from φ_1, as shown in Equation 44, where f is a leakage factor. [19, p. 135]

$$\varphi_3 = \frac{\dot{V}_3}{\pi d b_2 U} \tag{43}$$

$$\varphi_3 = f \varphi_1 \frac{\dot{V}_3/\dot{V}_1}{4(b_2/d)} \tag{44}$$

The impeller diameter is usually known. The blade tip height might also be provided by the manufacturer, but if this is not the case, an approximation for b_2 can be obtained from Equation 45, where η_L is a leakage efficiency and the value of φ_3 is approximated from an empiric relation to φ_1 at the best efficiency point. Said empiric relation is presented in Equations 46 and 47. [25, p. 3] [19, p. 175]

$$\frac{b_2}{d} = \frac{\varphi_1(\dot{V}_3/\dot{V}_1)f}{4\varphi_3\eta_L} \tag{45}$$

$$\varphi_3 = \varphi_1 + 0.215 \; for \; \varphi_1 < 0.038 \tag{46}$$

$$\varphi_3 = 1.8\varphi_1 + 0.187 \; for \; \varphi_1 \geq 0.038 \tag{47}$$

The ratio of the static volumetric flow rate $\dot{V}_3$ to the inlet flow rate is given by Equation 48, from which $\dot{V}_3$ is easily solved. [25, p. 4] A description of the calculation of the temperature relation is given in Chapter 2.2.4.

$$\frac{\dot{V}_3}{\dot{V}_1} = \frac{T_3}{T_1}\frac{p_1}{p_3}\frac{Z_3}{Z_1} \tag{48}$$

Once the dimensionless curve consisting of ψ and φ_3 has been constructed, calculation of the performance curve for the new operating conditions can commence. Equation 41 is used to calculate the new values for the polytropic head. As deduced in Appendix D, the values for the new inlet volume flow can be calculated with Equation 49, where $\dot{V}_3$ is given by Equation 50, deduced in Appendix C.

$$\dot{V}_{1,new} = \dot{V}_3 \frac{T_{1,new}}{T_{3,new}}\frac{p_{3,new}}{p_{1,new}}\frac{Z_{1,new}}{Z_{3,new}} \tag{49}$$

$$\dot{V}_{3,new} = \varphi_3 \pi d b_2 U_{new} \tag{50}$$

As stated in Appendix G, the new temperature ratio is given by Equation 51. The new outlet pressure is given by Equation 52, deduced in Appendix A. As shown in Appendix B, n can be calculated from κ and η_p according to Equation 53. The value of the polytropic efficiency should correspond to the value of φ_3. Equation 32 is used in the calculation of the compressibilities.

$$\frac{T_{1,new}}{T_{3,new}} = \frac{1}{\left(\frac{p_{3,new}}{p_{1,new}}\right)^{m_{new}}} \tag{51}$$

$$p_{3,new} = p_{1,new} \times \sqrt[\left(\frac{n_{new}-1}{n_{new}}\right)]{\frac{H_{p,new}}{\frac{R}{MW_{new}}Z_{avg,new}T_{1,new}\left(\frac{n_{new}}{n_{new}-1}\right)} + 1} \tag{52}$$

$$n = \frac{1}{1 - \frac{\kappa - 1}{\kappa\eta_p}} \tag{53}$$

Once $H_{p,new}$ and $\dot{V}_{1,new}$ are calculated for the range of the dimensionless curve, the new operating curve is ready for use. Unfortunately, even this method is strictly applicable only for a single compression stage. Searching for a general way to describe the operation of the whole compressor in a single curve, which would be a great benefit for accurate dynamic simulation, appears to be a Sisyphean task, as no such thing as an invariant performance curve seems to exist for multistage compressors. [19, p. 134] In Appendix F and Appendix G equations are deduced for direct conversion of a point on the operating curve to a point on a curve for new operating conditions.

2.2.2 Surge

As previously mentioned, operating the compressor at a flow below the surge point causes the operation to become unstable. Surge occurs when the machine attempts to achieve an excessive increase in pressure at an insufficient flow rate. [26, p. 6.4] The instabilities appear as pressure and flow oscillations in the process system. The oscillations may be present in the magnitude of the flow in the forward direction, but the entire direction of the flow may also alternate. System surge can best be explained by the extended operating curve shown in Figure 12. The region to the left of point A is usually not shown, as this is unstable operating region.

In short, operations to the right of point A are stable, as momentarily shifting the operating point from point 1 to point 2 or 3 will cause the dynamics of the rest of the system to restore the initial operating point. If, however, the machine is forced to operate on the part of the curve with a positive slope, i.e. to the left of point A, a small disturbance from a point 1′ to 2′ will cause the system to move the point even further away from point 1′, causing the machine to enter the surge cycle ADBEA. The instabilities generally occur when the gradient of the system resistance curve is larger than the compressor curve gradient. [19, pp. 140-142] Increases in the gas discharge temperature can also be observed, as gas at discharge temperature enters the impeller during back flow and is thus re-heated for each oscillation cycle the machine undergoes. [26, p. 7]
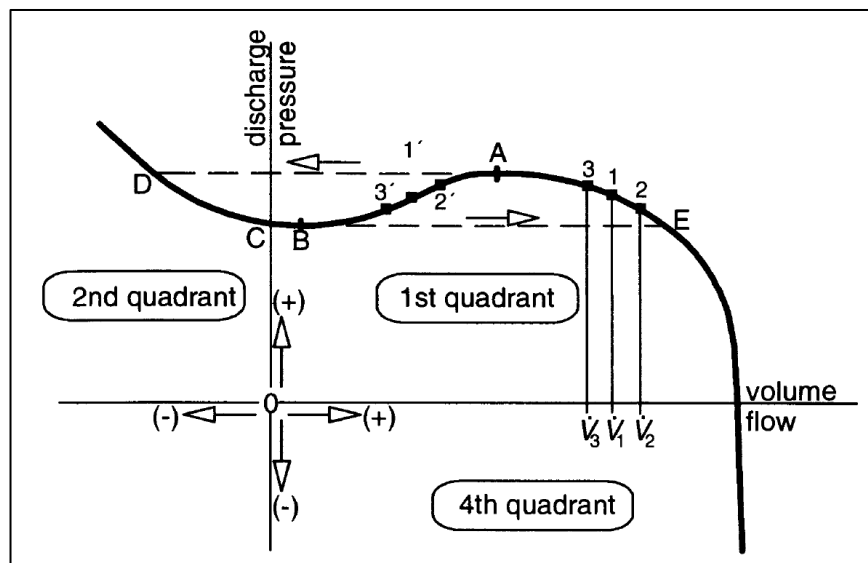
Figure 12. Extended performance curve detailing surge oscillations. [19, p. 141]

Surge is a very rapid phenomenon. The flow reverses in 20 to 40 milliseconds and the machine can go from normal operation to surge in a few tenths of a second. [26, p. 6.9] Due to the swiftness and destructive nature of the phenomenon, a surge margin is usually defined, above which the machine is to be operated to ensure surge does not occur. The margin can be defined to the automation system controlling the compressor. The system will then, for example, initiate minimum flow circulation to prevent surge. The impeller pulsation can be expected to occur at a constant value for the exit flow coefficient. [24, pp. 95, 97] The surge point usually corresponds to the minimum inlet flow coefficient plotted. If the surge point is based on the exit flow coefficient, it may be possible to scale the coefficient's value at surge from its value at the design point. A surge margin as a percentage can then be defined according to Equation 54. [25, p. 5]

$$Surge\ margin = \frac{\varphi_{3,surge} - \varphi_3}{\varphi_3} \times 100 \tag{54}$$

24

2.2.3 Stonewall

As previously stated, the second limit of the operating curve is the stonewall, or choke point, where flow velocity at the impeller blade inlet reaches the sonic velocity in the medium. [19, p. 148] The speed of sound in the medium can be calculated with Equation 55. [27, p. 8] The Mach number relates the flow velocity to the sonic speed. When the relative Mach number reaches a value of 1, the maximum possible flow is achieved. The number is calculated by Equation 56, where $u_{in,rel}$ is the inlet flow velocity relative to the impeller blade. [18, p. 92]

$$a = \sqrt{\kappa T Z \frac{R}{MW}} \tag{55}$$

$$M_{rel} = \frac{u_{in,rel}}{\sqrt{\kappa g T_1 \frac{R}{MW}}} \tag{56}$$

While stonewall as a phenomenon may not be as destructive as surge, operation at stonewall conditions is still not desirable, as the efficiency of the compressor is severely reduced. In Figure 13, the choke point of the compressor is defined as the point where the head of the last stage reaches zero. If the compressor is pushed a little more, the operating point of the last stage will be driven into the fourth quadrant of the coordinate system. If this happens, the stage starts consuming the compressor head rather than generating it. Operation in the fourth quadrant does not mean the stage acts as a power generating turbine. On the contrary, it requires power input in order to operate at this unusual mode. [19, pp. 148-149]
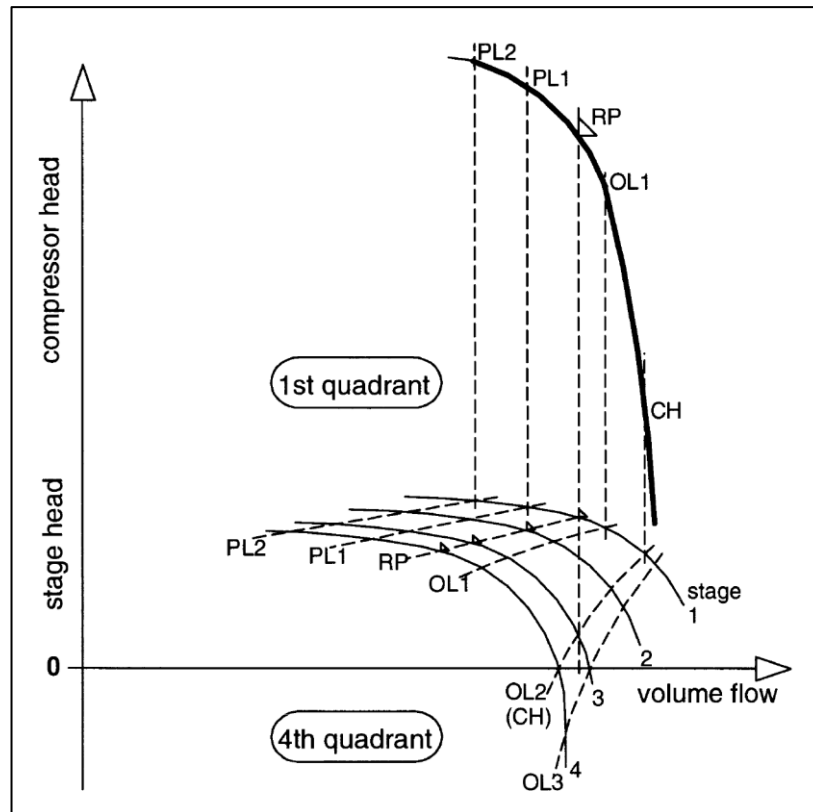
Figure 13. Performance curve of a four-stage compressor, along with individual stage performance curves. PL stands for part load, RP for rated point, OL for overload and CH for choke. [19, p. 149]

2.2.4 Outlet temperature

As a large portion of the compression energy appears as heat in the gas, the temperature increase in a compressor is often substantial. This can be a limiting factor for the operation of the machine, unless cooling of the compressor or interstage heat exchangers are deployed. For an ideal gas undergoing isentropic compression, the ratio of the outlet and inlet temperatures can be calculated with Equation 57. [9, pp. 412, 417] Sometimes the polytropic efficiency is added to the exponent, as shown in Equation 58. [19, p. 56]

$$\frac{T_3}{T_1} = \left(\frac{p_3}{p_1}\right)^{(\kappa-1)/\kappa} \tag{57}$$

$$\frac{T_3}{T_1} = \left(\frac{p_3}{p_1}\right)^{(\kappa-1)/\kappa\eta_p} \tag{58}$$

The irreversibility of a real compression process results in a higher outlet temperature than that given by Equation 57. [9, p. 418] For a better estimation, the polytropic temperature exponent *m* is used, as shown in Equation 59. The exponent is calculated with Equation 60, where *X* is a generalized compressibility function, supplementing the compressibility factor *Z*. It is, in turn, given by Equation 61. If the operating conditions are not close to critical conditions, the equation for *m* reduces to Equation 62. [13, pp. 84-85]

$$T_3 = T_1 \left(\frac{p_3}{p_1}\right)^m \tag{59}$$

$$m = \frac{ZR}{C_p}\left(\frac{1}{\eta_p} + X\right) \tag{60}$$

$$X = \frac{T}{V}\left(\frac{\partial V}{\partial T}\right)_p - 1 \tag{61}$$

$$m = \frac{\kappa - 1}{\kappa \eta_p} \tag{62}$$

When used for calculating the dimensionless φ_3 performance maps, *m* is sometimes defined by Equations 63 to 66. Here η_{p3} is the impeller total-to-static polytropic efficiency, κ_{T3} is the isentropic temperature coefficient, *Rxn* is the stage reaction and *s* is the impeller work input factor. As the stage reaction contains φ_3, this approach is iterative. [25, p. 4]

$$m = \frac{Z_1 R}{C_{p,1}}\left(\frac{1}{\eta_{p3}} - 1\right) + \frac{\kappa_{T3} - 1}{\kappa_{T3}} \tag{63}$$

$$\frac{\kappa_{T3} - 1}{\kappa_{T3}} = \frac{\ln\left(\frac{T_{3,is}}{T_1}\right)}{\ln\left(\frac{p_3}{p_1}\right)} \tag{64}$$

$$\eta_{p3} = \frac{\sqrt{\eta_p} + Rxn - 1}{Rxn} \tag{65}$$

$$Rxn = 1 - \frac{\varphi_3 - s^2}{2s} \tag{66}$$

2.2.5 Power consumption

The compression work done on a gas during isothermal conditions is given by Equation 67. The polytropic process is more complex and the expression for the compression work takes the form of Equation 68. An estimation for the required work by the machine can be obtained by calculating the ideal work and correcting the value with a suitable efficiency. For centrifugal machines the polytropic work is normally used. [13, pp. 81-82]

$$W = p_1 V_1 \ln \frac{p_3}{p_1} = \frac{RT_1}{MW} \ln \frac{p_3}{p_1} \tag{67}$$

$$W = p_1 V_1 \frac{n}{n-1} \left(\left(\frac{p_3}{p_1} \right)^{(n-1)/n} - 1 \right) = Z \frac{RT_1}{MW} \frac{n}{n-1} \left(\left(\frac{p_3}{p_1} \right)^{(n-1)/n} - 1 \right) \tag{68}$$

If no estimation of the ideal work is available, the polytropic work can be calculated with the help of another generalized compressibility function *Y,* in addition to the previously presented function *X*. Expressions for these functions are given in Equation 61 and 69. The functions can be used to calculate the polytropic exponent *n* and polytropic temperature exponent *m*, which in turn are used to determine the polytropic work and the outlet temperature. Calculation of *m* was presented in Equation 60, 62 and 63. The polytropic exponent is given by Equation 70. Unless operating at extreme conditions, the expression reduces to Equation 71. [13, pp. 84-85]

$$Y = - \frac{p}{V} \left(\frac{\partial V}{\partial p} \right)_T \tag{69}$$

$$n = \frac{1}{Y - m(1 + X)} \tag{70}$$

$$n = \frac{1}{1 - m} \tag{71}$$

Once the compression work *W* has been calculated, the electric power required to drive the compressor can be estimated by Equation 72, where η_e is the efficiency of the electric motor. [13, p. 93] If the compressor head is known, the power can be calculated from Equation 73. [14, pp. 10.37-52]

$$P = \frac{W \dot{m}}{\eta_e} \tag{72}$$

$$P = \dot{m} H \tag{73}$$

For an adiabatic (no heat losses) and isentropic (no entropy generation) compressor, the required power is given by Equation 74, where h is the specific enthalpy of the gas. Considering the adiabatic and mechanical the efficiency and combining these into one general efficiency for the compressor, the total power required by the compressor will be given by Equation 75. [15, pp. 142-144] [19, p. 17] If $\dot{m}$ and H_p are given in imperial units, the shaft horsepower of the compressor can be calculated with Equation 76. The factor 1.02 accounts for 2% gear losses. [28, p. 116]

$$P_{ad} = \dot{m}(h_3 - h_1) \tag{74}$$

$$P_{tot} = \frac{\dot{m}(h_3 - h_1)}{\eta} \tag{75}$$

$$P_{shaft} = \frac{\dot{m}H_p}{33000\eta_p} \times 1.02 \tag{76}$$

As the dimensionless work input factor s appears as a single curve when plotted against the exit flow coefficient, regardless of the governing Mach number, it could prove quite useful for predicting the required work input. The work input factor describes the sum of the dimensionless thermodynamic, disk friction and shroud leakage work and can be calculated from the enthalpy difference between the inlet and the outlet according to Equation 77. It can also be bound to φ_3 at best efficiency point, as shown in Equation 78, where β_2 is the impeller blade exit angle, I is the number of impeller blades and Δs is an experimentally determined correction. Equation 79 gives an approximate size for the correction. [19, pp. 37, 138, 177-178]

$$s = \frac{\Delta h}{U^2} \tag{77}$$

$$s = 1 - \frac{\sqrt{\sin \beta_2}}{I^{0.7}} - \frac{\varphi_3}{\tan \beta_2} - \Delta s \tag{78}$$

$$\Delta s = -0.017 \pm 0.005 \tag{79}$$

2.3 Turbines

Turbines, also known as expanders, can in many regards be viewed as the opposite machinery of the pump and compressor. Where pumps and compressors add energy to a fluid stream, the turbine can be used to extract energy from a stream. Turbines can be built for use in both liquid and gas streams. The turbines usually consist of a casing, vaned impellers mounted on a shaft and guide vanes between the impeller stages. The turbine converts the kinetic and potential energy of the stream to shaft work. The shaft can be connected directly to a machine requiring power, such as a pump or compressor, or to an electric generator. [29, p. 37] [14, p. 722] It is usually worthwhile to consider driving large pumps and compressors with steam turbines on site and using the exhaust steam as a heat source for the process, as this improves the energy integration of the process and reduces total electricity cost. [13, pp. 900-901] Steam turbines are utilized in power generation systems responsible for over 60% of the global electricity generation. [30, p. 3]

Like the compressors, the turbines are characterized by an operating curve. The turbine can experience choke when the inlet flow reaches the velocity of sound. [31, p. 251] The curve is not limited by surge, as the flow through the unit is from high pressure to low pressure conditions. However, in low-pressure applications condensation may occur, leading to aerodynamic, mechanical and irreversible thermodynamic losses. [30, p. 19] This phenomenon must be considered for turbines operating at conditions where condensation may occur.

The expansion process can be modeled as polytropic. [13, p. 108] The outlet temperature at expansion can be calculated with Equation 59. For expansion m is calculated with Equation 80 if using the generalized compressibility functions X and Y. The expression for m reduces to Equation 81 when not operating at critical conditions. For expansion, the polytropic efficiency is defined as the ratio of the actual work obtained to the polytropic work. [13, p. 85]

$$m = \frac{ZR}{C_p}\left(\eta_p + X\right) \tag{80}$$

$$m = \frac{(\kappa - 1)\eta_p}{\kappa} \tag{81}$$

The power generated by the turbine is given by Equation 82, where W is the work done by the expanding fluid and η is the turbine efficiency. [13, p. 207] The expansion work can be calculated with Equation 68. [13, p. 82] Effects of changes in outlet pressure Δp_3 on steam turbine power can be approximated with Equation 83, if entropy generation is neglected. Here

v_3 is the specific volume of the steam at the outlet. Estimation of the effects of changes in the inlet conditions is more complex. Usually enthalpy-entropy diagrams are used for this. [29, p. 43]

$$P = W\dot{m}\eta \tag{82}$$

$$\Delta P = -\eta\dot{m}v_3\Delta p_3 \tag{83}$$

3 Current pump, compressor and turbine models

In this chapter the current state of the pump and compressor models in ProsDS is described. Modeling of pumps, compressors and turbines is also present in several other simulation software. User manuals and various other sources have been briefly reviewed for Aspen Plus, Aspen HYSYS, Honeywell UniSim Design, Dynsim and Apros. There would appear to be several similarities, but also differences, between the implementations in the various simulators. For example, most use some form of a performance curve to model the equipment. However, some seem to have the machine operate along only one curve, while other programs utilize several performance curves or curve scaling to better describe the dynamic behavior of the machine.

3.1 ProsDS

In ProsDS the machine itself is only a part of the various calculations. For flow calculations, for example, the surrounding equipment supply the rest of the information, such as pressure loss in pipes. [32] Flow resistance in pipes is usually considered in the CV value of the valves during modeling, but various other options for modeling the pressure loss are also available. However, all these options rely on conversion to Aspen AV to determine the flow resistance. [33]

The pumps are modeled using theoretical maximum head at zero flow and pressure loss due to flow. The head H_{max} can be given either as pressure difference or height of fluid column. The pressure loss is modeled using the equation for the valve flow coefficient CV, which relates pressure loss to flow as a quadratic function. [32] The CV value is calculated with Equation 84, where SG is the specific gravity of the pumped fluid. The flow is given as US gallons per minute and the pressure loss is given in psi. [34, pp. 18-19] The operating curve for the pump is thus given by Equation 85. A curve of this sort is usually accurate enough for pumps around their normal operating points. Effects of changes in the rotating speed are taken into account in the head of the pump quadratically. [32]

$$CV = \dot{V}\sqrt{\frac{SG}{\Delta p}} \qquad (84)$$

$$H = H_{max} - SG\frac{\dot{V}^2}{CV^2} \qquad (85)$$

The compressors are modeled as pumps with some extra features. Generally, a better fit to the machine data should be made for the compressors. For compressor curve fitting a correction function is used, which takes the actual load of the compressor into account. A correction factor for the effect of guide vanes is also available. These correction factors are modeled individually for each compressor by the person doing the modeling work. The quality of the fit is usually dependent on the required accuracy of the modeling of a unit. These requirements are said to seldom be very high, as this equipment is only considered to be a small part of the whole process model. Any other calculations regarding the operating curves are usually carried out as external calculations modeled outside of the machine. Cavitation, surge and stonewall are very rarely modeled. No automatic curve correction for changes in e.g. molecular weight or inlet temperature exists in the simulator, these are defined by the modeler as external calculations. For compressors in general, the curve type should be steeper at higher loads than what the *CV* based quadratic curve is. A fourth-degree ellipsoid should give a considerably better fit. [32]

The power requirement of the machines is also modeled in a simple manner. It is based on the flow and pressure difference over the machine, with a corresponding efficiency. The outlet temperature is also modeled in a simple way, based on either an empirically approximated constant or on the inlet and outlet pressures. [32]

3.2 Other simulator software

Aspen Plus is a modeling tool mainly used in the oil and gas industries. It uses the underlying physical relationships, such as material balances, energy balances, thermodynamic equilibrium and rate equations, to predict the behavior and output of the simulated process. The software can simulate both steady state and dynamic state. The operation of the pumps in Aspen Plus can be specified in three ways; with pressure by defining the discharge pressure, the pressure increase or the pressure ratio, by required pumping power or by defining the

performance curve of the pump. Using this input, the software calculates the fluid and brake horsepower, required electricity and available *NPSH*. If information about the specific speed and suction specific speed are supplied to the model, the required *NPSH* will also be calculated. [35]

Aspen HYSYS is an engineering simulation tool with capabilities for both steady state and dynamic state simulations. The tool is used in industries related to gas processing, cryogenics, refining and chemicals. Simulation of pumps, compressors and expanders is possible in HYSYS. The simulator utilizes equations of state along with component and stream properties to perform the calculations. The pump increases the pressure of an inlet liquid stream. The simulator either calculates the outlet pressure, outlet temperature or pump efficiency, depending on what information is provided. If the inlet stream is fully specified and the outlet pressure is given to the pump, the simulator has enough information to perform the calculations. [36, pp. 32-40]

The HYSYS compressor block works in the same manner as the pump; it increases the pressure of a stream and solves the stream outlet pressure, outlet temperature or compressor efficiency, depending on the provided information. Both centrifugal and reciprocating compressors can be modeled. A polytropic or adiabatic efficiency can be defined for the machine. Furthermore, the compressor can be specified to operate along a single performance curve, or it can be given multiple curves for varying molecular weights or inlet guide vane settings. [36, pp. 41-51] The expander block decreases the pressure of a gas stream. Like the pump and compressor, the expander calculates either a property of the outlet stream or an expansion efficiency. The expander can use several methods to perform the calculations, but in general the solution is a function of flow, pressure difference, work and efficiency. The efficiency can be either adiabatic or polytropic. [36, pp. 52-58]

Honeywell's UniSim Design is a process simulation tool featuring simulation of event driven operation and modular operations. [37, p. 1.2] The software is used in gas processing, cryogenic, refining and chemical industries. It can be used for both steady state and dynamic simulation. [37, pp. 2.2-3] Positive displacement pumps, centrifugal pumps, reciprocating compressors, centrifugal compressors and expanders can be modeled with UniSim. The sizing and configuration variables, as well as the specification types, e.g. head or speed, for these machines are static. The specification values, however, are dynamic. [37, pp. 7.43-44] Enough information of the inlet, outlet and energy streams connected to the pump must be specified, so that the pump duty and the pressure difference across the pump can be calculated. Otherwise the simulation will not run. The pressure difference and pump duty can also be specified by the modeler. Much of the same holds true for both the compressors and expanders, but

information is only needed for the calculation of the duty. A value for the duty can also be given by the modeler. It is calculated if both the inlet and outlet pressures are specified. [37, pp. 8.11-12]

Dynsim is a dynamic process simulator by Invensys Process Systems. It is used for simulation of gas processing, liquified natural gas, refining, petrochemical and chemical process plants. [38] Modeling of pumps, centrifugal compressors, reciprocating compressors and expanders is available in Dynsim. The modeler can specify either the entire operating curve for the pump and centrifugal compressor or use scaling parameters to adjust a default curve for the head, flow and efficiency. A reference speed should also be provided. Both machines use the fan laws to calculate the flow and head at other speeds. The software seems to fit a third-degree polynomial to the curve to obtain a continuous modified performance curve. The pump can be modeled at three different operating regions, namely normal operation with positive head, hydraulic turbine operation where the suction pressure is higher than the discharge pressure and reverse flow operation, where the developed head is not enough to reach the discharge pressure. The pump calculates the shaft work and fluid enthalpy rise. The speed of the pump is given as an input, either by the modeler or by some other part of the process model. The model uses the pressure difference between the inlet and outlet to calculate the available head, which is then used to interpolate the volume flow from the specified operating curve. The efficiency is interpolated in the same manner from the efficiency curve. [39]

Effects of inlet guide vanes can be considered in the performance curve of the Dynsim compressor. The model can indicate when the compressor goes into surge if the modeler has specified a surge flow point at the design condition. The software uses this point to define a surge line through the coordinate system origin. Dynsim can simulate compressor operation in four regions. The regions are normal operation with positive head, surge at low flows or high head, reverse flow when the developed head is insufficient to compress the fluid against the discharge pressure and stonewall operation when the suction pressure is higher than the discharge pressure. The calculated compressor head is based on isentropic calculations. In the same manner as for the pump, the volumetric flow and compressor efficiency are interpolated once the head is calculated. [39]

The Dynsim expander block can be used to model a steam turbine or a gas expander. The speed of the turbine is decided by other parts of the process model. The expander is modeled using isentropic efficiency and a flow conductance equation. The modeler gives the efficiency and a conductance parameter as inputs. A custom efficiency curve can also be defined. The power generated by the expander is based on the isentropic efficiency. [39]

Apros is a dynamic simulation software developed by Fortum and VTT. It is mainly used for the modeling of power plants, energy systems and industrial processes. [40] For the compressors in Apros the required input data is the dimensions of the flow area and design point values for inlet pressure and temperature, pressure ratio, mass flow, compressor speed and efficiency. The user can also specify a number of custom performance curves for the compressor. Otherwise a predefined curve is used. The performance curves plot the pressure ratio against the mass flow. The curves have their own corresponding dimensionless speeds. The modeler defines the curve by giving the mass flow and pressure ratio at the vertex point and at a point to the right of the vertex. The software then approximates the curve as a second-degree polynomial. The compressor block calculates the pressure and enthalpy increase of the stream with Equations 86 and 87. Π is the pressure ratio, which is read from the operating curve. It is a function of the mass flow, rotation speed and inlet temperature and pressure. The outlet enthalpy is a function of the specific heat capacity and outlet temperature, of which the latter in turn is a function of inlet temperature, pressure ratio, polytropic efficiency and molecular weight. [41]

$$\Delta p = p_1 (\Pi - 1) \tag{86}$$

$$\Delta H = m(h_3 - h_1) \tag{87}$$

The behavior of the Apros turbine is defined by specific volume, efficiency and inlet and outlet mass flows and pressures at the design point. The rotation speed is also given as an input if the turbine is not connected to a separate shaft module. The modeler can specify an efficiency curve for the turbine. It can be given either as a function of volumetric or mass flow. If the flow goes outside of the given points for the curve, the first or last value for the efficiency is used. A curve for the efficiency as a function of the rotation speed can be defined in a similar manner. The isentropic efficiency used for the expansion process is obtained by interpolating a value from both curves using the flow and rotation speed and multiplying these two values. The modeler can also give the Stodola coefficient K as input, which generally is used in defining the dependence of outlet pressure to flow and is of importance in turbine calculations when operating outside of design conditions. The coefficient is usually calculated at nominal load with Equation 88, where v_1 is the specific volume at inlet. The coefficient is assumed to be constant for the turbine. In the flow and pressure calculations the turbine is treated as a flow resistance causing pressure drop in the stream. The pressure loss is solved from the equation for the form loss coefficient F, Equation 89. The simulator calculates the outlet enthalpy as a function of the inlet enthalpy and the turbine efficiency and design point values. Different models are used for steam and gas turbines. Gas turbines use Equation 87 with the enthalpies reversed. For a steam turbine Equation 90 is used, where η_{ent} is the entropic expansion

efficiency. Equation 91 is used if the stream contains droplets. The index *l* denotes liquid, x_{steam} is the steam fraction and notation *h(p)* is for the saturation enthalpy at pressure *p*. The mechanical power produced by the turbine is also calculated by the simulator. [41]

$$K = \dot{m}\sqrt{\frac{p_1 v_1}{p_1^2 - p_3^2}} \tag{88}$$

$$F = \frac{2}{K^2 \rho \left(1 - \frac{p_3}{p_1}\right)} \tag{89}$$

$$\Delta H_S = \dot{m}\left(h_{1,steam} - \left(h_{1,steam} - h_{ref}\right)\left(\frac{p_3}{p_1}\right)^{\eta_{ent}/4.27} - h_{ref}\right) \tag{90}$$

$$\Delta H = x_{steam}\Delta H_{steam} + (1 - x_{steam})\left(h_{1,l}(p_1) - h_{3,l}(p_3)\right)\dot{m} \tag{91}$$

4 Developed compressor model

For a dynamic simulator used in operator training, correct and accurate behavior is vital. The simulator should, at the bare minimum, be able to run in real-time, which limits the acceptable computational complexity for any single piece of machinery or equipment in the process model. As the process model needs to be able to handle a plethora of operating conditions and upset scenarios, the compressor model should also be flexible and robust. Changes in the inlet temperature, gas composition, pressure and flowrate, rotation speed of the compressor, as well as changes in the outlet pressure, should affect the compressor operation in an appropriate manner.

The compressor operation is characterized by the operating point, outlet temperature and consumed power, of which the operating point is most important. As such, the focus during this work was mainly on calculating the operating point and describing its behavior during off-design operation. Power and outlet temperature calculations were also implemented, but in a relatively simple manner. As computationally heavy methods such as CFD modeling of the entire machine is not an option for dynamic simulation, the best way to accurately calculate the operation of the machine would seem to be to use the performance curves and determine how they change with varying operating conditions.

Implementing a single performance curve and using empiric correction coefficients for each variable to scale it would likely not work in a sufficient manner, as determining such coefficients would be difficult. Additionally, due to the complexity of the machine, such simple coefficients would probably not be able to sufficiently predict the entire performance curve for the wide range of operating conditions the machine may be exposed to.

Building a model that takes several performance curves as input and interpolates between these might also be difficult, as each curve is strictly valid only at the specific operating conditions they were created for. The availability of performance curves may also be limited, so creating a performance map for each variable would likely not be possible. To properly determine how to interpolate between the curves, some parameter describing the lumped impact of all the operating condition variables would have to be found. One such parameter would be the Mach number, but sadly the curves do not seem to be arranged in any strict order corresponding to their respective Mach numbers in a performance map in the natural dimensions. Extrapolation to off-design operation would also likely be inaccurate.

Dimensionless curves unaffected by the rotational speed and inlet condition, on the other hand, can be accurately implemented to the process simulator. [23, p. 42] The inlet flow coefficient method appears as accurate, flexible and relatively simple to implement, but the need for interpolation and, in particular, extrapolation of the dimensionless curves is an unwanted feature. The inlet flow coefficient performance curves are still affected by the inlet conditions and the rotating speed, as they vary with the Mach number. The exit flow coefficient method appears as similar but slightly more complex than the inlet flow coefficient method, with the distinction that it produces a single dimensionless performance curve for a wide range of Mach numbers, which is thus largely unaffected by changes in the operating conditions. Using the exit flow coefficient to predict compressor operation appears as a viable method for dynamic simulation and, as such, it was selected for further study.

Equipment data for three multi-stage compressors, referred to as A, B and C, was provided for testing and validation of the model. Process data from a real process plant was also available for compressor C. The equations and the prediction capability of the method was first tested in Excel for these compressors. Once a working model in Excel was ready, implementation and testing began in ProsDS. Note, that the values of polytropic head, volumetric flow and compressor power presented in certain graphs in this chapter, as well as in some of the appendices, have been scaled to mask the actual values.

4.1 Model

At first, the polytropic head versus volumetric inlet flow operating curves of compressors A and B were converted to the dimensionless form in Excel using Equations 39 and 43. The expression for the volume flow ratio was simplified from Equation 48 to Equation 92, as the compressibilities generally did not seem to vary that much and calculation of the outlet compressibility seemed a bit challenging at this stage. The temperature ratio was calculated based on Equation 59. Equations 52 and 53 were used to calculate the outlet pressure. In Equation 52 the inlet compressibility was used instead of the average. Both compressors were modeled as a single stage operation, meaning only one dimensionless curve was used for the entire machine. To align the dimensionless curves, the exponent *m* was used as a tuning parameter with a constant value common for every curve of the same compressor.

$$\frac{\dot{V}_3}{\dot{V}_1} = \frac{T_3}{T_1}\frac{p_1}{p_3}$$ (92)
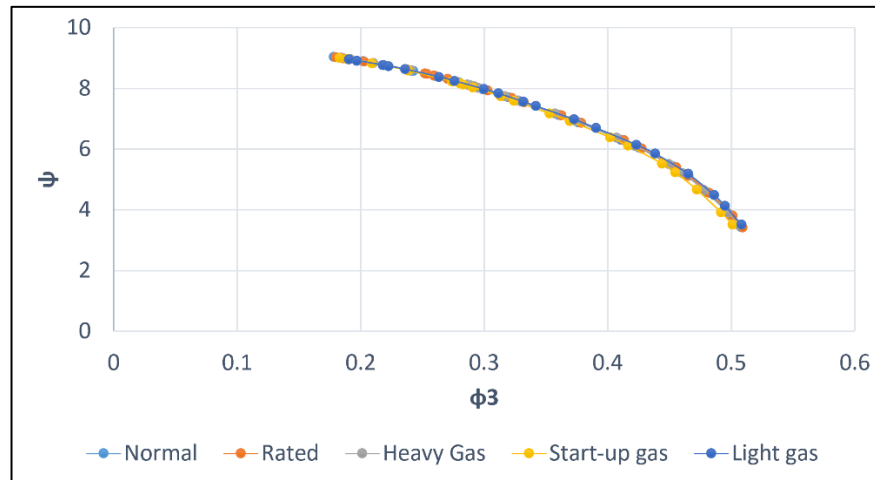
Figure 14. Dimensionless exit flow coefficient performance curve of compressor A.
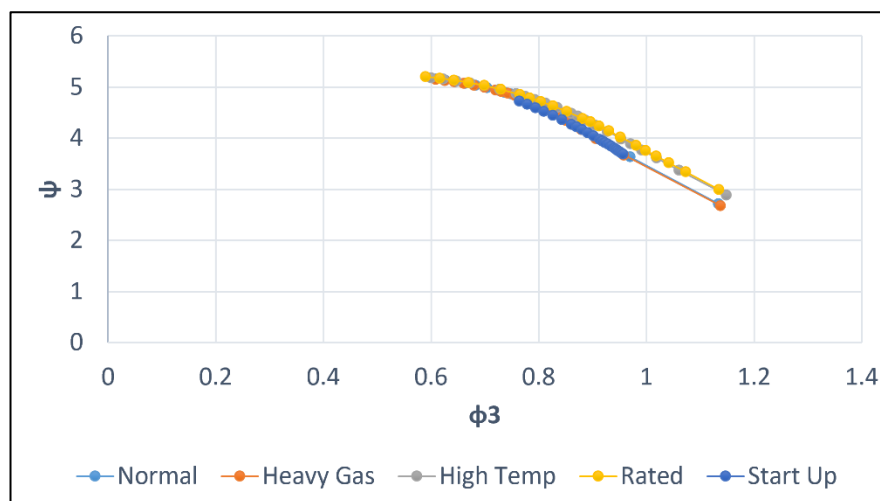
Figure 15. Dimensionless exit flow coefficient performance curves of compressor B.

As Figure 14 and Figure 15 show, this method of alignment worked rather well for both compressors. As can be seen in Appendix H, however, most of the operating curves for compressors A and B were quite close to each other to begin with. Nevertheless, the figures in Appendix J show that the predicted operating curves for compressor A are a near perfect match, while it can be seen in Appendix K that, while most of the predictions are a good match, there are some issues with the prediction of a few of the stonewall regions and with the start-up case for compressor B. The dimensionless performance curve and dimensionless polytropic efficiency curve of the rated case were used to calculate the predicted curves in Excel.

Regrettably, the same approach did not work as well for compressor C. This might be due to aerodynamic mismatch between the stages, which means "a progressive drift-off for each

subsequent stage from its intrinsic best efficiency point once the first stage is operated at an off-design point". [19, p. 43] As can be seen from the performance maps in Appendix H the performance curves of compressor C are also more scattered compared to those of the other two compressors. It was possible to slightly improve the alignment by calculating an individual value for *m* for each point on the converted curve. Based on Equation 62 and the relationship between *n* and *κ* described in Appendix B, calculation of *m* was performed with Equation 93. To compensate for the reduced assumption made in Equation 62, the polytropic efficiency was also added. In addition, a tuning parameter m_{corr} was added. This parameter is common for all the curves and can be used by the modeler to align the curves.

$$m = \frac{n-1}{n\eta_p} m_{corr} \tag{93}$$

The aligned dimensionless curves for compressor C are displayed in Figure 16. The performance curves provided by the manufacturer were digitalized by hand, which is the cause for some of the irregularities that can be seen in the curves. It is clear that the alignment of the dimensionless curves for compressor C did not work as well as for compressors A and B, but as can be seen in the figures of Appendix L, most of the predicted performance curves are not that far off. Figure 17 shows that the dimensionless polytropic efficiency curves for compressor C are quite close to each other which, as can be seen in Figure 18, was also the case for the efficiency curves of compressor B. This is likely a contributing factor for some of the good predictions, even though the dimensionless operating curves for the cases do not overlap.
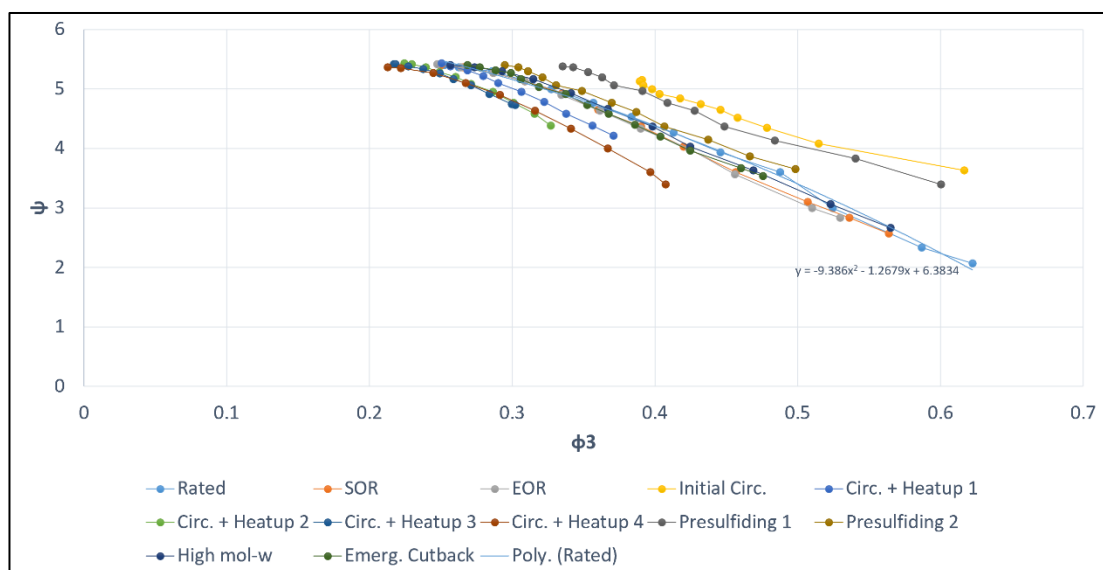
Figure 16. Dimensionless exit flow coefficient performance curves of compressor C, with a correction factor of 3.2 used for *m*.
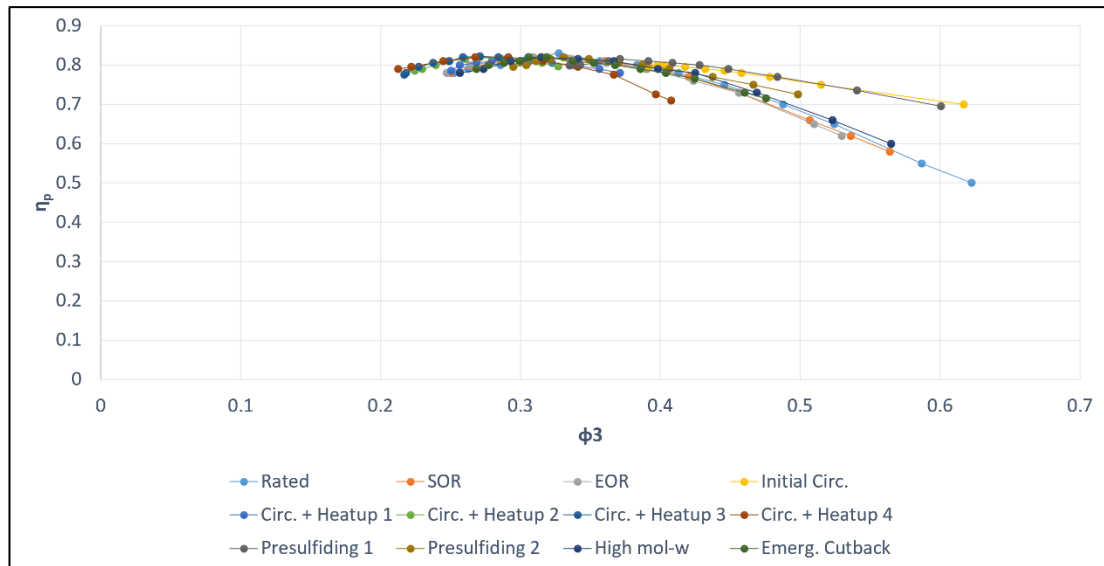
Figure 17. Dimensionless polytropic efficiency curves of compressor C.
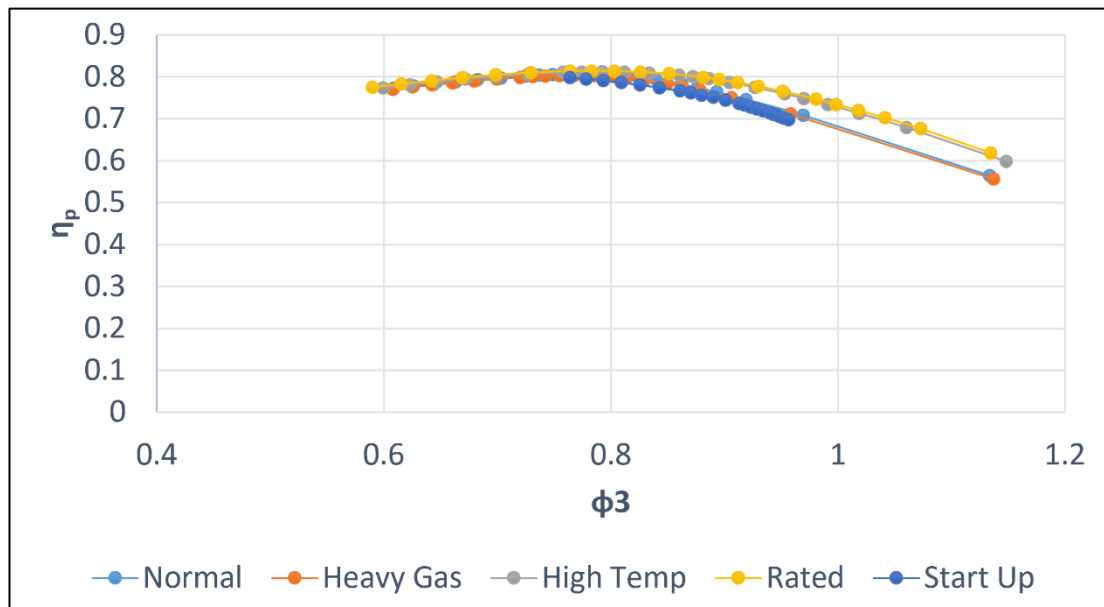
Figure 18. Dimensionless polytropic efficiency curves of compressor B.

Initially attempts were made to fit a function to the operating curves in natural scale. This function would then have been transformed to the dimensionless plane, but as can be seen from Figure 19, the second-degree polynomial is a poor match to the data and polynomials of higher order show a wobbling behavior, even within the data range they were fitted to. In addition, polynomials of higher degree may behave unexpectedly outside of the plotted range. Both features are unwanted in a dynamic process simulator. [23, p. 45] Thus, the operating curves were first transformed to the dimensionless form and the polynomials then fitted to this data range. The second-degree polynomials proved a good approximation for the normal operating region, as can be seen in Figure 20. Strict limits were imposed for the surge and

stonewall regions, although a better approach would be to use functions similar to those presented in Figure 8 and Figure 9. The modeler gives the values for the exit flow coefficient for the inception of surge respective stonewall. The first and last point of the dimensionless performance curve for the rated case were used as the limits in the test model. Surge is modeled by dropping the flow through the compressor to zero. At stonewall the volume flow is capped at the value corresponding to the exit flow coefficient stonewall limit.

As can be seen in Appendix L, some of the predicted curves started turning backwards as they approached stonewall operation. To avoid any problems caused by this, the ProsDS model checks if the volume flow in each point is greater than in the previous point on the curve. If this is not the case, the volume flow of the point is assigned the value of the previous point on the curve. This marks the end of the ordinary operating curve and the start of the stonewall region.
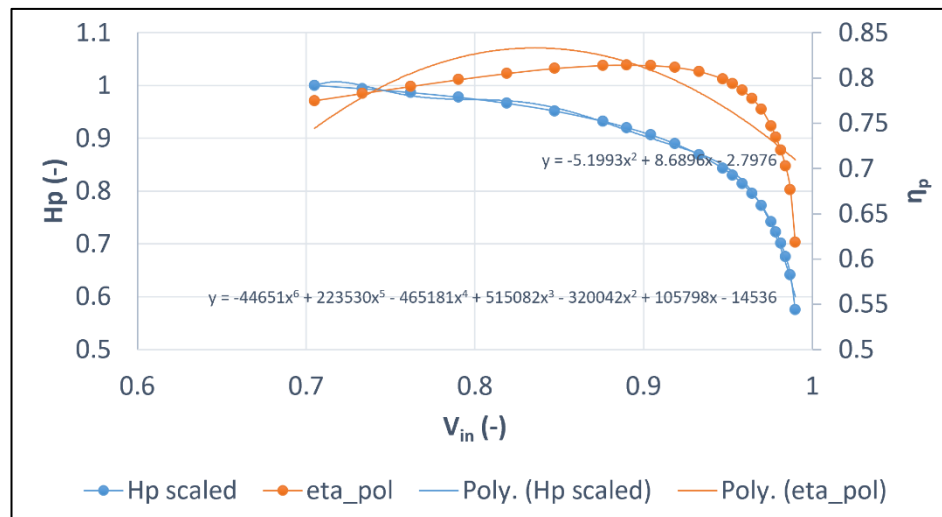
Figure 19. Attempts to fit a second-degree polynomial to the polytropic efficiency curve and a sixth-degree polynomial to the operating curve of compressor B in natural dimensions.
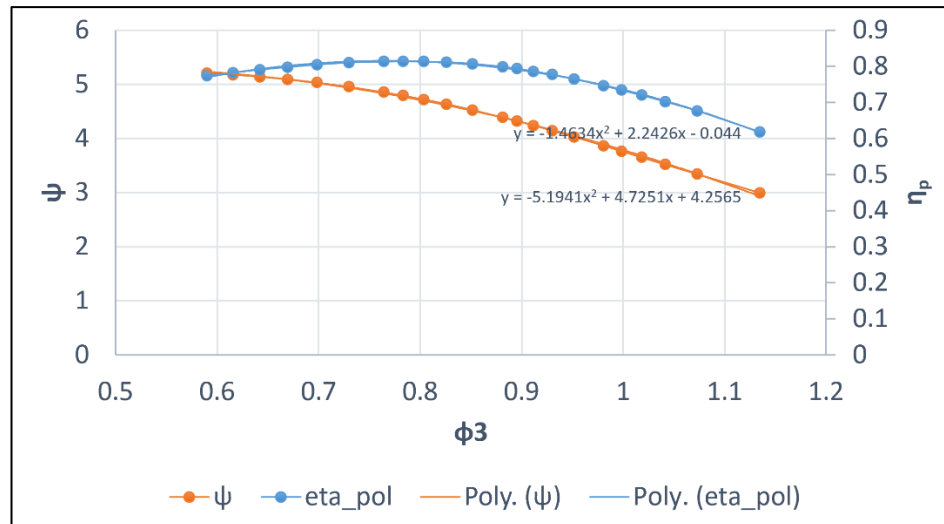
Figure 20. Attempts to fit a second-degree polynomial to the polytropic efficiency and head coefficient curves for compressor B in the dimensionless plane.

Once polynomials have been fitted to the dimensionless performance curve and the dimensionless polytropic efficiency curve, the coefficients of the polynomials are given as input to the constructed compressor model in ProsDS as shown in Figure 21. Coefficients *A*, *B* and *C* are for the second-degree polynomial of the performance curve, while coefficients *AE*, *BE* and *CE* are for the efficiency curve. *Phi3min* and *Phi3max* are the surge respective stonewall limits. The model divides the range between the limits to a specified amount of points. Together these points create a list, which constitutes the values of a variable over the specified operating range. By pairing the values in two lists together, the model is able to specify curves. The dimensionless performance curve, for example, is created by pairing the lists of φ_3 and ψ together. The model also needs the impeller diameter, impeller blade tip height, m_{corr} and the voltage of the machine as inputs by the modeler. If the speed of the machine would change *Nnew* would be used in the prediction of the new operating curves.
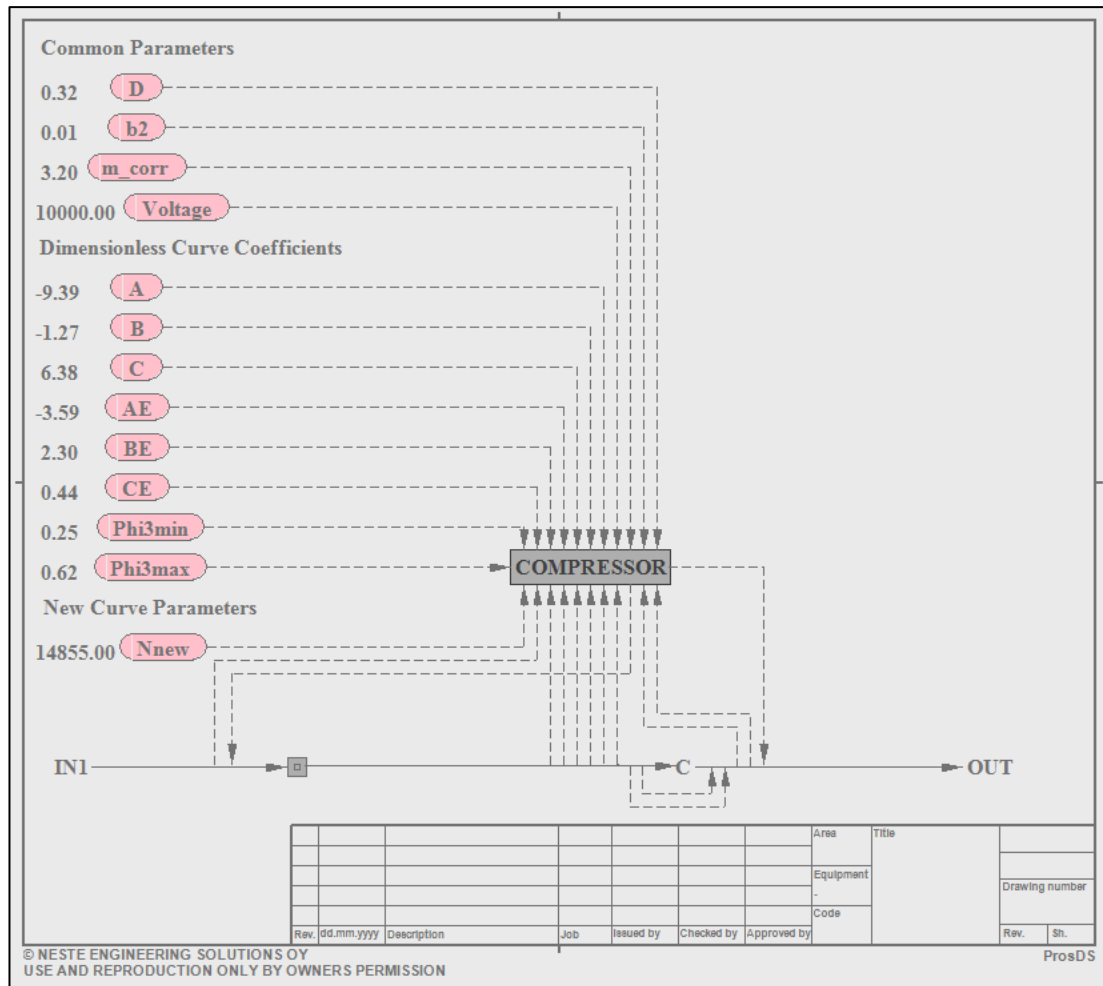
Figure 21. The compressor model constructed in ProsDS.

The simulator model contains three source-sinks; IN1, C and OUT, with streams in between. These are the inlet and outlet streams, with source-sink C representing the compressor. The inlet stream is connected to a stirred tank block, which can be used to change the equation of state used for the stream. The non-linear function block COMPRESSOR contains the equations and performs the necessary calculations of the simulated compressor. The function block reads the temperature, pressure, molar weight, specific heat capacity, molar flow, molar volume and enthalpy from the inlet flow. The pressure and enthalpy are read from the outlet stream. The compressor block then calculates and writes the volume flow to the inlet stream and the temperature to the outlet stream. The mass flow and weight fractions are written from the inlet stream, over source-sink C, to the outlet stream. The stirred tank in the inlet was found to alter the temperature occasionally, so the inlet temperature was read before tank. The inlet volume flow was also written before the tank. The other parameters had to be read after the tank in order to get the desired effect when changing the used equation of state in the tank.

Once the model has all the needed inputs from the modeler and the streams, it starts by calculating values for the new polytropic head using Equation 41. Next, κ is calculated with Equation 94, as deduced in Appendix E. The polytropic index is calculated with Equation 53 and *m* is calculated with Equation 93. After the inlet compressibility has been calculated with Equation 32, the outlet pressure list for the new performance curve can be evaluated. The outlet pressure is calculated with Equation 52.

$$\kappa = \frac{C_p}{C_p - R} \tag{94}$$

To calculate the values in the inlet volume flow list, the model largely follows the procedure described in Chapter 2.2.1.2. The model first calculates the ratio of the inlet and outlet temperature using Equation 51. Values for $\dot{V}_{3,new}$ are obtained with Equation 50. Next, the new values for the inlet volume flow are calculated using Equation 95, which is based on Equation 49 but, as in Equation 92, the compressibilities have been left out.

$$\dot{V}_{1,new} = \dot{V}_{3,new} \frac{T_{1,new}}{T_{3,new}} \frac{p_{3,new}}{p_{1,new}} \tag{95}$$

Once the new values in the lists for the outlet pressure and inlet volume flow have been successfully evaluated, the new operating curve can be described by pairing together the corresponding values from the lists. Now the actual operating point of the compressor can be found. Of the conditions at the outlet, the outlet pressure can be regarded as known. [15, p. 142] The required outlet pressure is defined by the rest of the process system. This pressure then dictates the volume flow the compressor can transport. Thus, using the actual value of the pressure at the compressor outlet, the corresponding value for the inlet volume flow is interpolated from the new operating curve.

Again based on the relationship between *n* and κ described in Appendix B and Equation 58, the outlet temperature at the operating point was calculated with Equation 96. The polytropic index at the operating point is calculated by interpolating from the previously calculated lists for the index and the inlet volume flow. An issue with the iteration was noticed if the compressor operated in the stonewall region. As the value of the volume flow had been limited, several values for the polytropic index corresponded to a single value of the volume flow. In this situation, the model used the last value in the list of the polytropic index, which caused a jump in the outlet temperature. To avoid this, a small constant value was subtracted from the volume flow used in the interpolation. The outlet temperature is said to be a tricky variable to calculate and the polytropic index may be a too ideal assumption here. [32] Based on some tests in Excel for compressor B, adding *Z* to the exponent seemed to improve the accuracy of

the temperature calculation at design point operation. The effect of this correction depends on the used equation of state; if the ideal equation of state is used Z will not affect the calculated temperature.

$$T_3 = T_1 \left(\frac{p_3}{p_1}\right)^{(n-1)/nZ} \tag{96}$$

During the testing it was discovered that the values calculated for κ and Z by the simulator differ from those reported by the manufacturer. The C_p value used for obtaining κ is calculated from the enthalpies in the simulator. The enthalpy calculations are based on the used equation of state and are typically accurate at low pressures. The accuracy deteriorates as the pressures increase. No-one but the manufacturers themselves can say how they have obtained their parameters. The parameters may even be completely empirical or based on previous experience. [32] These discrepancies in the values affect both the calculated outlet temperature and the predicted operating curve.

The power consumption was calculated with Equation 97. It closely resembles Equation 74, but the molar flow $\dot{\xi}$ was used in stead of the mass flow, as the enthalpy values in the simulator were per mole. To calculate the electric current consumption of the machine the power was divided by the machine voltage. Accurately calculating the power consumption may be challenging, as the outlet enthalpy is affected by the outlet temperature, which, as previously discussed, suffers from certain issues. Additionally, various losses are associated with the power demand. These should also be considered. [32]

$$P = \dot{\xi}(h_3 - h_1) \tag{97}$$

4.2 Tests

To evaluate the stability, accuracy and dynamic behavior of the constructed model, a series of test were performed in the simulator. The results were compared to both manufacturer data and process data.

4.2.1 Static tests for operating curve and power consumption

To determine the impact of the previously mentioned differences in the values of κ and Z used by the manufacturer and the values calculated by the simulator two tests were carried out for compressor B. Step changes were made to the outlet pressure and the volume flow calculated by the model was recorded. In one test κ and Z were given constant values, matching those reported by the manufacturer, while in the other test the simulator calculated the values. The resulting predictions for the operating curve can be seen in Figure 22.

The figure shows that, in this case, the values differing from those used by the manufacturer result in a slightly reduced curve. If the values of κ and Z match the values used by the manufacturer the prediction is almost perfect. The modeling of surge and stonewall had not yet been implemented in the model at the time the test was carried out, which is why the predicted curves can be seen bending slightly backward on the right-hand side. The reduced curve also forms a wall of points on the left-hand side, as the range of the volume flow the model could use was still limited at this time. If the surge modeling had been implemented at this stage, these points would have corresponded to zero flow.
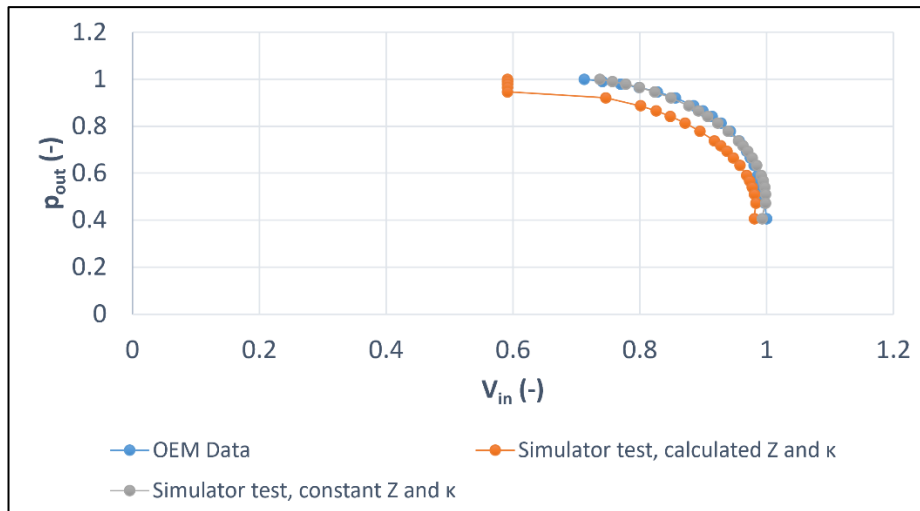
Figure 22. Comparison of scaled original equipment manufacturer curve and simulator test curves used to approximate the effects of the differences in the values of κ and Z.

Similar tests were also carried out to test the accuracy of the implemented power calculation. The outlet pressure was changed in steps, while the calculated volume flow and corresponding power consumption were recorded. The impact of κ and Z was tested in the same manner as previously. Additionally, tests were carried out to determine the effects of the used equation of state on the power calculation. The ideal and the Soave-Redlich-Kwong equations of state were used in the test.
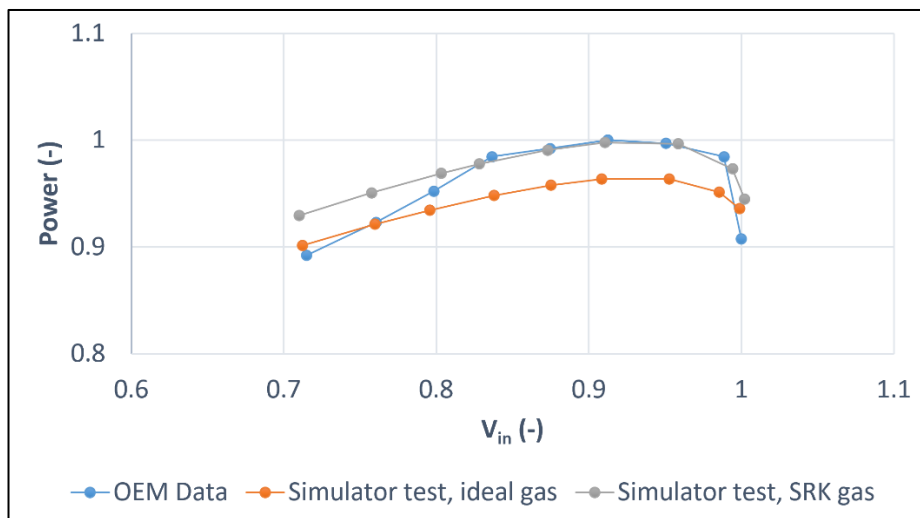
Figure 23. Comparison of scaled manufacturer power curve and predicted curves. Values for κ and Z were given as constants.
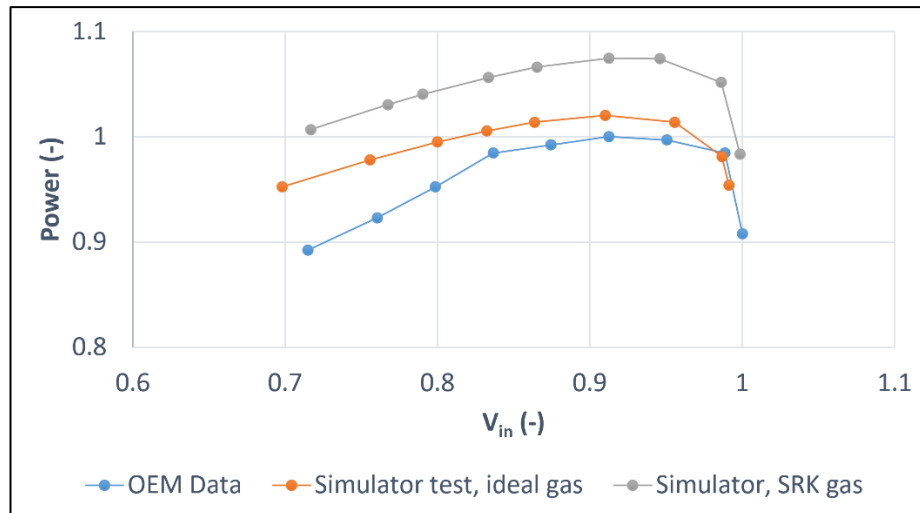
Figure 24. Comparison of scaled manufacturer power curve and predicted curves. Values for κ and Z were calculated by the simulator.

As Figure 23 and Figure 24 show, the predicted power consumption is increased when using the values calculated by the simulator. Use of the SRK equation of state also increases the power consumption, as can be expected. It yields a very good result for most of the curve when the values of κ and Z match the values used by the manufacturer. The accuracy deteriorates somewhat at lower volume flows. For the case where κ and Z are calculated by the simulator, the ideal equation of state gives a better result than the SRK method.

4.2.2 Dynamic tests

The stability and correct dynamic behavior of the model was verified by performing a series of dynamic test for the constructed compressor model in the simulator. During the tests, the temperature, pressure and molecular weight of the inlet stream as well as the pressure of the outlet stream were adjusted up and down by a ramp function in the simulator. The results are presented in the figures below. Clarifications to the legends of the figures are given in Table 1. The model performed well when the variables were ramped within reasonable ranges. Some issues could be observed when the values were ramped down to extremely low, abnormal levels.

Table 1. Explanation of dynamic test graph legends.

Figure legend entries	Explanation
COMPRESSOR POWER	Calculated power consumption
ST1-1 VOLUME FLOW IN	Inlet volume flow
ST1-1 PRESSURE IN	Inlet pressure
C-1 PRESSURE OUT	Outlet pressure
Delta DP	Pressure difference over compressor
Delta PRATIO	Pressure ratio
ST1-1 TEMPERATURE IN	Inlet temperature
C-1 TEMPERATURE OUT	Outlet temperature
Delta DT	Temperature difference over compressor
COMPRESSOR K	Calculated κ
COMPRESSOR POLEXP-FOR-TOUT	Calculated n used in outlet temperature calculation
COMPRESSOR Z	Calculated Z
ST1-1 MW	Flow molecular weight
COMPRESSOR N-EXPMIN	Minimum value of the calculated list for n

Figure 25 and Figure 26 show the ramp down and ramp up of the outlet pressure. As can be seen, the model makes a smooth transition from surge all the way to stonewall. Since the power calculation in the model was based on the flow through the compressor, the power consumption is zero when the model is in surge, which was modeled as zero flow through the compressor. When approaching stonewall the power consumption decreases, as the outlet pressure approaches the inlet pressure. As the pressure ratio decreases the calculated outlet temperature also decreases. The opposite behavior can be observed during the ramp up of the outlet pressure. Figure 27 shows the behavior of the model during unnatural operating conditions. As the outlet pressure is ramped down close to complete vacuum, the power curve can be seen to make a spike towards the end. Such errors were typical when ramping the process variables extremely low. The power consumption also drops to negative as the compressor is forced further into stonewall operation, which, as described in section 2.2.3 is not realistic behavior.
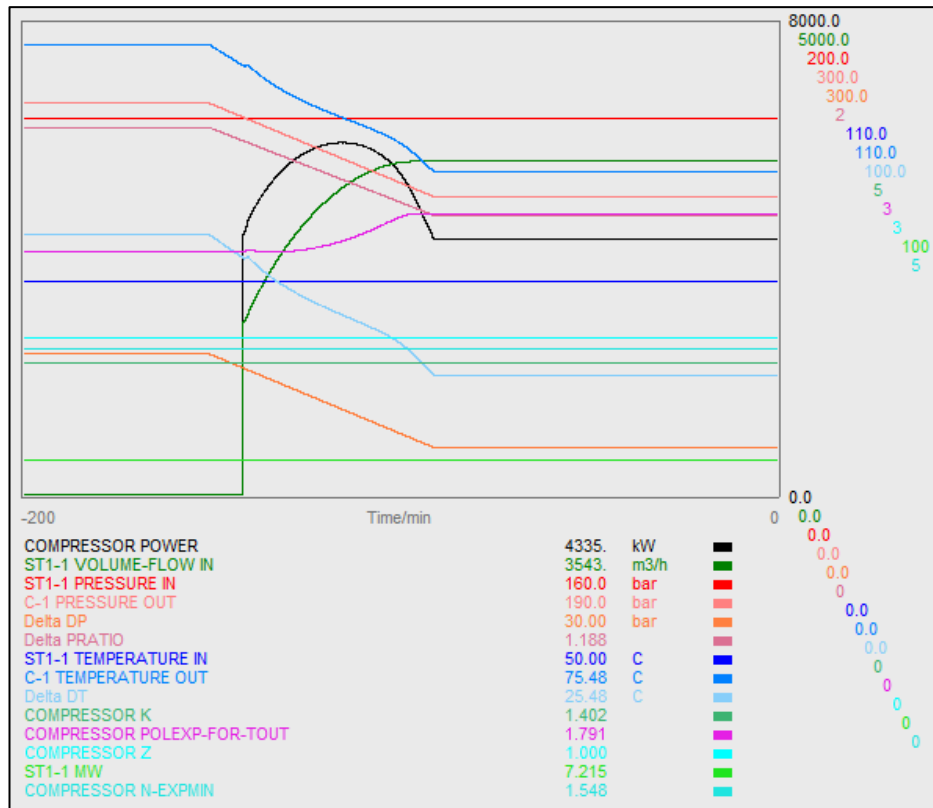
Figure 25. Ramp down of outlet pressure.
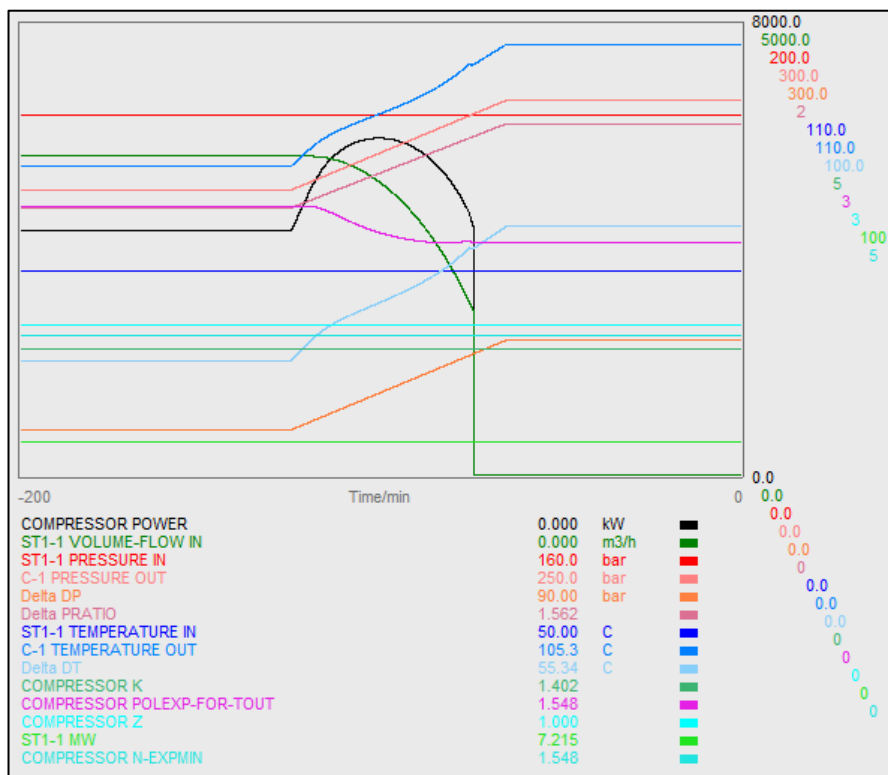
Figure 26. Ramp up of outlet pressure.
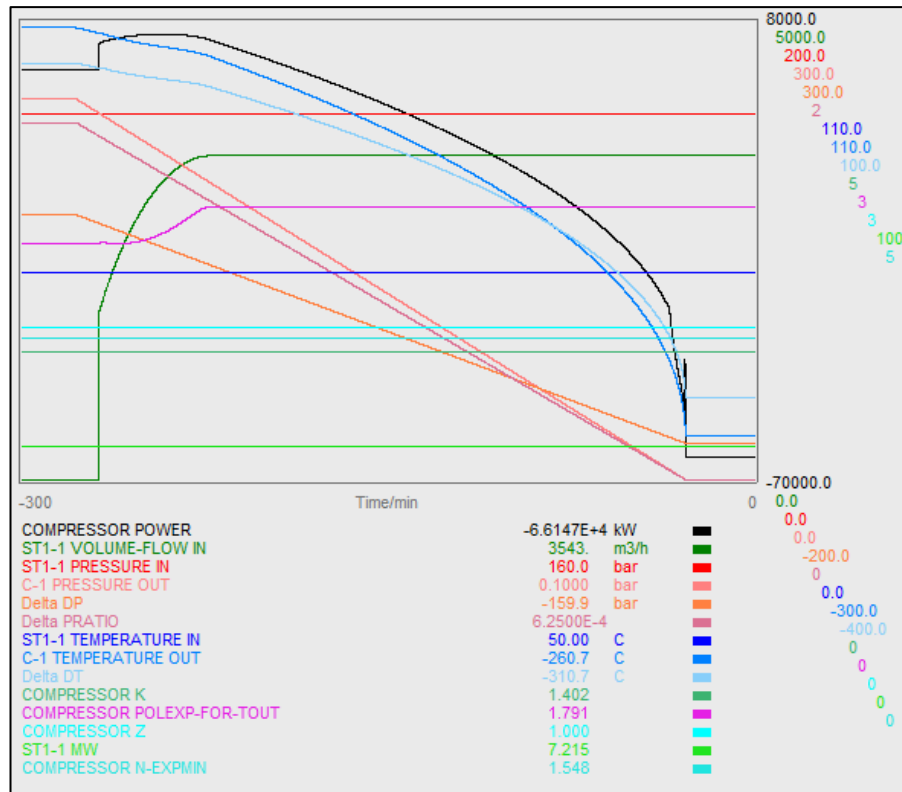
Figure 27. Ramp down of outlet pressure to abnormal levels.

Next, the operating conditions of the inlet stream were ramped. First in order was the inlet pressure. As can be seen in Figure 28 and Figure 29 both the ramp up and ramp down went smoothly at realistic ranges for the pressure. At the start of the ramp down the machine is in stonewall. As the inlet pressure decreases the pressure difference and pressure ratio are increased. From this follows that the outlet temperature increases, which leads to an increase in the compressor power consumption. The volume flow smoothly decreases from its maximum value until it drops to zero as the compressor goes into surge. The power consumption decreases along with the volume flow. As the figures are as good as mirror images of each other the same processes occur in the ramp down of the inlet pressure, but in a reversed order.
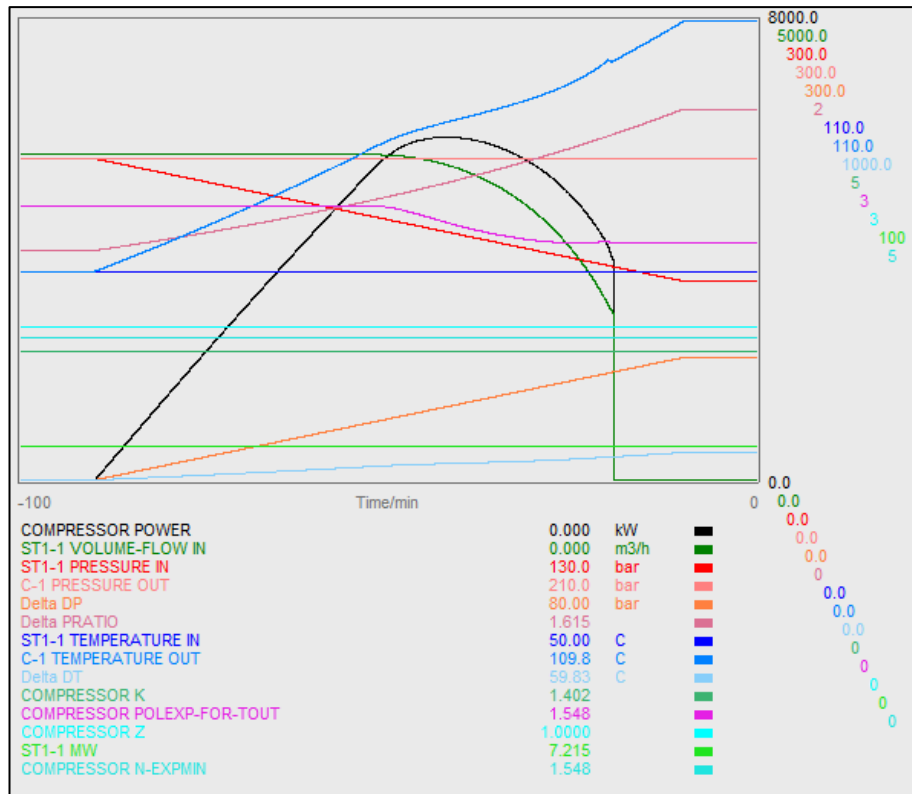
Figure 28. Ramp down of inlet pressure.
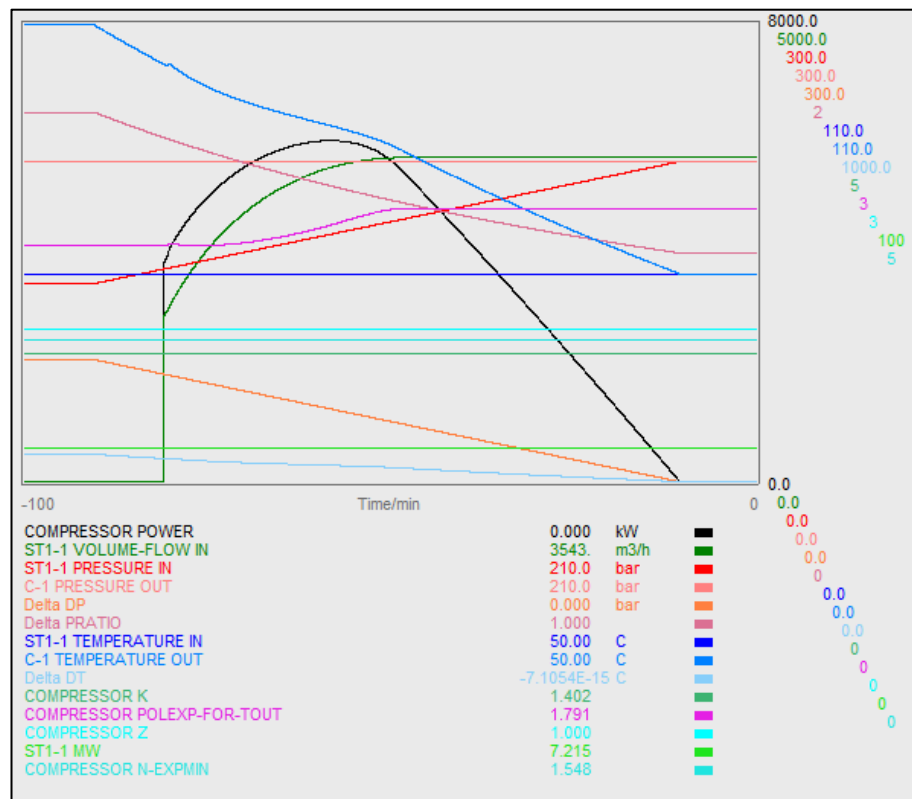
Figure 29. Ramp up of inlet pressure.

While the pressure ramp tests encompassed the entire operating range of the compressor from surge to stonewall, the temperature variations had a much milder impact on the operating point of the machine. The results of the temperature ramp test are displayed in Figure 30 and Figure 31. A decrease in the inlet temperature leads to a decrease in both the outlet temperature and the temperature difference. From this follows that the transported volume flow also decreases, which in turn reduces the power consumption. The model again behaves in a similar manner when the process is reversed.
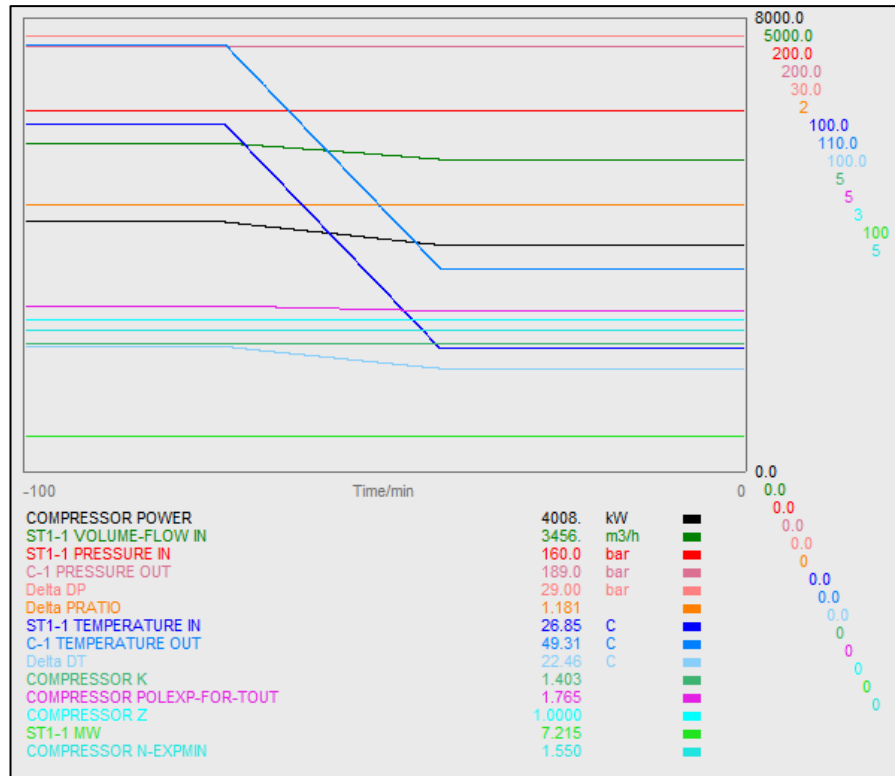
Figure 30. Ramp down of inlet temperature.
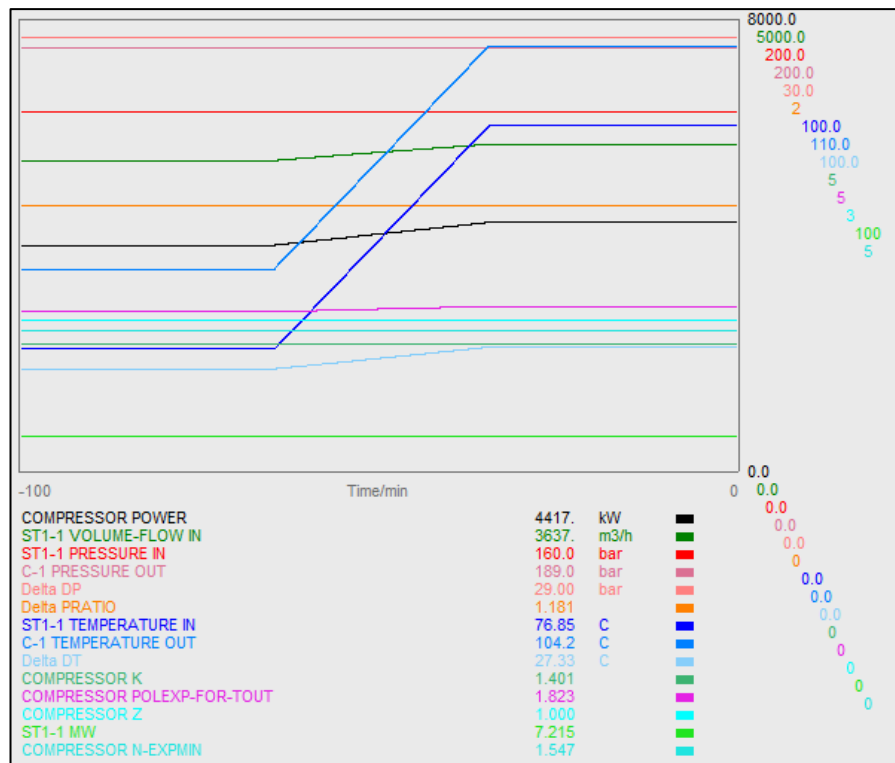
Figure 31. Ramp up of inlet temperature.

The ramping of the molecular weight was last in the series of dynamic tests. The ramping was achieved by creating three streams that merged into the compressor inlet stream. Each stream had a different composition, resulting in a low, medium and high molecular weight. A function was created to adjust the position of a valve in each stream, resulting in the ramping of the molecular weight in the compressor inlet stream.

Figure 32 and Figure 33 show the behavior of the model during the ramp down and ramp up of the molecular weight. The behavior is again similar but reversed for the cases. As the molecular weight decreases, the volume flow increases. This causes the power consumption and the polytropic exponent to rise. The rise in the polytropic exponent results in an increase in the outlet temperature, which also contributes to the rise in the calculated power consumption.
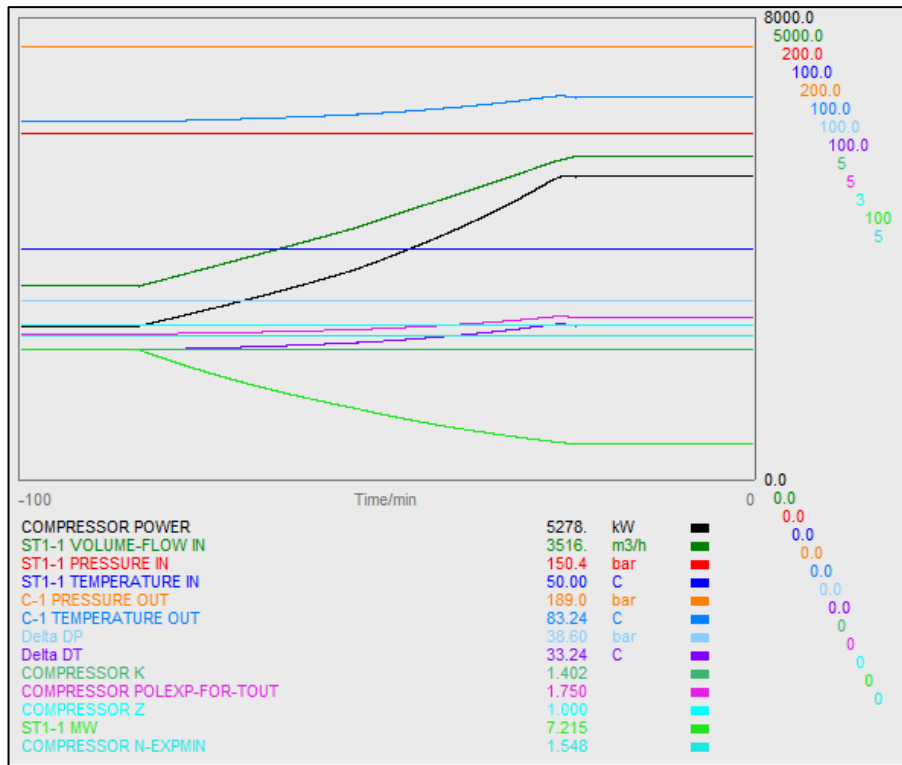
Figure 32. Ramp down of molecular weight.
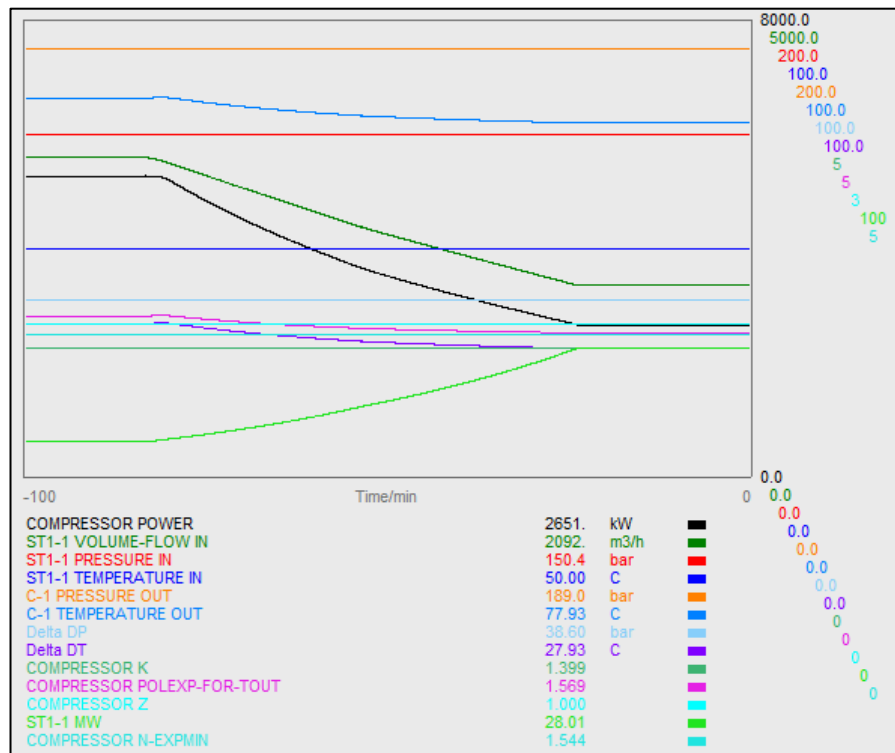
Figure 33. Ramp up of molecular weight.

4.2.3 Process data tests

Once the validity of the concept had been proved in Excel and the stability of the constructed model ascertained with the dynamic tests, the testing could progress to assess the actual accuracy of the model by performing the process data tests. Process data of three different operating cases was obtained for compressor C. The basic model presented in Figure 21 was expanded to the model shown in Figure 34 to accommodate for the process data testing. The data of the stream inlet temperature, composition and pressure as well as outlet pressure, all displayed in Appendix M, was fed to the test model, which then predicted the inlet volume flow, outlet temperature and compressor power consumption.

To import and export the data to ProsDS from excel and vice versa, several connectors were added to the test model: TI for temperature data, PI for pressure, FI for flow, IIA for current and AI for composition. The mass flow of the inlet stream was read form the simulator, as the available process data was the mass flow measurement. The data of the component analyzers was given as volume fractions. [33] It had to be converted into weight fractions for the simulator, so a function block was added to the model for this purpose.

Parallel to the new compressor model the existing compressor block in the simulator was connected to inlet and outlet streams. Process data was written to these streams in a similar manner as for the new model and the results were gathered for a comparison of the current implementation and the developed model.
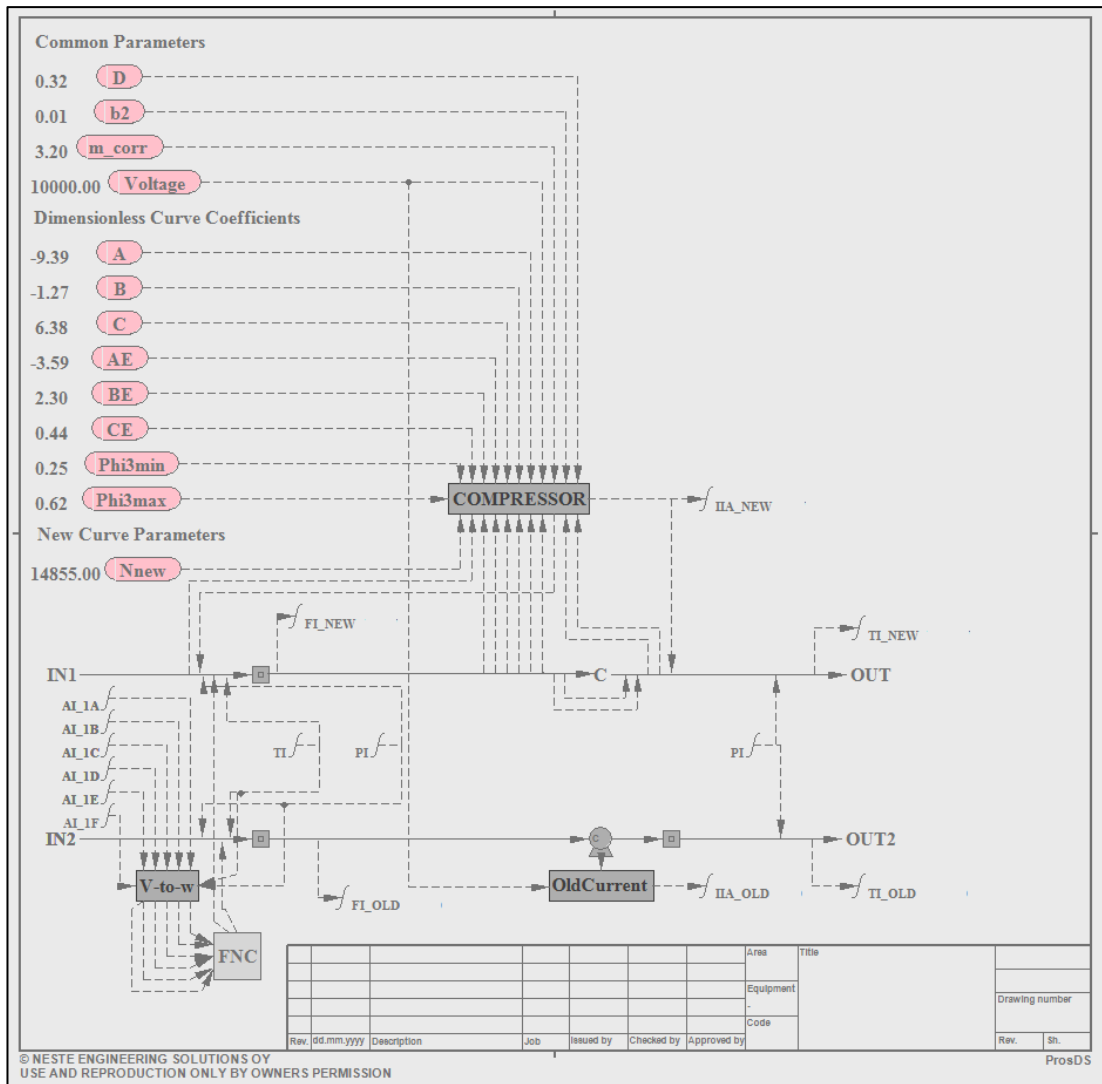
Figure 34. The compressor model constructed in ProsDS expanded for process data testing.

The first process data case tested was the shutdown case. This case was tested twice to determine whether to use the SRK or the ideal equation of state for the remaining cases. The SRK method was tested first. The results are displayed in Figure 35 to Figure 39. The first figure shows that the mass flow curve predicted by the new model has a similar shape as the process data curve. At conditions close to normal operation the predicted flow lies slightly below the measured flow. It is possible that inaccuracies in the measurements, which can be up to several tens of percent in some cases, may lie behind some of the differences. Various calculations and corrections may also be done to the measured data in the automation system. [33] However, the most likely reason for the difference in this case is the effect of the values of κ and Z calculated by the model. As shown by Figure 22 the difference in the calculated values and the manufacturer values may have a reducing effect on the predicted operating curve, leading to lower mass flows at the given pressures.

As the process conditions diverge from normal operation the offset between the curves can be seen to increase. The reason behind this would seem to be increasing inaccuracies in the predicted operating curves. As the figures in Appendix L show, predictions for some of the curves will lie to the left of the manufacturer performance curves when moving from the rated operating conditions towards conditions resembling the initial circulation case. The range of some curves will also be shorter as they are cut off when they start turning backwards.

At times, the predicted mass flow can be seen to jump back and forth between zero flow and the continuous operation trend. The reason behind this behavior is the way surge was taken into consideration in the model. At the mentioned points, the model is balancing on the verge of surge. As described in section 4.1 the limit for the inception of surge was strictly set to the value read from the operating curves provided by the manufacturer. As these values may contain some inaccuracies and reading values from graphs always causes some errors, a better approach would be to give the surge limit with a margin for error to the model, instead of giving the exact value read from the operating curve.

The flow prediction of the old model is far off from the process data. It starts off close to the process data but quickly starts behaving in a completely different manner. Instead of decreasing, the flow rapidly increases. It then remains on a higher level for most of the time before it quickly starts to decrease to a level close to the initial operation. The predicted flow remains at this level for a while, before sharply dropping as the machine is turned off. The flow does not go all the way to zero but remains at a small value above the process data for the rest of the test.
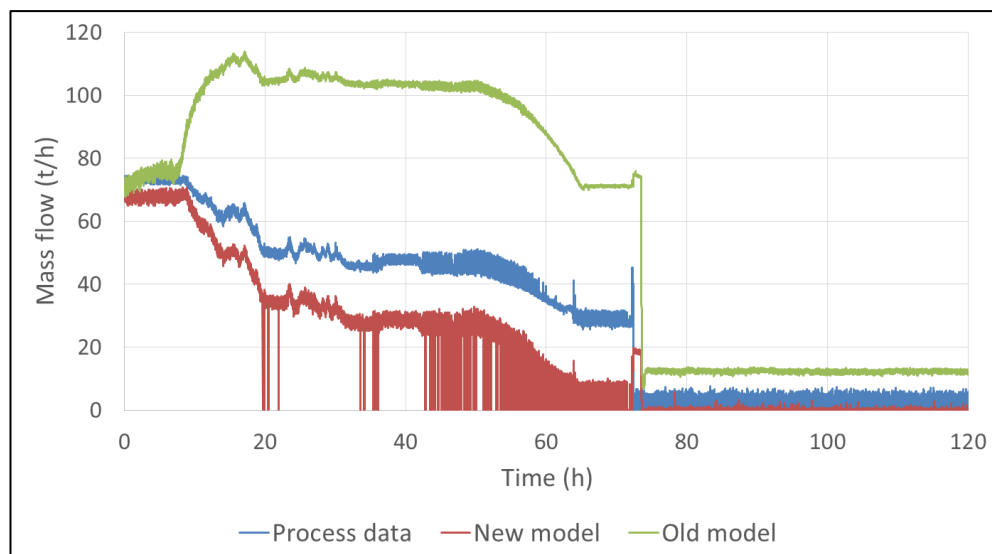
Figure 35. Test result for the suction mass flow of the shutdown case using the SRK equation of state. "New model" refers to the developed model while "Old model" refers to the existing compressor model in ProsDS.

60

The outlet temperature predicted by the new model, depicted in Figure 36, seems quite good and, rather interestingly, the prediction seems to improve in accuracy towards the end of the test. That is, until the compressor is turned off. At this point, the temperature spikes and starts oscillating quite violently. This can be seen in Figure 37. According to the process data in Appendix M, the inlet temperature exceeds the outlet temperature at this point, while both the inlet and the outlet pressure fall close to zero. It is thus no wonder the outlet temperature predicted by the model behaves in a strange manner at these conditions, as the calculation is based on both the inlet temperature and the pressure ratio. At this point the model should be told that the machine has been shut off and that it should stop calculating the outlet temperature in this manner.

The temperature calculation of the old model works quite well. The shape of the predicted curve is very similar to that of the process data, even though there is an offset between the two when using the SRK equation of state. During normal operation, this prediction is slightly better than the new model's prediction, but as the conditions diverge from normal operation the new model clearly gives a better prediction. The old model suffers from even heavier oscillations in the temperature as the machine is turned off.
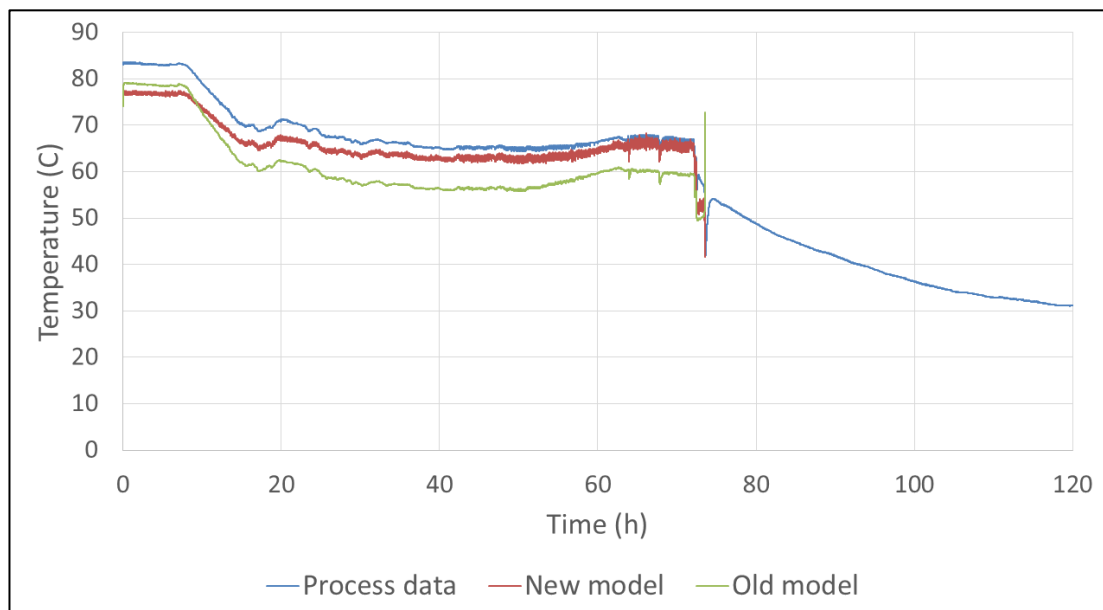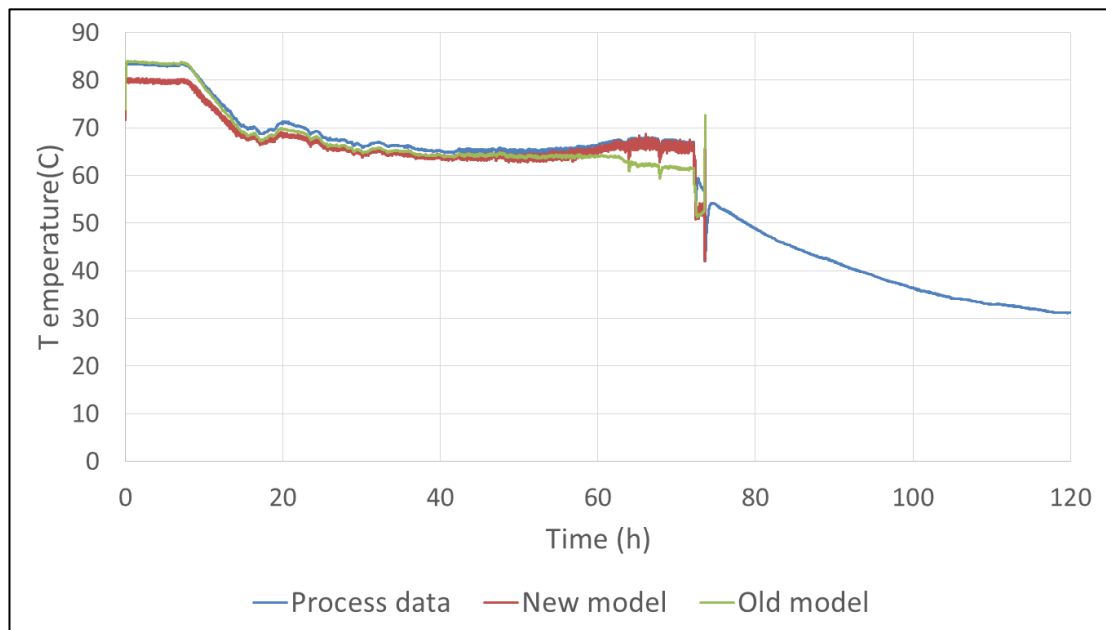

Figure 36. Test results for the compressor outlet temperature of the shutdown case using the SRK equation of state. The predicted graphs have been cut before spiking to better visualize the normal operation.
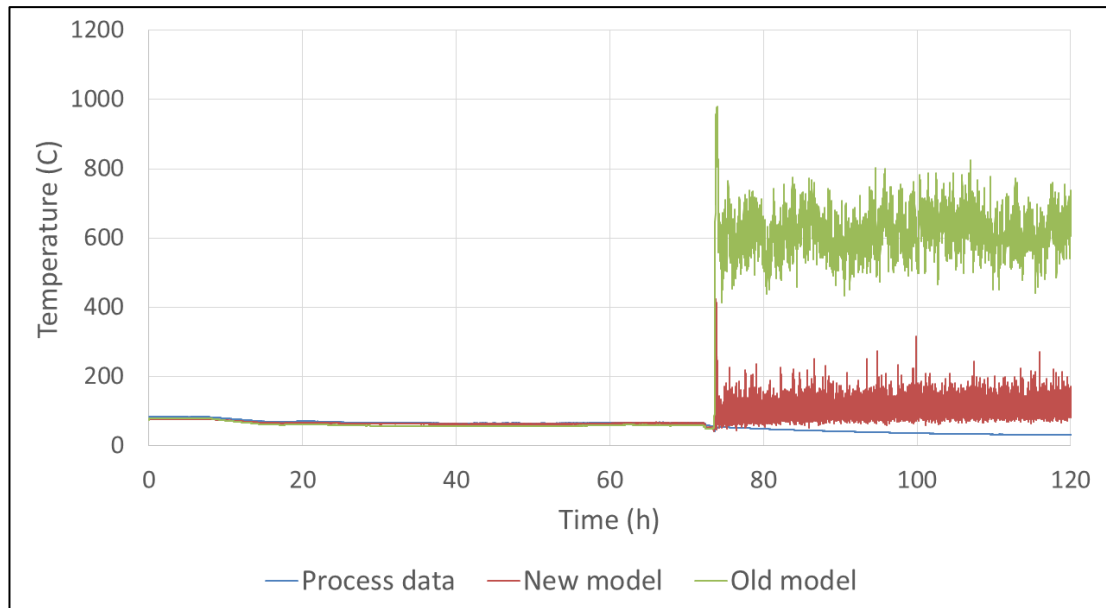
Figure 37. Full range of the SRK shutdown case outlet temperature predictions detailing the spikes and elevated values of the model.

The new model's prediction of the electric current is rather good throughout the entire test, as displayed in Figure 38. It does drop to zero at times, which is due to the aforementioned issue of the model balancing on the verge of surge. The predicted current of the old model again differs completely from the process data. It is constantly increasing, until finally doing a massive spike and going into oscillation as the compressor is shut off, as seen in Figure 39.
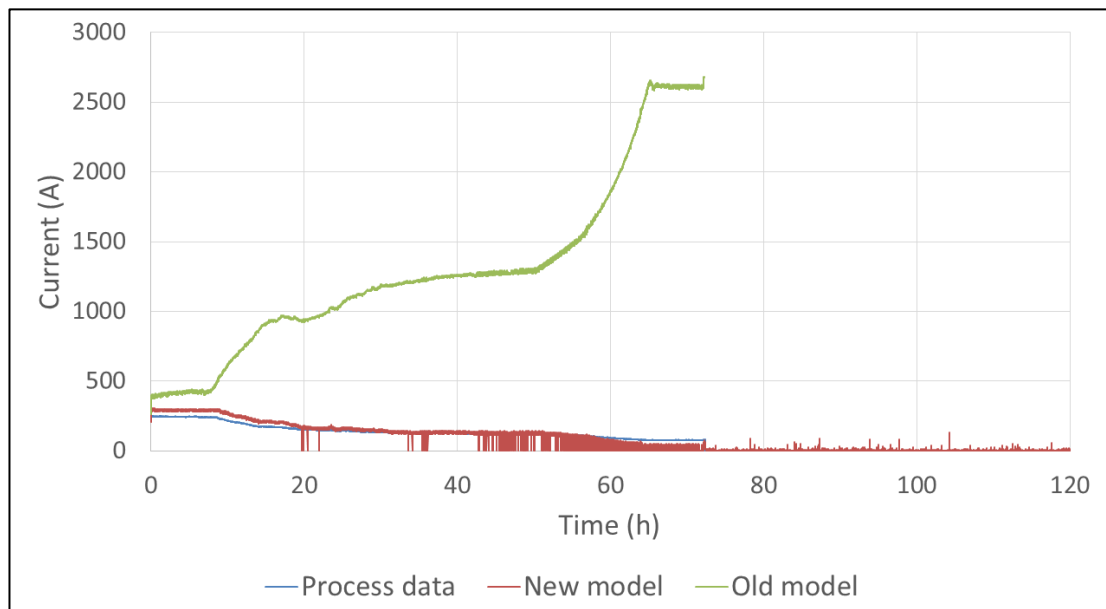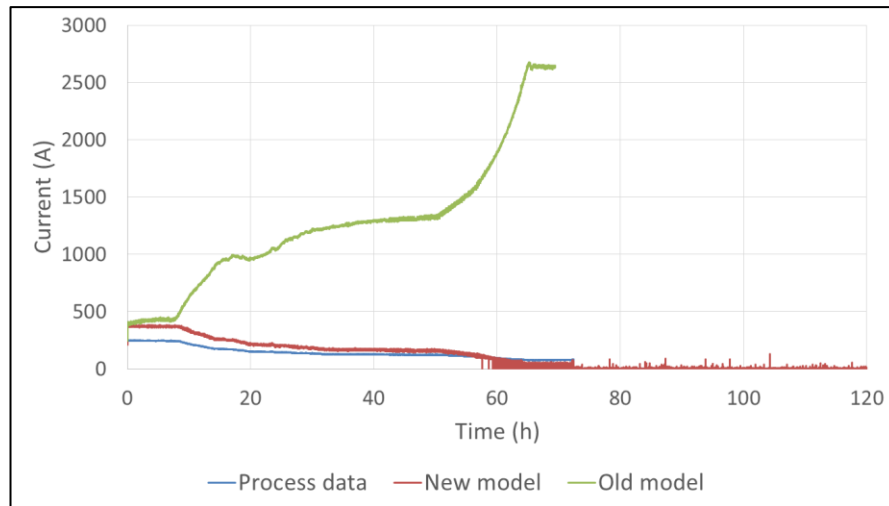

Figure 38. Test results for the compressor electric current of the shutdown case using the SRK equation of state. The predicted graph of the old model has been cut before spiking to better visualize the normal operation.
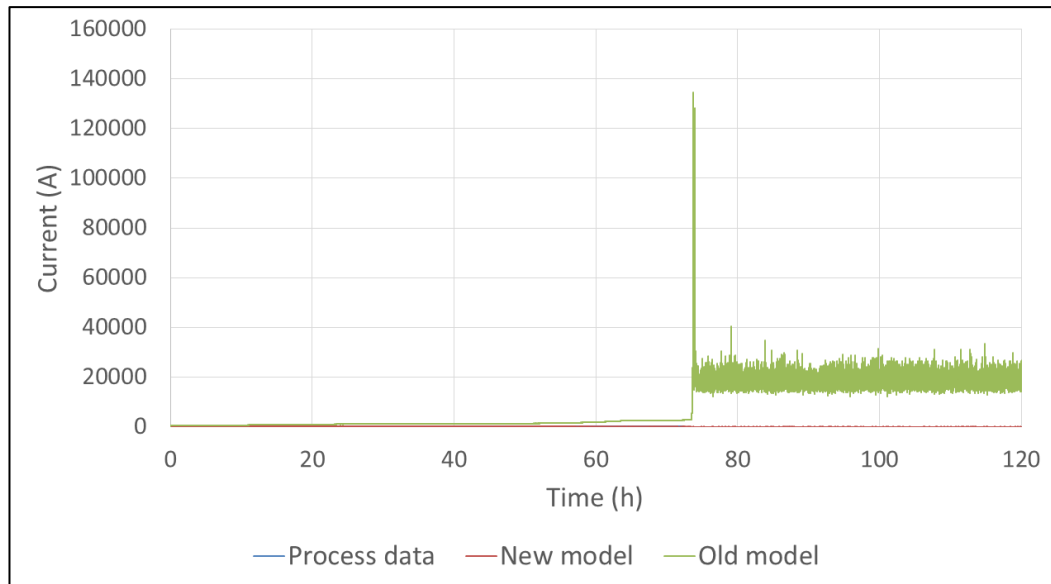
Figure 39. Full range of the SRK shutdown case electric current predictions detailing the spike and highly elevated values of the old model.

When the test was performed using the ideal equation of state, the results, which are displayed in Figure 40 to Figure 42, were similar to the results of the previous test. Nonetheless, certain differences between the two methods were visible. The predicted mass flow initially stayed slightly above the process data flow but fell below it once the operating conditions started to change. The offset between the curves mostly remained smaller than when the SRK method was used. The model started jumping between surge and normal operation only towards the end of the test. The shape of the predicted curve was once again very similar to that of the process data. The old model appears to behave in the same manner as previously.
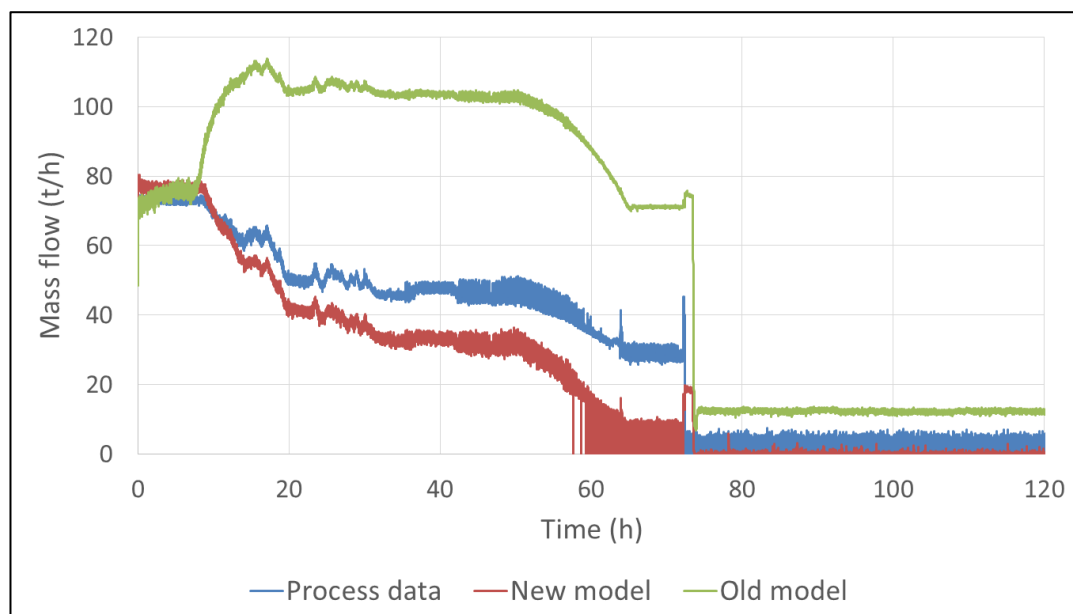
Figure 40. Test result for the suction mass flow of the shutdown case using the ideal equation of state.

A resemblance can also be seen between the temperature predictions of both cases. The offset between the predicted curve and the process data is somewhat smaller when using the ideal equation of state and the shape of the curves seem similar, as seen in Figure 41. For the most part of the test the old model manages to predict the outlet temperature very well. Predictions of the new model are better than those of the old model only towards the end of the normal operation, before the machine is shut off. Both predictions spiked in the same manner as in Figure 37 also in this test. It is worth noting that the correction with Z used in Equation 96 is effectively not active in this test, as Z will have a value of 1 when the ideal equation of state is used.

Figure 41. Test results for the outlet temperature of the shutdown case using the ideal equation of state. The predicted graphs have been cut before spiking to better visualize the normal operation.

The predicted electric current initially lies above the process data with a bigger offset than in the SRK test case but approaches the process data curve towards the end of the operation, as seen in Figure 42. Figure 24 gave some indication of such behavior of the model, although it would suggest a bigger offset for the SRK test. The reason for a larger offset in the ideal test case is likely the higher predicted mass flow and slightly higher outlet temperature. The current consumption of the old model behaves in the same way as in the SRK test and also spikes in the same manner as in Figure 39.
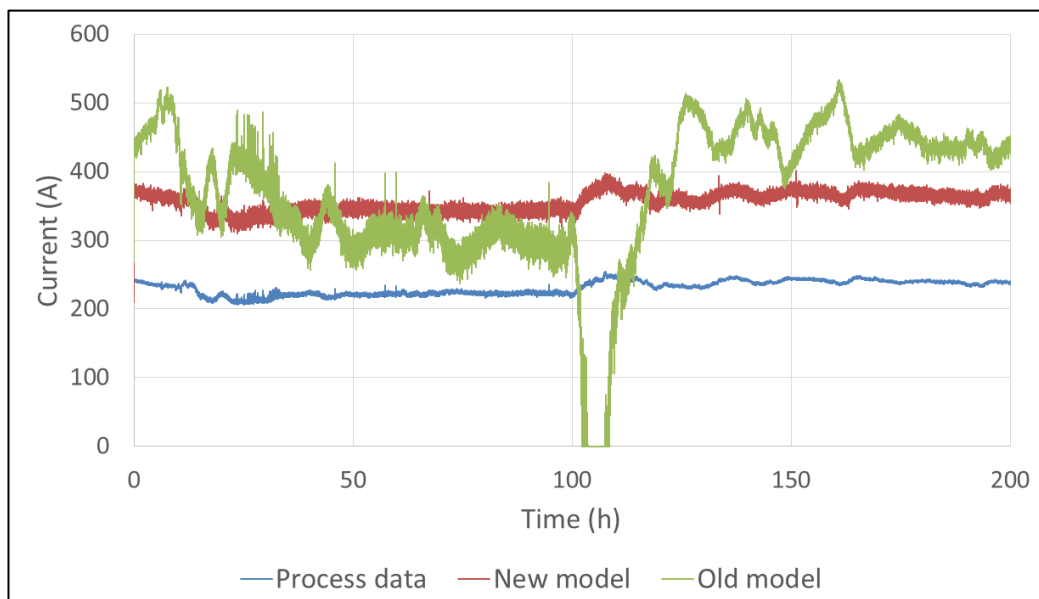
Figure 42. Test results for the compressor electric current of the shutdown case using the ideal equation of state. The predicted graphs have been cut before spiking to better visualize the normal operation.

As particularly the flow predictions seemed better when the ideal equation of state was used, the same method was used for the two remaining test cases. Next in order was the normal operation case, where the capacity of the compressor varied to some extent. The results of the test can be seen in Figure 43, Figure 44 and Figure 45. The observations of the developed model's performance from the previous cases largely held true also for this test.

The predicted mass flow lies a bit above the process data and would seem to follow the shape of the latter rather nicely. Same goes for the outlet temperature prediction, which lies a few degrees beneath the process data curve. A slight concern is the predicted electric current. The shape of the curve is satisfactory, but it is situated quite a bit above the process data curve.

Figure 43. Test result for the suction mass flow of the normal operation case using the ideal equation of state.

65

The behavior of the old model is certainly rather perplexing, as nothing in the process data would seem to warrant such a sudden drop in the flow and the consequent radical rise, nor the swinging nature of the curve. The old model's prediction of the outlet temperature is very good for most of the test, save for the part where the flow drops to zero. At this point the temperature also drops, albeit not as much as the mass flow. The electric current prediction follows the same pattern as the mass flow prediction, exhibiting fluctuating behavior and suddenly dropping to zero for a while.
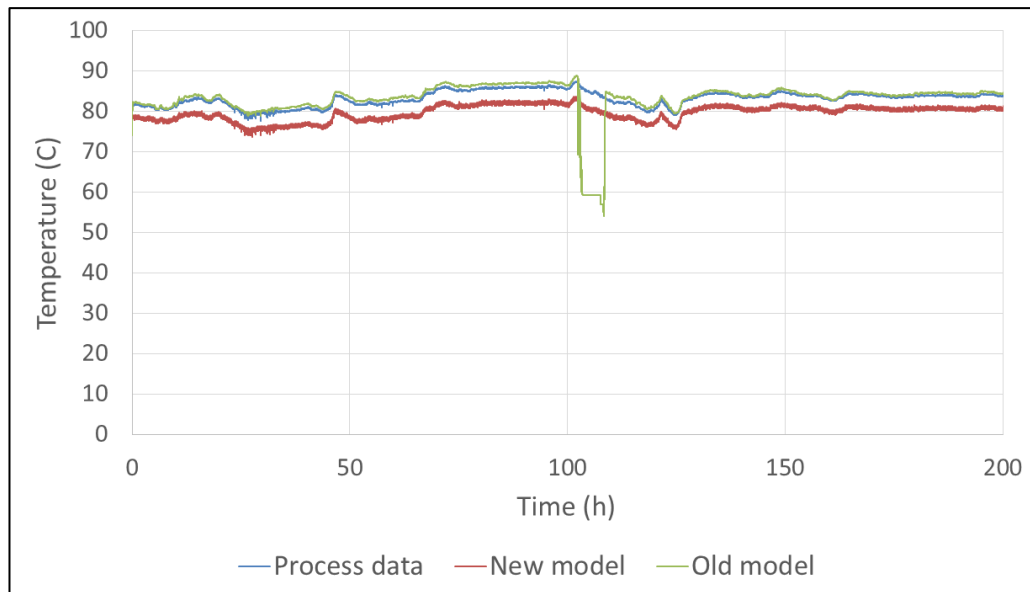
Figure 44. Test results for the outlet temperature of the normal operation case using the ideal equation of state.

Figure 45. Test results for the compressor electric current of the normal operation case using the ideal equation of state.

The last case in the process data test series was the startup operation. The results, displayed in Figure 46, Figure 47 and Figure 48, was mainly consistent with the results from previous tests. A noticeable difference was that the new model predicted full surge operation for some time during the startup before exhibiting the previously encountered behavior of jumping between surge and normal operation. For the rest of the test the shape of the predicted curve followed that of the process data, starting off somewhat below it and rising slightly above towards the end.
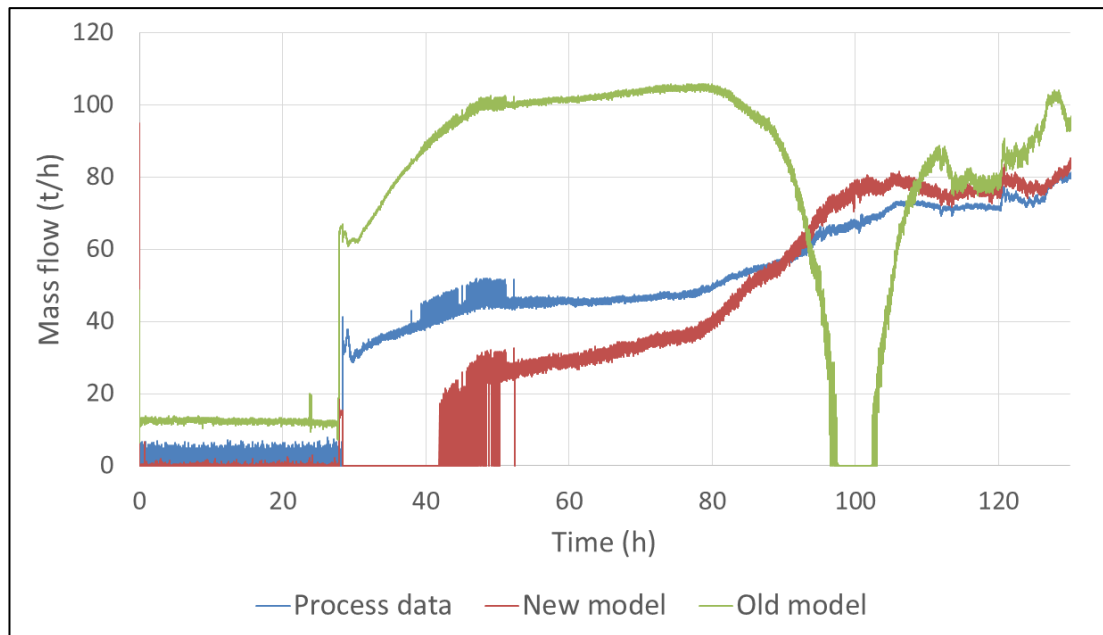
Figure 46. Test result for the suction mass flow of the startup case using the ideal equation of state.

The outlet temperature of the new model matched the process data well, with a minor increase in the offset towards the end of the test case. The same behavior displayed in Figure 37 was again present. Once the model started predicting normal operation the current prediction initially worked well, but as was the case in both of the previous test where the ideal equation of state was used, the offset increase is a bit excessive when moving closer to normal operating conditions for the compressor.

The behavior of the old model is again detached from the process data and seems to combine elements of the results for the shutdown and normal operation cases. The old model correctly predicts the inception of flow through the machine, but it starts off at a much higher level. After this, the flow rises to a higher level which is then maintained for quite some time, similar to the behavior in the shutdown case. Once the flow starts to decline it drops all the way to zero, much like in the normal operation case. The flow stays at zero for a while before rapidly rising back to a level above the process data, where it starts to fluctuate in a similar manner as in the normal operation case.

The discharge temperature prediction of the old model exhibited the same oscillating behavior at an elevated level as in Figure 37 while the machine was shut off. After normal operation started, the prediction was a decent match to the process data, improving as conditions neared normal operation. A drop in the temperature occurred as the flow dropped to zero, similar as in the normal operation case. The predicted current initially follows the same pattern as in Figure 39. It remains at a high level for the duration of the test, shortly dropping to zero along with the flow prediction before rising up again.
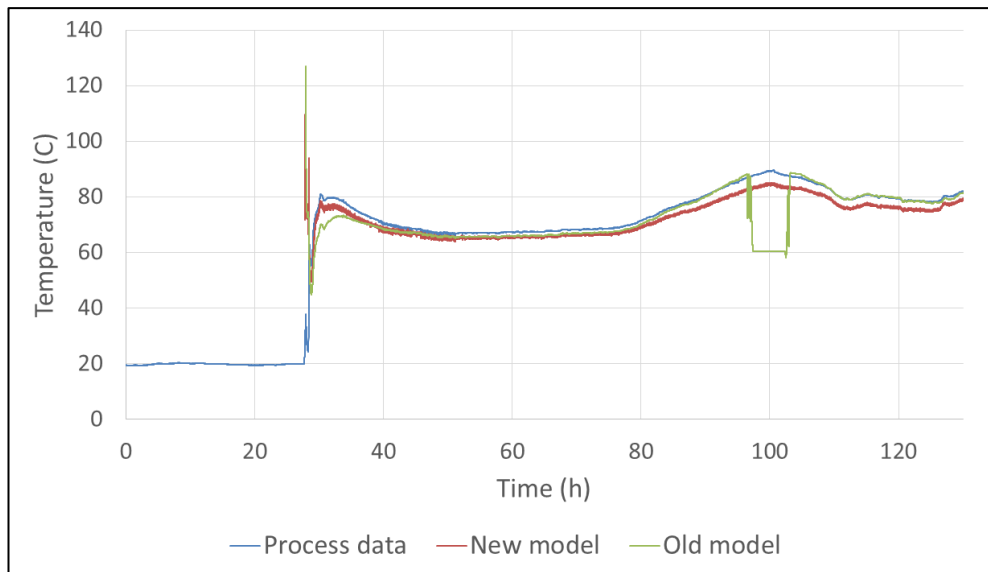
Figure 47. Test results for the outlet temperature of the startup case using the ideal equation of state. The spikes of the predicted graphs have been cut to better visualize the normal operation.
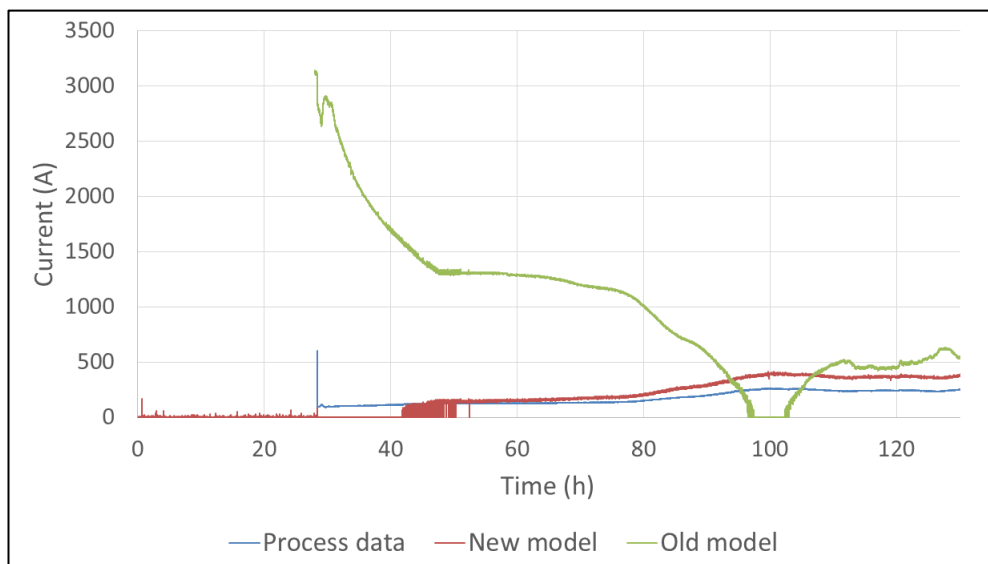
Figure 48. Test results for the compressor electric current of the startup case using the ideal equation of state. The spike of the predicted graph of the old model has been cut to better visualize the normal operation.

5 Results

Upon inspection of the figures in section 4.2.2 it is clear that the developed model is stable over a wide range of operating conditions, supporting the feasibility of the selected method of modeling the compressor operation. When examining the tests and figures of section 4.2.3, it can be found safe to claim that modeling of the compressor flow and required electric current were substantially improved by the developed model.

The flow and outlet temperature calculations of the new model performed better when using the ideal equation of state, while the electric current calculation fared better when the SRK equation of state was used. When using the SRK method the outlet temperature predicted by the developed model seemed better compared to the old model's prediction. When the ideal equation of state was used, however, the outlet temperature predicted by the old model described the process data more accurately for the most part of the test. The accuracy of the new model's temperature prediction was better only shortly before the machine was shut off or shortly after it was turned on.

When studying the graphs in the aforementioned sections, the possibility of inaccuracies and various uncertainties pertaining to both the manufacturer data and the measured process data should be kept in mind. Albeit the developed model overall appears to be a clear improvement, it still suffers from certain shortcomings and requires further development to overcome these issues.

5.1 Issues

The main issue discovered in the developed model was the offset between the predicted flow and the process data, which grew in size as the operating conditions diverged from the normal operating state. The nature of the operating curve predictions and the difference between the calculated values for κ and Z and the values provided by the manufacturer were identified as possible causes for this behavior of the model.

The model could be seen balancing on the verge of surge during the shutdown and startup test cases. During the startup case the model also initially predicted full surge for some time. These issues are caused by the poor accuracy of the predicted performance curves at these operating conditions, but to avoid having the model jump between surge and normal operation for extended periods of time, the limit of the exit flow coefficient used to predict the onset of surge could be given a smaller value. This would move the surge limit a little to the left on the operating curves and the model would not be balancing right on the limit, as it now can be seen doing for certain parts of the shutdown and startup tests.

Another issue encountered during the shutdown and startup tests was elevated and oscillating predictions of the outlet temperature when the machine was not running. When the machine is not running the model should not be calculating the outlet temperature. Lastly, the model calculated a too high current consumption for the machine when the ideal equation of state was used. The power calculation should altogether be improved, as it was implemented in a rather simple manner, using only the transported mass flow and the difference between the inlet and outlet flow enthalpies.

5.2 Suggestions for future improvements

Based on the results of the various tests performed for the developed model several areas of improvement were identified. These subjects mainly relate to the operating curve, outlet temperature calculation and power calculation, but some entirely new features are also suggested. Certain features have already been introduced in Chapter 2, but some new concepts are also presented.

5.2.1 Improvements of the operating curve calculation

There are a number of approaches to address the most serious issue with the model, which is the inaccuracy of the flow calculation. Firstly, as the compressibility could be calculated in the simulator, the simplified form of Equation 52 used in the model could be expanded to use the

average compressibility instead of just the inlet compressibility. The outlet compressibility could also be used to expand Equation 92 into its full form of Equation 48. The use of the compressibilities of course require that some other equation of state than the ideal is used. Similar problems as with the values of the inlet compressibility and the ratio of specific heat would likely also be encountered with the outlet compressibility.

Since the difference in the calculated values of Z and κ compared to the manufacturer values resulted in slightly reduced volume flow predictions, a second improvement to the flow prediction accuracy may be achieved by using the values calculated by the simulator for Z and κ already in Excel when transforming the manufacturer curves to the dimensionless curves. That way, the transformed dimensionless curves would match the values calculated for Z and κ by the simulator.

A third method would be to address the issue of the curve predictions seemingly being increasingly reduced as the operating conditions diverge from the rated conditions. As was discovered during the initial testing of compressors A and B, the temperature exponent m is a powerful parameter for controlling the shape of the dimensionless curves and the predictions made from these. In the developed model m_{corr} was used as a tuning parameter to adjust the temperature exponent when aligning the dimensionless curves. As the stage performance curves are supposed to follow only the Mach numbers according to the literature, a possible approach may be to scale m_{corr} based on the relation of the governing Mach number in the machine to the Mach number pertaining to the dimensionless curve used in the model. By decreasing the value of m_{corr} the reduced curves could be pushed further to the right-hand side of the coordinate system, closer to the manufacturer curves.

The fourth and final suggestion for a way to improve the flow calculation is to scale the polytropic efficiency used in the flow calculation to match the governing process conditions. This in turn can be implemented by a handful of different methods. In the model the curves of the head coefficient and polytropic efficiency plotted against the exit flow coefficient of the rated case were used for predicting the operating curves at other operating conditions. As the prediction for the initial circulation case seemed to differ the most from the manufacturer data, this case was selected for further polytropic efficiency scaling studies in Excel. The results of these tests are displayed in Figure 49 and Figure 50 with a m_{corr} value of one and in Figure 51 and Figure 52 with a value of 3.2 for m_{corr}. Substantial improvements in the predictions in the first case would mean that m_{corr} would be made obsolete, while improvements in the second case would imply that the accuracy of the developed model can be enhanced by scaling the efficiency.

"Eta, rated case" and "Eta, initial circulation" in Figure 49 are the manufacturer efficiency curves transformed to dimensionless form. The initial thought was that an extension of the initial circulation efficiency curve into the exit flow coefficient values of the rated case would yield a good prediction for the operating curve. Initially, the value of the first point of "Approximated Eta" in Figure 49 was approximated in this manner and each consecutive value of the efficiency was reduced by one percent. This yielded a poor result, so the initial value was adjusted until "Initial Circ. prediction, approximated Eta" in Figure 50 matched the manufacturer curve "Initial Circ." as well as possible. Even though the approximation was far from a perfect fit, Figure 50 showed that it was still considerably better than the current prediction of the developed model, "Initial Circ. prediction", demonstrating that the polytropic efficiency significantly influences the operating curves and thus proving the feasibility of the approach.

To form an idea of the shape of the actual efficiency curve needed to obtain a good prediction for the initial circulation case operating curve from the rated case dimensionless operating curve, "Initial Circ. prediction, fitted Eta, mcorr=1" was empirically matched to the manufacturer curve by adjusting the values of "Fitted Eta, mcorr=1" in Figure 49 one by one. Attempts were made to use exit flow coefficient values scaled with Equation 98, both alone and in conjunction with scaled efficiency values, to obtain a desirable polytropic efficiency curve. The efficiency values were supposed to be scaled with Equation 99 in this case, but Equation 100 was accidentally used. The "φ3 scaled" and the "φ3 & Eta scaled" in Figure 49 both proved to be poor matches and extensions for the empiric curve and, thus, further attempts to use exit flow coefficient scaling for this purpose were abandoned and no attempts to predict operating curves using these efficiency curves were made.

Scaling only the polytropic efficiency using Equation 99, however, yielded rather promising results. The curve obtained by this, "Eta scaled", lied just below the fitted curve and the predicted operating curve "Initial Circ. prediction, scaled Eta" was situated slightly to the left of the actual operating curve. The predicted curve can be seen to turn backwards, but the developed model would cut off the curve at the point it starts turning, resulting in a curve bearing a good resemblance to the performance curve provided by the manufacturer. The curves "Eta scaled, mcorr" and "Fitted Eta, mcorr=3.2" in Figure 49 as well as curves "Initial Circ. prediction, scaled mcorr Eta" and "Initial Circ. prediction, fitted Eta, mcorr=3.2" in Figure 50 are related to the scaling test where m_{corr} is used.
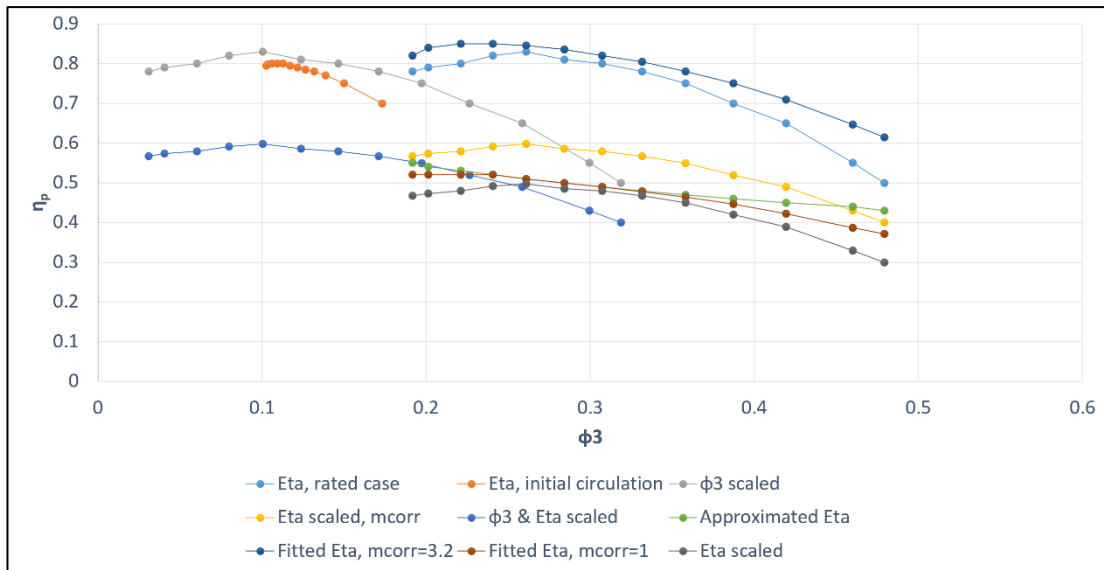
Figure 49. Various attempts to scale the dimensionless polytropic efficiency of the rated case for use in the prediction of the initial circulation case of compressor C, with a value of 1 for m_{corr}. The actual efficiency curves provided by the manufacturer for the rated and the initial circulation case are also included for reference.
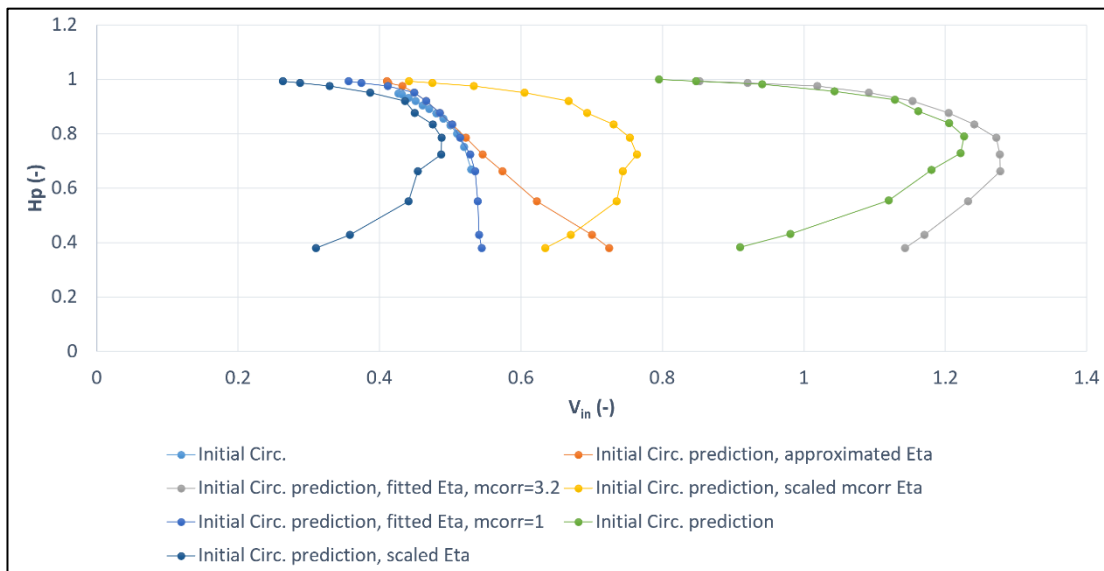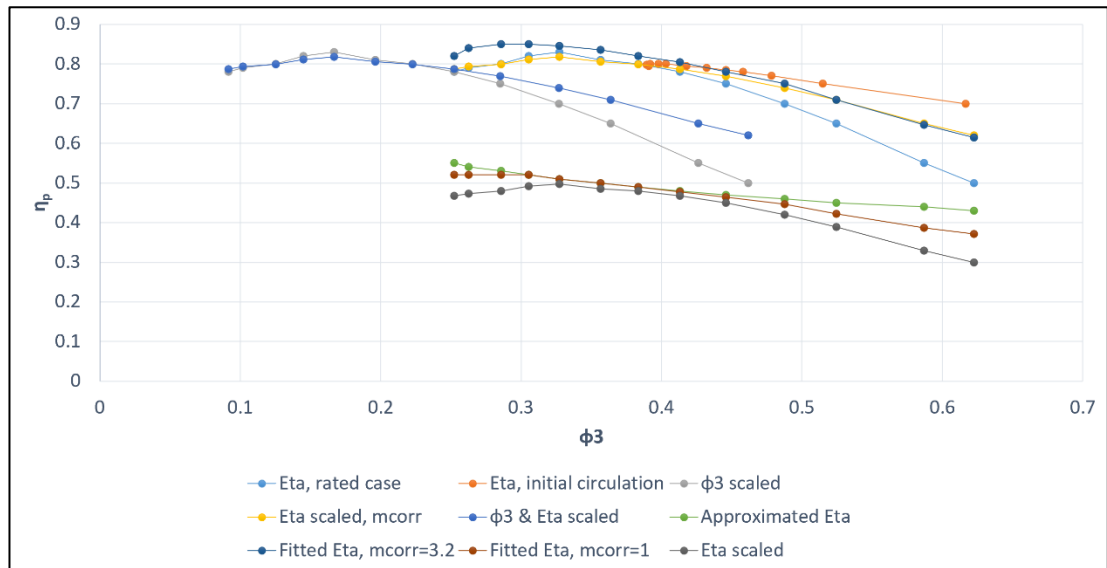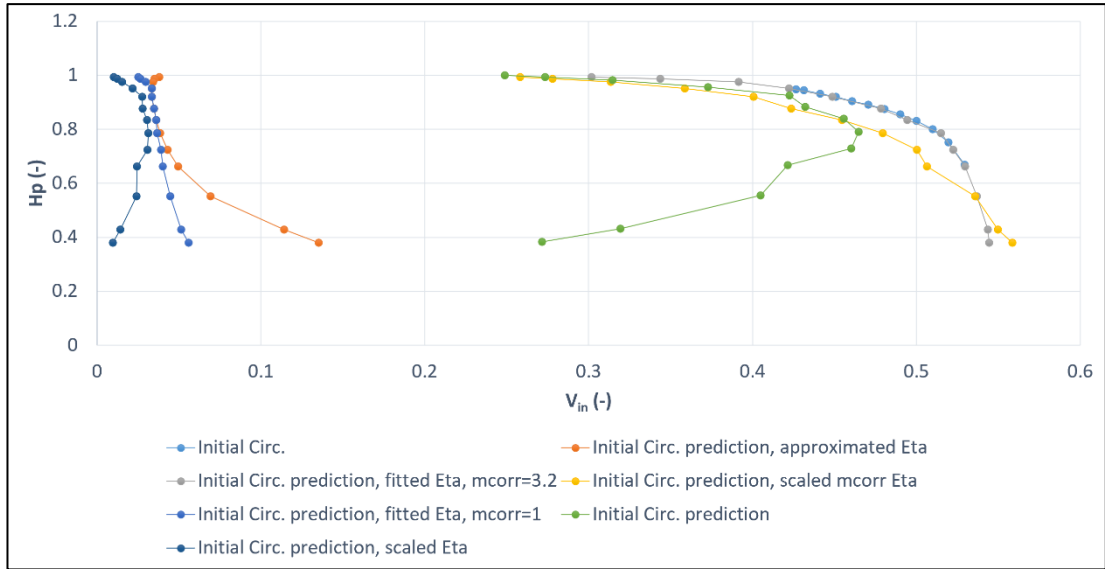

Figure 50. Attempts to predict the initial circulation operating curve using various polytropic efficiency curves with a value of 1 for m_{corr}. The actual performance curve provided by the manufacturer is also included for reference.

$$\varphi_{3,scaled} = \varphi_{3,rated} - \left(M_{u,init.circ.} - M_{u,rated}\right)\frac{M_{u,rated}}{M_{u,init.circ.}} \tag{98}$$

$$\eta_{p,scaled} = \eta_{p,rated}\frac{M_{u,init.circ.} - M_{u,rated}}{M_{u,init.circ.}} \tag{99}$$

$$\eta_{p,scaled,mcorr} = \eta_{p,rated}\frac{M_{u,init.circ.} - M_{u,rated}}{M_{u,init.circ.}} + \frac{m_{corr}}{10} \tag{100}$$

The results of the scaling test for the case where m_{corr} is used are presented in Figure 51 and Figure 52. The curves are the same as in the previous figures, but their shapes have been altered by the effect of m_{corr}. The curves "Fitted Eta, mcorr=3.2" and "Initial Circ. prediction, fitted Eta, mcorr=3.2" were obtained by a similar empiric procedure as in the previous test. In order to account for the use of the correction factor, Equation 99 was expanded to Equation 100, which was used to obtain "Eta scaled, mcorr" in Figure 51. This efficiency curve was used in the calculation of "Initial Circ. prediction, scaled mcorr Eta" in Figure 52. The prediction lies close to the manufacturer curve, but it is not perfect. It is still located to the left of the actual operating curve and the operating range of the prediction is too wide. It seems that the scaling did not work as well when m_{corr} was used.

Figure 51. Various attempts to scale the dimensionless polytropic efficiency of the rated case for use in the prediction of the initial circulation case of compressor C, with a value of 3.2 for m_{corr}.

Figure 52. Attempts to predict the initial circulation operating curve using various polytropic efficiency curves with a value of 3.2 for m_{corr}.

The equations used in the scaling tests bear some resemblance to the equations used in another method for predicting the polytropic efficiency at a given operating point. The ratio of the efficiency to the peak efficiency is a function of the tip-speed Mach number and the ratio of the inlet flow coefficient to the maximum flow coefficient at the choke point, as shown in Equation 101. [42, p. 2]

$$\frac{\eta}{\eta_{peak}} = f\left(\frac{\varphi_1}{\varphi_{1,c}}, M_u\right) \tag{101}$$

The stage efficiency as a function of flow at varying Mach numbers can be modeled as a modified elliptic curve. For flows below the maximum efficiency point the function is described by Equation 102, where E is a coefficient that varies with the Mach number. Typical values for E range from 1.7 to 2.1 for high respective low speed characteristics. [42, p. 3]

$$\frac{\eta}{\eta_{peak}} = \left(1 - \left(1 - \frac{\varphi_1/\varphi_{1,c}}{\varphi_{1,peak}/\varphi_{1,c}}\right)^E\right)^{1/E} \quad for \; \varphi_1 < \varphi_{1,peak} \tag{102}$$

If the flow is greater than at peak efficiency the function is described by Equation 103, where A and B are similar coefficients as E, varying with the Mach number. B usually assumes values between 2 and 3.5 for low respective high speeds, while usual values for A lie between 0.3 and 2 for high respective low speed characteristics. [42, p. 3]

$$\frac{\eta}{\eta_{peak}} = (1 - A) + A\left(1 - \left(1 - \frac{\frac{\varphi_1}{\varphi_{1,c}} - \frac{\varphi_{1,peak}}{\varphi_{1,c}}}{1 - \frac{\varphi_{1,peak}}{\varphi_{1,c}}}\right)^B\right)^{1/B} \quad for \; \varphi_1 > \varphi_{1,peak} \tag{103}$$

Another method makes use of both the inlet flow coefficient and the exit flow coefficient to shift the point of peak efficiency. Equation 104 is used to shift the best efficiency point to smaller flow coefficient values for Mach numbers below the rated point Mach number. At Mach numbers exceeding the rated point, Equation 105 is used to shift the point of maximum efficiency to lower exit flow coefficient values. [19, p. 139]

$$\varphi_1 \approx \frac{\left(\dot{V}_3/\dot{V}_1\right)_{RP}}{\dot{V}_3/\dot{V}_1} \varphi_{1,RP} \tag{104}$$

$$\varphi_3 \approx \frac{\dot{V}_3/\dot{V}_1}{\left(\dot{V}_3/\dot{V}_1\right)_{RP}} \varphi_{3,RP} \tag{105}$$

A final method is to use an iterative calculation for determining the polytropic efficiency at the governing process conditions. First, the polytropic efficiency is determined as a function of the gas properties according to Equation 106. To avoid rounding errors in the compressibility functions Y and X these are calculated with Equations 107 and 108. The volume polytropic exponent n_V is calculated with Equation 109, where κ_T is the temperature isentropic exponent and n_T is the temperature polytropic exponent, which in turn is given by Equation 110. This equation itself contains the polytropic efficiency, which contributes to the iterative nature of the method. [43, p. 8502]

$$\eta_p = \frac{n_V Y(1 - \kappa)}{(1 + X)\kappa - n_V Y(X + \kappa)} \tag{106}$$

$$Y = \frac{1}{n_V} + n_T(1 + X) \tag{107}$$

$$X = \frac{C_p}{ZR}\frac{\kappa_T - 1}{\kappa_T} - 1 \tag{108}$$

$$n_V = \frac{\kappa_1}{1 + \frac{C_p(\kappa_1 - 1)}{Z_1 R}\left(\frac{1}{n_T} + \frac{\kappa_1 - 1}{\kappa_1} - 1\right)} \tag{109}$$

$$n_{T,new} = n_{T,ref} \frac{1 - \frac{Z_{ref}R}{C_{p,ref}}\left(\frac{1}{\eta_p} - 1\right) - \frac{\kappa_{ref}}{\kappa_{ref} - 1}}{1 - \frac{Z_{new}R}{C_{p,new}}\left(\frac{1}{\eta_p} - 1\right) - \frac{\kappa_{new}}{\kappa_{new} - 1}} \tag{110}$$

To incorporate the effects of the compressor itself in the polytropic efficiency, the obtained value is further iterated to correct the efficiency based on the flow coefficient and the Mach number. The value calculated for the efficiency in the previous step is used to calculate the polytropic head. If the flow coefficient changes from its design value, Equation 111 is used to correct the polytropic efficiency previously calculated in Equation 106. [43, pp. 8502-8503]

$$\eta_{p,new} = \eta_{p,ref} \frac{S_{ref}}{S_{new}} \frac{H_{p,new}}{H_{p,ref}} \frac{U_{ref}^2}{U_{new}^2} \tag{111}$$

If any of the presented methods for improved prediction of the polytropic efficiency at off-design operation can be incorporated in the developed model with satisfactory accuracy, the flow predictions would significantly improve even if the dimensionless performance curves would not be aligned, making m_{corr} largely obsolete.

5.2.2 Improved modeling of the operating curve limits

For more realistic behavior of the model, modeling of the surge and stonewall operation should be further developed. In the model both the surge and stonewall were implemented as a limit value for the exit flow coefficient. As the process data test results for the model demonstrated, the selection of the limits should be reviewed. In addition, the behavior of the model outside of the normal operating range should be developed in the direction of the behavior described in sections 2.2.2 and 2.2.3, instead of simply limiting the flow or stopping it all together.

Simulation of pre-surge perturbations has been achieved with a one-dimensional flow model, consisting of a set of nonlinear ordinary differential equations. The model makes a quasi-steady assumption and requires a system geometry distribution, element characteristics, inlet conditions and working fluid data to be able to solve the equations. It is thought that the model would be able to simulate full surge cycles, should negative flow characteristics of the compressor be available. [44]

5.2.3 Improved calculation of the outlet temperature

It may be worth looking into replacing the compressibility used as a correction in the outlet temperature calculation with the polytropic efficiency. This would at least have the benefit that the correction would have an effect even if the ideal equation of state is used. The model should also know when the machine is shut off and stop calculating the outlet pressure at this point. This would prevent most of the spikes and oscillations in the temperature predictions now visible in the tests, but some other safeguards may also be needed. Implementation of a power switch to the model should be a trivial matter.

5.2.4 Enhanced power calculation

The tests showed that the power calculation worked rather well when the SRK equation of state was used. However, when the equation of state was switched to ideal, the calculated power at normal operation was quite high compared to the process data. The model should also account for various losses during the compression process, so an efficiency should be added for this purpose.

Using one of the presented options in section 2.2.5, such as Equation 72 or 76, could work well as an improvement. It would be particularly interesting to investigate the use of the work input factor, presented in Equations 77 and 78 , in more detail as this factor is also linked to the exit flow coefficient, which is the backbone of the developed model. The work input factor equations are strictly valid for a single compression stage, so some correction will likely be needed if it is used to describe compression in a multi-stage machine.

5.2.5 Additional features

In addition to the several improvements mentioned above, the developed model could benefit from some entirely new features. In the current implementation in ProsDS the effect of adjustable impeller inlet guide vanes was modeled. This modeling, along with adjustable diffuser vanes, could also be added to the developed model. Adjustable inlet guide vanes are a form of regulation that can offer a wider operating range and higher efficiency for the compressor. The row of inlet guide vanes is positioned before the impeller and can be used to create a negative of positive prerotation of the gas. As Figure 53 shows, positive prerotation reduces the head while negative prerotation increases it, to some extent. Positive prerotation shifts the entire operating curve to smaller volume flows. [19, pp. 79-80, 118-120]

The adjustable diffuser vanes are located downstream of the impeller. They contribute with a more efficient transformation of the kinetic energy. As Figure 54 shows, use of adjustable diffuser vanes enables a much wider operating range at constant pressure ratio by stabilizing the flow in the diffuser. [19, pp. 120-121]
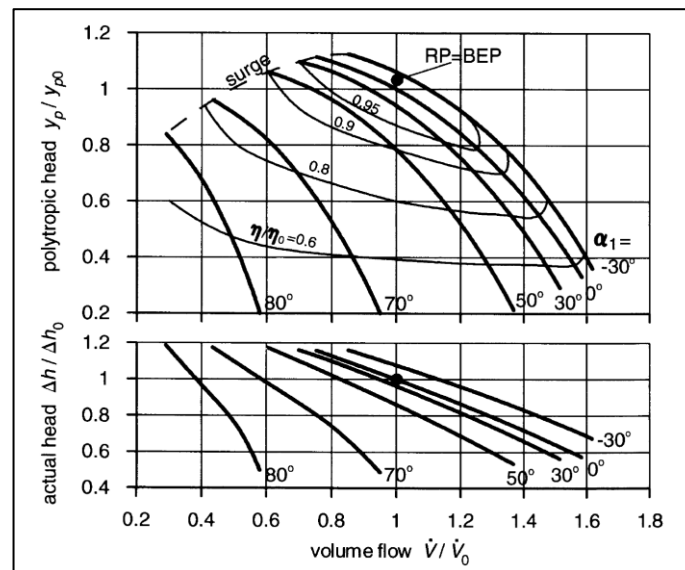
Figure 53. Effect of adjustable inlet guide vanes on a single-stage performance map, α_1 denotes the inlet guide vane angle. [19, p. 119]
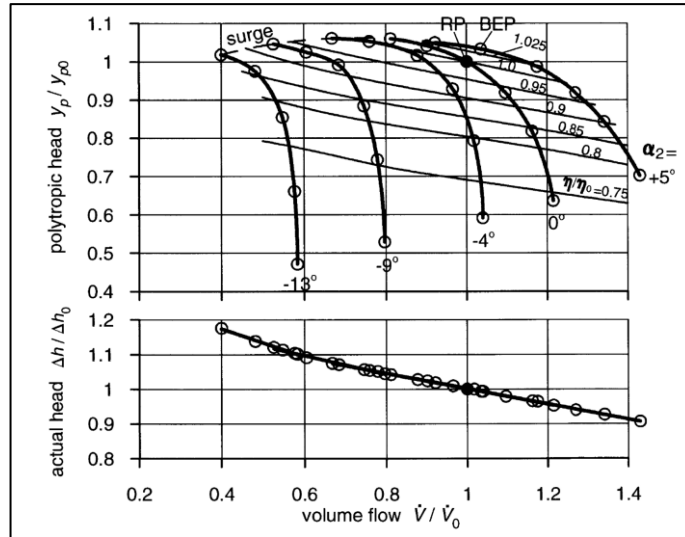
Figure 54. Effect of adjustable diffuser vanes on a single-stage performance map, α_2 denotes the diffuser vane angle. [19, p. 121]

6 Summary

The central status of the pumps, compressors and turbines for the process industry warrant an interest in detailed dynamic modeling of the equipment. The methods used to model the equipment in a dynamic operator training simulator should be both accurate over a wide regime of operating conditions and computationally relatively light. The underlying theory and principles of the pumps, compressors and turbines was presented. The machines shared many similarities both in construction and working principles, but each machine also had its individual characteristics. Among these characteristics, cavitation for pumps, surge and stonewall for compressors and condensation for turbines could be mentioned. Various approaches to model the operating curve, outlet temperature and power consumption or generation of the machines were presented. The focus lied on describing the function of the compressor. The modeling currently implemented in ProsDS as well as approaches used in other simulator software for the mentioned machines was also briefly presented.

Due to the requirements of accuracy and computational efficiency, as well as ease of implementation, it was desirable to find either a single invariant operating curve able to describe the function of the compressor, or a version of the affinity laws valid for the compressor. The method coming closest to these criteria was converting the operating curves to a dimensionless form using the head coefficient and the exit flow coefficient. The task appeared to be a bit of a snipe hunt as, regrettably, the dimensionless curves were strictly valid only for a single compression stage. Nevertheless, this method was used as a basis for the developed compressor model.

The constructed model was subjected to rigorous testing both by ramping the inlet and outlet conditions and by feeding it measured process data for three different dynamic operating cases from an actual process plant and comparing the resulting predictions against measured data. The inlet volume flow, power consumption and outlet temperature of the compressor were predicted in the tests. The results were also compared against the predictions of the currently implemented compressor model in ProsDS. During the dynamic ramp tests the model yielded satisfactory results, demonstrating a stable operation over a wide range of operating conditions.

During the process data testing the flow prediction of the new model fared considerably better than the prediction of the current compressor model of the simulator. The developed model captured the correct shape of the curve rather well and the predictions were quite accurate at normal operation. Some further development is however needed, as the predicted flow dropped too low during the shutdown and startup operations.

The temperature prediction functioned in a satisfactory manner for the most part, but the accuracy could still be improved. When using the ideal equation of state, the temperature prediction of the old model seemed to be more accurate for the most part. The new model seemed more accurate when operating further away from normal operation. The model should also be stopped from calculating the temperature once the machine is turned off.

The electric current prediction of the new model worked better than that of the old one. When using the SRK equation of state the prediction was quite accurate and followed the shape of the process data curve well. However, when using the ideal equation of state the predicted current during normal operation was unreasonably high, although the offset did decrease when the operating conditions diverged from normal operation. A contributing factor to the decrease in the offset is the excessive decrease of the predicted flow, which influences the calculation of the power consumption.

Suggestions for methods to improve the accuracy of the model by developing the calculation of the operating curve, modeling of operation at the curve limits, calculation of the outlet temperature and power consumption as well as ideas for a couple of new features were brought up. Implementation of these should considerably enhance the performance of the compressor model.

In conclusion, the new model, although still requiring some further development, appears to be a clear improvement based on the results of the performed process data tests. To verify that the model can be used as a general approach for compressor modeling, it should still be validated by further testing for several other machines.

7 Svensk sammanfattning

NAPCON, en del av Neste Engineering Solutions, erbjuder en mångfald av mjukvaruprodukter för sina kunder. Dessa produkter avslöjar produktionsanläggningarnas dolda potential och möjliggör deras maximala utnyttjande. En av dessa produkter är en verklighetstrogen dynamisk processimulator, med vilken processoperatörerna kan utbildas till att köra anläggningen. Målet med detta arbete var att förbättra behandlingen av centrifugalkompressorer i simulatorn, samt att lägga grunden för fortsatt förbättring av centrifugalpumparnas och turbinernas modellering. Pumpar och kompressorer utgör centrala delar av processanläggningar, vilket framgår av att en ansenlig andel av energin som förbrukas av industrin går åt till att driva dessa maskiner. Således är det också viktigt att dessa maskiners modeller också beter sig verklighetsenligt.

Centrifugalpumpar och -kompressorer används för att transportera fluider i processanläggningar. Dessa maskiner är både till sin konstruktion och funktionsprincip rätt lika, även om kompressorn kan anses något mer invecklad till följd av det transporterade mediets egenskaper. Maskinerna består av ett hölje samt kopplingar till inloppet och utloppet. Inuti höljet finns en roterande impeller. Impellern kan vara omgiven av en skovelförsedd diffusor, vilken möjliggör mer effektiv omvandling av den kinetiska energin till potentiell energi i form av en tryckökning hos fluiden. Den transporterade fluiden leds in i impellerns mitt, varifrån den slungas ut som en följd av centrifugalverkan. I detta sammanhang ökar flödeshastigheten, och när fluidens hastighet minskar vid utloppet omvandlas den kinetiska energin till en tryckökning.

Maskinerna beskrivs av sina karaktäristikor, där lyfthöjden, verkningsgraden och den förbrukade effekten är uppritade mot volymflödet. För pumpar anges lyfthöjden vanligen som meter vätskepelare. För kompressorer ges lyfthöjden som energi per massaenhet som tillförs flödet mellan kompressorns inlopp och utlopp, eftersom gasernas densitet varierar kraftigt jämfört med vätskornas. Kompression som fenomen beskrivs oftast som isotermisk, isentropisk (adiabatisk) eller polytropisk. Av dessa kan de två första ses som idealiserade gränsfall, medan den polytropiska processen bäst beskriver verkliga kompressionsprocesser. Maskintillverkarna tillhandahåller vanligen kompressorkaraktäristikorna med den polytropiska lyfthöjden och den polytropiska verkningsgraden uppgivna.

Karaktäristikorna som fås av tillverkaren gäller endast vid det uppgivna drifttillståndet. För att kunna förutspå maskinens funktion vid avvikande drifttillstånd bör man veta hur karaktäristikorna påverkas av förändringar i bland annat maskinens varvtal och fluidens temperatur, tryck och molmassa. För pumparna kan maskinens beteende predikteras med hjälp av affinitetslagarna med en rätt god noggrannhet. För kompressorer är dessa dock otillräckliga. I detta arbete utnyttjades en metod baserad på dimensionslösa lyfthjöds- och utloppsflödeskoefficienter vid modellbygget. Denna metod går ut på att ett antal vanliga karaktäristikor kan sammanföras till en enda dimensionslös karaktäristika, ur vilken karaktäristikor för nya drifttillstånd kan beräknas.

Modellen tar koefficienter för ett andra gradens polynom anpassat till den dimensionslösa karaktäristikan som indata. Samma sak görs för ett polynom för den polytropiska verkningsgraden. Modellen avläser utloppsflödets tryck och entalpi samt inloppsflödets tryck, temperatur, molmassa, specifika värmekapacitet, molära volym och entalpi. Med hjälp av dessa beräknar modellen en ny karaktäristika och interpolerar ur det inloppets volymflöde, då utloppstrycket kan anses vara känt. Modellen beräknar även utloppstemperaturen och kompressorns effekt. För beräknandet av utloppstemperaturen används inloppstemperaturen, tryckförhållandet och den polytropiska exponenten korrigerad med gasens kompressibilitet. Effektbehovet beräknades ur strömmarnas entalpidifferens.

Den byggda modellens dynamik testades genom att variera utloppets tryck och inloppets tryck, temperatur samt molmassa över ett brett spektrum. Endast vid väldigt extrema värden, exempelvis nära den absoluta nollpunkten, uppvisade modellen osammanhängande beteende, vilket är föga överraskande. Då värdena varierades kring normala drifttillstånd uppvisade modellen ett robust och sammanhängande dynamiskt beteende.

För att närmare undersöka modellens prediktionsförmåga kopplades strömmarna till en databas med processdata uppmätta som funktion av tiden. Data omfattade utloppsströmmens tryck och temperatur, den elektriska strömmen genom kompressorn samt inloppsströmmens sammansättning, tryck, temperatur och volymflöde. Värdena som modellen behövde för prediktionen lästes ur databasen, medan de predikterade värdena för volymflödet, utloppstemperaturen och elektriska strömmen beräknad ur effekten skrevs till databasen för jämförelse med de verkliga värdena. Den gamla kompressormodellen kördes även parallellt på samma vis för att de båda modellerna skulle kunna jämföras sinsemellan.

Då modellernas predikterade data uppritades mot processdata framgick det att den nya modellen var en klar förbättring. Formen för den nya modellens grafer var mycket nära processdata, medan den gamla modellens grafer avsevärt avvek från processdata och hade helt annat dynamiskt beteende. Det förekom en förskjutning mellan den nya modellens volymflöde

och processens uppmätta volymflöde. Förskjutningen var mindre kring normaldrift, medan den växte då maskinen närmade sig nedstängning eller då den nyligen startats upp. En liten förskjutning kommer från att de beräknade värdena för kompressibiliteten och värmekapaciteternas förhållande i processimulatorn avviker från tillverkarens värden. Orsaken till att förskjutningen växer ju mer man avviker från normaldrift beror på att modellens prediktionsförmåga försämras, eftersom det använda polynomet för den polytropiska verkningsgraden gäller vid normaldriften. För att förbättra prediktionsförmågan borde även verkningsgraden skalas om då driftsförhållandet förändras.

Trots att några smärre förbättringar kvarstår för att förbättra modellens prediktionsförmåga kunde det konstateras att en klar förbättring i noggrannheten och det dynamiska beteendet hade åstadkommits.

8 References

[1]   Neste Engineering Solutions, "NAPCON Simulator," NAPCON, [Online]. Available: https://www.napconsuite.com/product/napcon-simulator/. [Accessed 19 February 2020].

[2]   H. Vogelsang, "An introduction to energy consumption in pumps," *World Pumps,* vol. 2008, no. 496, pp. 28-31, 2008.

[3]   R. Banerjee, Y. Cong, D. Gielen, G. Jannuzzi, F. Maréchal, A. T. McKane, M. A. Rosen, D. van Es, E. Worrell, R. Ayres, M. Olshanskaya, L. Price, D. Saygin and A. Srivastava, "Global Energy Assessment - Toward a Sustainable Future, Chapter 8: Energy End-Use - Industry," Cambridge University Press, Cambridge, 2012.

[4]   ICF Consulting Limited, "Study on energy efficiency and energy saving potential in industry and on possible policy mechanisms," ICF Consulting Limited, London, 2015.

[5]   NAPCON, *Master's thesis proposal,* Porvoo, 2019.

[6]   J. Harju, N. Turunen, T. Saarinen and F. Pettersson, Interviewees, *Thesis kick-off meeting.* [Interview]. 2 September 2019.

[7]   K. Liljemark, R. Kemi and M. Asujamaa, Interviewees, *Observations of the simulator trainers.* [Interview]. 12 September 2019.

[8]   E. Tamminen, Interviewee, *Contents of the thesis.* [Interview]. 12 September 2019.

[9]   R. Chhabra and V. Shankar, Coulson and Richardson's Chemical Engineering, 7th ed., Vols. 1A: Fluid Flow, Fundamentals and Applications, Oxford: Elsevier Butterworth-Heinemann, 2017.

[10] C. Pfleiderer, Die Kreiselpumpen für Flüssigkeiten und Gase, Berlin: Springer-Verlag, 1961.

[11] I. J. Karassik, W. C. Krutzsch, W. H. Fraser and J. P. Messina, Pump Handbook, New York: McGraw Hill, 1986.

[12] J. M. Kay, J. E. Kay and R. M. Nedderman, An Introduction to Fluid Mechanics and Heat Transfer: With Applications in Chemical and Mechanical Process Engineering, London: Cambridge University Press, 1974.

[13] R. K. Sinnott, Coulson & Richardson's Chemical Engineering, 4th ed., vol. 6: Chemical Engineering Design, Oxford: Elsevier Butterworth-Heinemann, 2005.

[14] D. W. Green and M. Z. Southard, Perry's chemical engineers' handbook, 9th ed., New York: McGraw-Hill Education, 2019.

[15] T. Westerlund, Anläggnings- och systemteknik, Åbo: Tekniska fakulteten vid Åbo Akademi, 2009.

[16] F. Pettersson, H. Skrifvars, K. Lundqvist, K. Fagervik and T. Westerlund, "Ett övningsarbete i pumpdimensionering," Åbo Akademi, Kemisk-tekniska fakulteten, Institutionen för anläggningsteknik, Åbo, 1990.

[17] C. E. Brennen, Hydrodynamics of Pumps, Norwich: Concepts ETI, 1994.

[18] W. E. Forsthoffer, Fortshoffer's Rotating Equipment Handbooks, vol. 3: Compressors, Elsevier Science, 2005.

[19] K. H. Lüdtke, Process Centrifugal Compressors, New York: Springer-Verlag Berlin Heidelberg GmbH, 2004.

[20] T. Mäkelä, Kiertokaasukompressorin monitorointi simulointimallilla, Lappeenranta: Lappeenranta Univeristy of Technology, 2018.

[21] O. S. Ochiche and B. T. Lebele-Alawa, "Improving Compressor Performance to Reduce Loss Production Opportunities in Oil and Gas Production," *Journal of Mechanical Engineering and Automation,* vol. 4, no. 3, pp. 101-109, 2014.

[22] A. Ravi, L. Sznajder and I. Bennett, "Compressor map prediction tool," *IOP Conference Series: Materials Science and Engineering,* vol. 90, 2015.

[23] G. Stephenson, "Integrate Compressor Performance Maps into Process Simulation," *Chemical Engineering Progress,* vol. 107, no. 6, pp. 42-47, 2011.

[24] H. E. Sheets, "Nondimensional Compressor Performance for a Range of Mach Numbers and Molecular Weights," *Transactions of the ASME,* vol. 74, no. 1, pp. 93-102, January 1952.

[25] E. Liese and S. E. Zitney, "The Impeller Exit Flow Coefficient as a Performance Map Variable for Predicting Centrifugal Compressor Off-Design Operation Applied to a Supercritical CO2 Working Fluid," in *ASME Turbo Expo 2017: Turbomachinery Technical Conference and Exposition*, Charlotte, 2017.

[26] ESD Simulation Training Ltd, *Control & Operation of Centrifugal Gas Compressors,* Aberdeenshire: ESD Simulation Training Ltd, 2003.

[27] L. A. Ostromuhov, "Uniform Conversions of Operating Points and Characteristics of Compressor," 2011.

[28] T. Barletta and S. W. Golden, "Centrifugal Compressor Operations," *Petroleum Technology Quarterly,* vol. 9, no. 4, pp. 113-119, 2004.

[29] T. Westerlund, Processindustriell Energiteknik, Turku: Institutionen för Kemiteknik vid Åbo Akademi, 2006.

[30] Y. Patel, Computational modelling of non-equilibrium condensing steam flows in low-pressure steam turbines, Lappeenranta: Lappeenranta University of Technology, 2016.

[31] R. Kurz and K. Brun, "Gas Turbine Performance - What Makes the Map?," in *Proceedings of the 29th Turbomachinery Symposium*, 2000.

[32] L. Hammarström, Interviewee, *Private communication regarding modeling in ProsDS*. [Interview]. 2019 - 2020.

[33] T. Saarinen and N. Turunen, Interviewees, *Private communication with the instructors*. [Interview]. 2019 - 2020.

[34] Johnson Controls, Engineering Data Book, vol. Vb1: Valves, Johnson Controls Inc., 1994.

[35] K. Abdulla and S. M. Walke, "Simulation of Pumps by Aspen Plus," *International Journal of Engineering Science and Innovative Technology,* vol. 4, no. 3, pp. 50-57, 2015.

[36] A. Hamid and M. Kamaruddin, HYSYS®: An Introduction to Chemical Engineering Simulation for UTM Degree++ Program, Universiti Teknologi Malaysia, 2007.

[37] Honeywell, UniSim® Design User Guide, Honeywell, 2009.

[38] Schneider Electric, "Invensys Process System enhances Dynsim simulation software," Schneider Electric, 17 September 2008. [Online]. Available: https://www.automation.com/en-us/products/product17/invensys-process-system-enhances-dynsim-simulation. [Accessed 11 May 2020].

[39] Invensys Process Systems, *DYNSIM OTS Training Course, DYNSIM Modelling: Flow Devices,* Invensys Process Systems, 2008.

[40] Fortum, VTT Technical Research Centre of Finland Ltd., "Apros - Dynamic Process Simulation Software for Nuclear and Thermal Power Plant Applications," Fortum, VTT Technical Research Centre of Finland Ltd., [Online]. Available: http://www.apros.fi/en/. [Accessed 11 May 2020].

[41] Fortum, VTT Technical Research Centre of Finland Ltd., Apros Process component reference guide, Fortum, VTT Technical Research Centre of Finland Ltd., 2015.

[42] M. Casey and C. Robinson, "A Method to Estimate the Performance Map of a Centrifugal Compressor Stage," *Journal of turbomachinery,* vol. 135, no. 2, p. 021034, 2013.

[43] W. Albusaidi and P. Pilidis, "An Iterative Method to Derive the Equivalent Centrifugal Compressor Performance at Various Operating Conditions: Part I: Modelling of Suction Parameters Impact," *Energies,* vol. 8, no. 8, pp. 8497-8515, 2015.

[44] I. Macdougal and R. L. Elder, "Simulation of centrifugal compressor transient performance for process plant applications," *Journal of engineering for power,* vol. 105, no. 4, pp. 885-890, 1983.

[45] S. Modekurti, J. Eslick, B. Omell, D. Bhattacharyya, D. C. Miller and S. E. Zitne, "Design, dynamic modeling, and control of multistage CO2 compression system," *International Journal of Greenhouse Gas Control,* vol. 62, pp. 31-45, 2017.

Appendix A – Deduction of equation for the discharge pressure from the polytropic head

Polytropic head for a centrifugal compressor as given by Equation 29:

$$H_p = Z_{avg} T_1 \frac{R}{MW} \frac{n}{n-1} \left(\left(\frac{p_3}{p_1} \right)^{(n-1)/n} - 1 \right)$$

Division by the factors in front of the parenthesis:

$$\frac{H_p}{Z_{avg} T_1 \frac{R}{MW} \frac{n}{n-1}} = \left(\frac{p_3}{p_1} \right)^{(n-1)/n} - 1$$

Moving 1 to left hand side and switching sides:

$$\left(\frac{p_3}{p_1} \right)^{(n-1)/n} = \frac{H_p}{Z_{avg} T_1 \frac{R}{MW} \frac{n}{n-1}} + 1$$

Taking the root of the exponent:

$$\frac{p_3}{p_1} = \sqrt[(n-1)/n]{\frac{H_p}{Z_{avg} T_1 \frac{R}{MW} \frac{n}{n-1}} + 1}$$

Multiplying both sides by inlet pressure finally gives:

$$p_3 = p_1 \times \sqrt[(n-1)/n]{\frac{H_p}{Z_{avg} T_1 \frac{R}{MW} \frac{n}{n-1}} + 1}$$

Appendix B – Deduction of equation for the polytropic exponent

Two equations are given for the polytropic co-efficient γ, which can be combined to relate n to κ. [26, p. A28]

$$\gamma = \frac{n-1}{n}$$

$$\gamma = \frac{\kappa - 1}{\kappa \eta_p}$$

Combining these:

$$\frac{n-1}{n} = \frac{\kappa - 1}{\kappa \eta_p}$$

Multiplication by n:

$$n - 1 = n\left(\frac{\kappa - 1}{\kappa \eta_p}\right)$$

Moving to same side:

$$n - 1 - n\left(\frac{\kappa - 1}{\kappa \eta_p}\right) = 0$$

Moving -1 to right hand side and factorizing left hand side for n:

$$n\left(1 - \frac{\kappa - 1}{\kappa \eta_p}\right) = 1$$

Division by the parenthesis finally yields:

$$n = \frac{1}{1 - \frac{\kappa - 1}{\kappa \eta_p}}$$

Appendix C – Deduction of equation for the static volumetric flow rate at impeller exit

The exit flow coefficient is defined by Equation 43 as:

$$\varphi_3 = \frac{\dot{V}_3}{\pi d b_2 U}$$

Multiplying by the denominator gives:

$$\varphi_3 \pi d b_2 U = \dot{V}_3$$

And switching sides finally yields:

$$\dot{V}_3 = \varphi_3 \pi d b_2 U$$

Appendix D – Deduction of equation for the inlet volume flow

A general equation for calculating the ratio of static volumetric flow rate at impeller exit to total volumetric flow rate at inlet is given by Equation 48:

$$\frac{\dot{V}_3}{\dot{V}_1} = \frac{T_3}{T_1}\frac{p_1}{p_3}\frac{Z_3}{Z_1}$$

Inverting the fractions:

$$\frac{\dot{V}_1}{\dot{V}_3} = \frac{T_1}{T_3}\frac{p_3}{p_1}\frac{Z_1}{Z_3}$$

Lastly, multiplying by the static volume flow:

$$\dot{V}_1 = \dot{V}_3 \frac{T_1}{T_3}\frac{p_3}{p_1}\frac{Z_1}{Z_3}$$

Appendix E – Deduction of equation for the compressibility and the ratio of specific heats

The compressibility can be solved from the relation below. [26, p. A18]

$$pV_m = ZRT$$

Rearranging:

$$Z = \frac{pV_m}{RT}$$

For κ and C_p, the two equations below are given. [26, p. A19]

$$\kappa = \frac{C_p}{C_V}$$

$$C_p = C_V + R$$

Rearranging:

$$C_V = C_p - R$$

Combining:

$$\kappa = \frac{C_p}{C_p - R}$$

Appendix F – Deduction of equation for direct conversion of the polytropic head

The expressions for conversion of polytropic head to dimensionless head coefficient and for the conversion of the head coefficient to polytropic head as given by Equations 39 and 41:

$$\psi = \frac{2H_p}{U^2}$$

$$H_{p,new} = \psi \frac{U_{new}^2}{2}$$

Inserting the equation for the head coefficient into the equation of polytropic head:

$$H_{p,new} = \frac{2H_p}{U^2} \frac{U_{new}^2}{2}$$

The expression for *U*, as given by Equation 38:

$$U = \pi d\omega$$

Inserting *U* into the polytropic head equation:

$$H_{p,new} = \frac{2H_p}{(\pi d\omega\,)^2} \frac{(\pi d\omega_{new}\,)^2}{2}$$

Trimming the equation:

$$H_{p,new} = H_p \frac{(\pi d\omega_{new})^2}{(\pi d\omega\,)^2}$$

Moving the numerator and denominator into the same parenthesis:

$$H_{p,new} = H_p \left(\frac{\pi d\omega_{new}}{\pi d\omega}\right)^2$$

And after one final trimming of constants:

$$H_{p,new} = H_p \left(\frac{\omega_{new}}{\omega}\right)^2$$

Note, that this is essentially one of the fan laws.

Appendix G – Deduction of equation for direct conversion of the inlet volume flow

Expression for exit flow coefficient as given by Equation 43:

$$\varphi_3 = \frac{\dot{V}_3}{\pi d b_2 U}$$

An equation for the static volumetric flow at impeller exit is given below. [45, p. 38]

$$\dot{V}_3 = \dot{V}_1 \frac{Z_3 T_3 p_1}{p_3 Z_1 T_1}$$

Temperature ratio can be calculated according to the expression below. [25, p. 4]

$$\frac{T_3}{T_1} = \left(\frac{p_3}{p_1}\right)^m$$

The outlet pressure from Appendix A:

$$p_3 = p_1 \times \sqrt[\left(\frac{n-1}{n}\right)]{\frac{H_p}{\frac{R}{MW} Z_{avg} T_1 \left(\frac{n}{n-1}\right)} + 1}$$

From Appendix B:

$$\frac{n-1}{n} = \frac{k-1}{k\eta_p}$$

and thus

$$\frac{n}{n-1} = \frac{k\eta_p}{k-1}$$

Substituting the terms containing *n* in the equation for outlet pressure:

$$p_3 = p_1 \times \sqrt[\left(\frac{k-1}{k\eta_p}\right)]{\frac{H_p}{\frac{R}{MW} Z_{avg} T_1 \left(\frac{k\eta_p}{k-1}\right)} + 1}$$

Inserting expression for outlet pressure in that for temperature ratio:

$$\frac{T_3}{T_1} = \left(\frac{p_1 \times \sqrt[\left(\frac{k-1}{k\eta_p}\right)]{\dfrac{H_p}{\dfrac{R}{MW} Z_{avg} T_1 \left(\dfrac{k\eta_p}{k-1}\right)} + 1}}{p_1} \right)^m$$

Trimming:

$$\frac{T_3}{T_1} = \left(\sqrt[\left(\frac{k-1}{k\eta_p}\right)]{\dfrac{H_p}{\dfrac{R}{MW} Z_{avg} T_1 \left(\dfrac{k\eta_p}{k-1}\right)} + 1} \right)^m$$

Substituting the temperature ratio in the static volume flow equation:

$$\dot{V}_3 = \dot{V}_1 \frac{Z_3 p_1}{p_3 Z_1} \left(\sqrt[\left(\frac{k-1}{k\eta_p}\right)]{\dfrac{H_p}{\dfrac{R}{MW} Z_{avg} T_1 \left(\dfrac{k\eta_p}{k-1}\right)} + 1} \right)^m$$

Substituting the remaining outlet pressure:

$$\dot{V}_3 = \dot{V}_1 \frac{3 p_3}{Z_1 p_1 \times \sqrt[\left(\frac{k-1}{k\eta_p}\right)]{\dfrac{H_p}{\dfrac{R}{MW} Z_{avg} T_1 \left(\dfrac{k\eta_p}{k-1}\right)} + 1}} \left(\sqrt[\left(\frac{k-1}{k\eta_p}\right)]{\dfrac{H_p}{\dfrac{R}{MW} Z_{avg} T_1 \left(\dfrac{k\eta_p}{k-1}\right)} + 1} \right)^m$$

Trimming the inlet pressure:

$$\dot{V}_3 = \dot{V}_1 \frac{Z_3}{Z_1} \frac{\left(\sqrt[\left(\frac{k-1}{k\eta_p}\right)]{\dfrac{H_p}{\dfrac{R}{MW} Z_{avg} T_1 \left(\dfrac{k\eta_p}{k-1}\right)} + 1} \right)^m}{\sqrt[\left(\frac{k-1}{k\eta_p}\right)]{\dfrac{H_p}{\dfrac{R}{MW} Z_{avg} T_1 \left(\dfrac{k\eta_p}{k-1}\right)} + 1}}$$

Merging the numerator and denominator:

$$\dot{V}_3 = \dot{V}_1 \frac{Z_3}{Z_1} \left(\sqrt[\left(\frac{k-1}{k\eta_p}\right)]{\frac{H_p}{\frac{R}{MW} Z_{avg} T_1 \left(\frac{k\eta_p}{k-1}\right)} + 1} \right)^{m-1}$$

Moving the root to the exponent:

$$\dot{V}_3 = \dot{V}_1 \frac{Z_3}{Z_1} \left(\frac{H_p}{\frac{R}{MW} Z_{avg} T_1 \left(\frac{k\eta_p}{k-1}\right)} + 1 \right)^{\frac{k\eta_p(m-1)}{k-1}}$$

Inserting the static outlet volume to the exit flow coefficient:

$$\varphi_3 = \frac{\dot{V}_1 \frac{Z_3}{Z_1} \left(\frac{H_p}{\frac{R}{MW} Z_{avg} T_1 \left(\frac{k\eta_p}{k-1}\right)} + 1 \right)^{\frac{k\eta_p(m-1)}{k-1}}}{\pi d b_2 u_2}$$

Inserting the expression for *U* from Appendix F:

$$\varphi_3 = \frac{\dot{V}_1 \frac{Z_3}{Z_1} \left(\frac{H_p}{\frac{R}{MW} Z_{avg} T_1 \left(\frac{k\eta_p}{k-1}\right)} + 1 \right)^{\frac{k\eta_p(m-1)}{k-1}}}{\pi d b_2 \pi d N}$$

Trimming:

$$\varphi_3 = \frac{\dot{V}_1 \frac{Z_3}{Z_1}}{\pi^2 d^2 b_2 N} \left(\frac{H_p}{\frac{R}{MW} Z_{avg} T_1 \left(\frac{k\eta_p}{k-1}\right)} + 1 \right)^{\frac{k\eta_p(m-1)}{k-1}}$$

Then the equations for converting back to volume flow remain. From Appendix D, the equation for the new inlet volume:

$$\dot{V}_{1,new} = \dot{V}_{3,new} \frac{T_{1,new}}{T_{3,new}} \frac{P_{3,new}}{P_{1,new}} \frac{Z_{1,new}}{Z_{3,new}}$$

Inserting the expression for $\dot{V}_3$ from Appendix C:

$$\dot{V}_{1,new} = \varphi_3 \pi d b_2 U_{new} \frac{T_{1,new}}{T_{3,new}} \frac{P_{3,new}}{P_{1,new}} \frac{Z_{1,new}}{Z_{3,new}}$$

From the previously presented equation for the temperature ratio follows that

$$\frac{T_{1,new}}{T_{3,new}} = \frac{1}{\left(\dfrac{p_{3,new}}{p_{1,new}}\right)^{m_{new}}}$$

Inserting this into the equation for $\dot{V}_{1,new}$:

$$\dot{V}_{in,new} = \varphi_3 \pi d b_2 U_{new} \frac{1}{\left(\dfrac{p_{3,new}}{p_{1,new}}\right)^{m_{new}}} \frac{p_{3,new}}{p_{1,new}} \frac{Z_{1,new}}{Z_{3,new}}$$

The pressure ratios can be simplified:

$$\dot{V}_{1,new} = \varphi_3 \pi d b_2 U_{new} \left(\frac{p_{3,new}}{p_{1,new}}\right)^{1-m_{new}} \frac{Z_{1,new}}{Z_{3,new}}$$

Inserting the previous expression for the outlet pressure and simplifying:

$$\dot{V}_{in,new} = \varphi_3 \pi d b_2 U_{new} \left(\left(\frac{k_{new}-1}{k_{new}\eta_{p,new}}\right)\sqrt{\frac{H_{p,new}}{\frac{R}{MW_{new}}Z_{avg,new}T_{1,new}\left(\frac{k_{new}\eta_{p,new}}{k_{new}-1}\right)}+1}\right)^{1-m_{new}} \frac{Z_{1,new}}{Z_{3,new}}$$

Substituting the exit flow coefficient with the previously derived expression yields:

$$\dot{V}_{1,new} = \frac{\dot{V}_1 \frac{Z_3}{Z_1}}{\pi^2 d^2 b_2 N} \left(\frac{H_p}{\frac{R}{MW}Z_{avg}T_1\left(\frac{k\eta_p}{k-1}\right)}+1\right)^{\frac{k\eta_p(m-1)}{k-1}} \pi d b_2 U_{new} \left(\left(\frac{k_{new}-1}{k_{new}\eta_{p,new}}\right)\sqrt{\frac{H_{p,new}}{\frac{R}{MW_{new}}Z_{avg,new}T_{1,new}\left(\frac{k_{new}\eta_{p,new}}{k_{new}-1}\right)}+1}\right)^{1-m_{new}} \frac{Z_{1,new}}{Z_{3,new}}$$

Inserting expression for U_{new} from Appendix F and trimming:

$$\dot{V}_{1,new} = \frac{\dot{V}_1 N_{new} Z_3 Z_{1,new}}{\pi d N Z_1 Z_{3,new}} \left(\frac{H_p}{\frac{R}{MW}Z_{avg}T_1\left(\frac{k\eta_p}{k-1}\right)}+1\right)^{\frac{k\eta_p(m-1)}{k-1}} \left(\frac{H_{p,new}}{\frac{R}{MW_{new}}Z_{avg,new}T_{1,new}\left(\frac{k_{new}\eta_{p,new}}{k_{new}-1}\right)}+1\right)^{\frac{k_{new}\eta_{p,new}(1-m_{new})}{k_{new}-1}}$$

Finally, inserting the expression for the new polytropic head from Appendix F yields:

$$\dot{V}_{in,new} = \frac{\dot{V}_1 N_{new} Z_3 Z_{1,new}}{\pi d N Z_1 Z_{3,new}} \left(\frac{H_p}{\frac{R}{MW}Z_{avg}T_1\left(\frac{k\eta_p}{k-1}\right)}+1\right)^{\frac{k\eta_p(m-1)}{k-1}} \left(\frac{H_p\left(\frac{N_{new}}{N}\right)^2}{\frac{R}{MW_{new}}Z_{avg,new}T_{1,new}\left(\frac{k_{new}\eta_{p,new}}{k_{new}-1}\right)}+1\right)^{\frac{k_{new}\eta_{p,new}(1-m_{new})}{k_{new}-1}}$$

Appendix H – Performance maps of compressors A, B and C
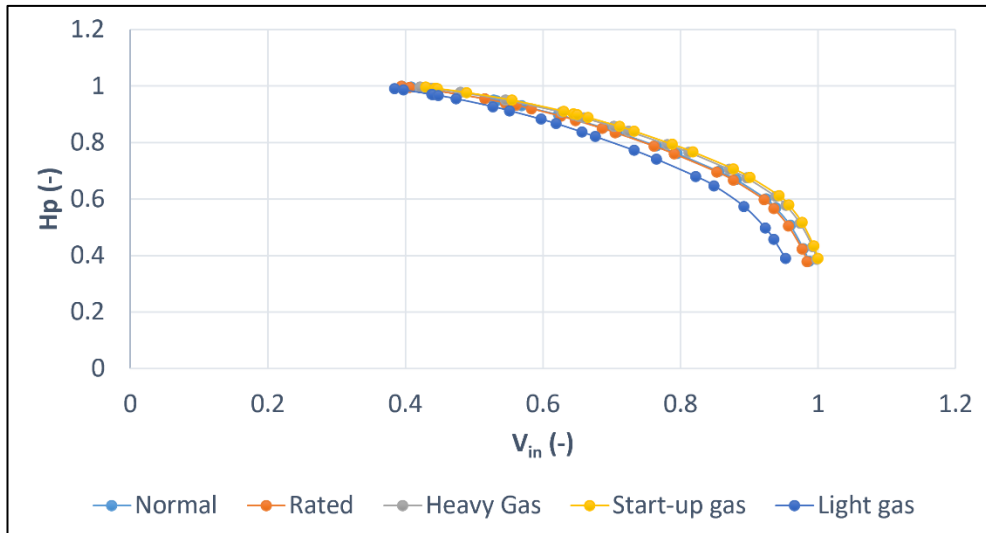
Figure 55.Scaled performance map of compressor A.
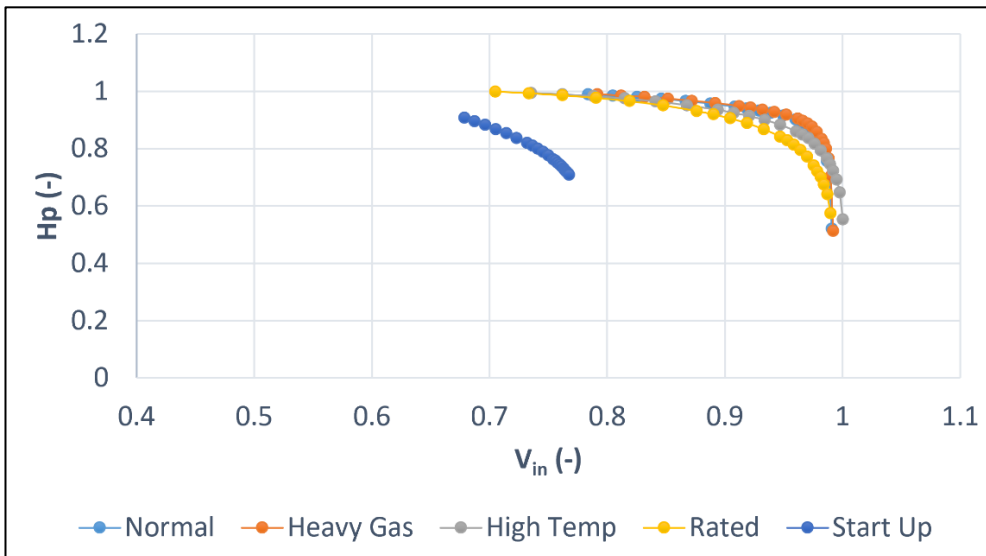
Figure 56. Scaled performance map of compressor B.
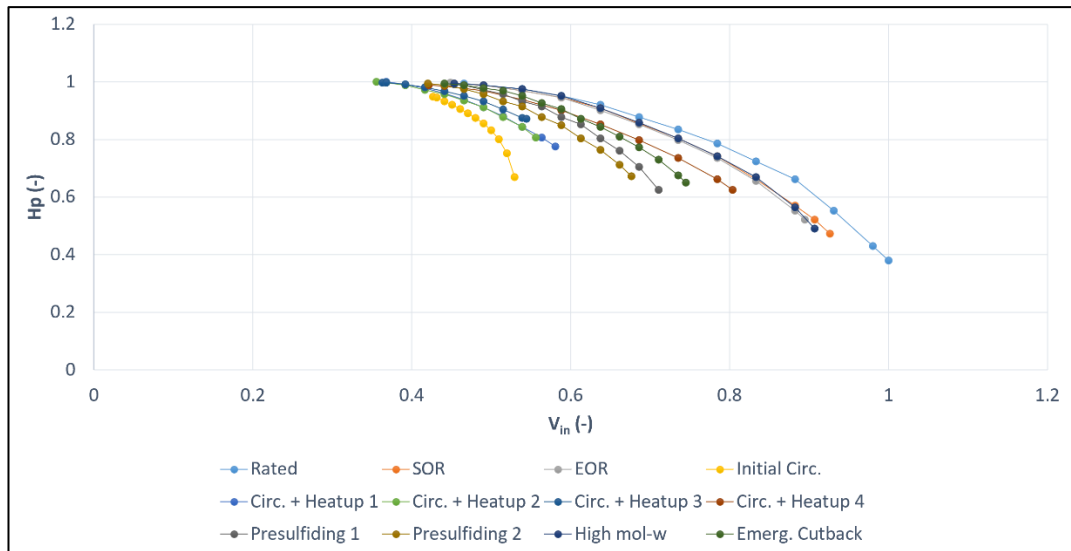
Figure 57. Scaled performance map of compressor C.

Appendix I – Dimensionless inlet flow coefficient performance maps of compressors A and B
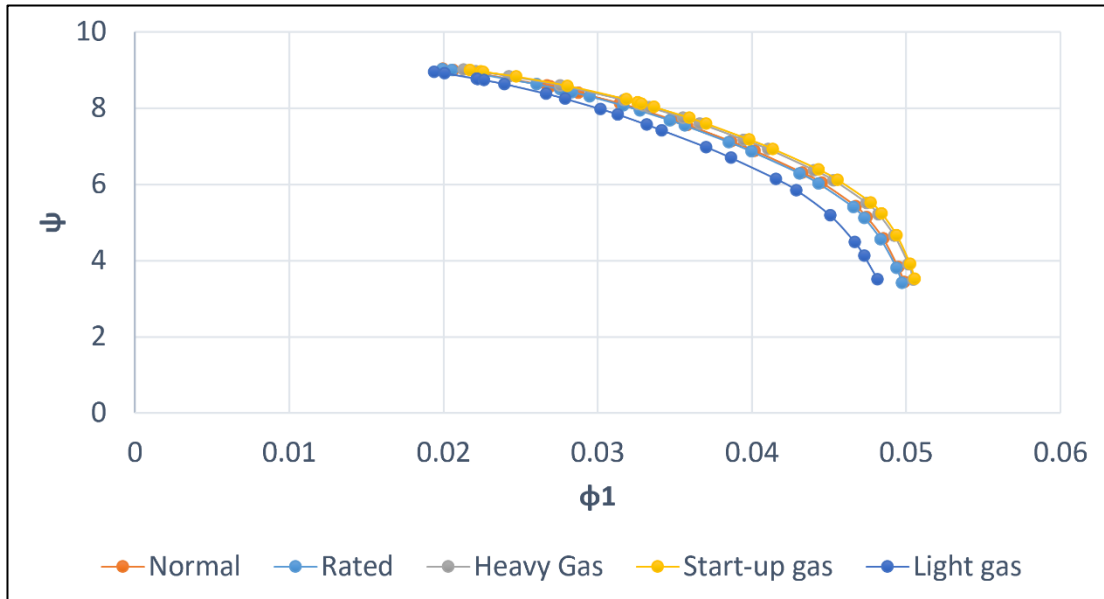
Figure 58. Dimensionless performance map based on the inlet flow coefficient of compressor A.
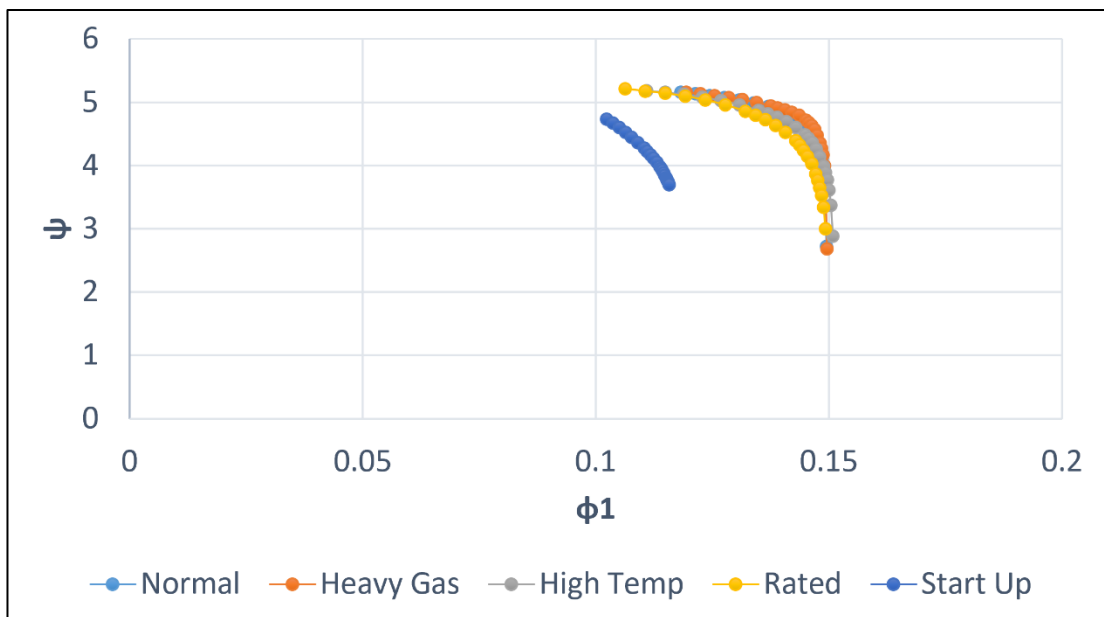
Figure 59. Inlet flow coefficient performance map of compressor B.

Appendix J – Predicted performance curves of compressor A
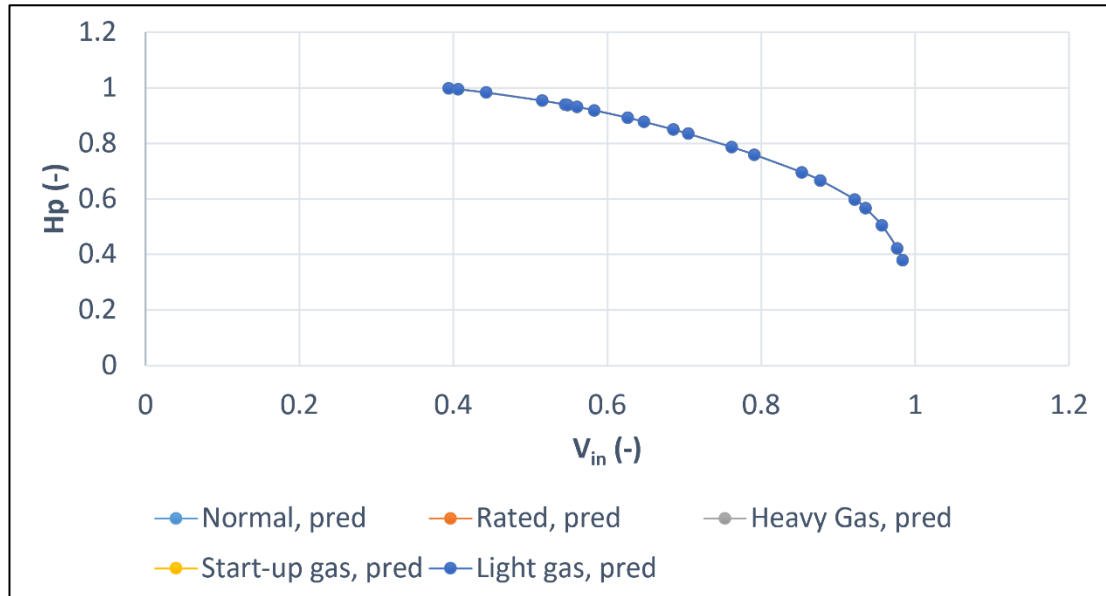
Figure 60. Scaled predicted performance map of compressor A. Predictions are based on the inlet flow coefficient curve of the rated case.
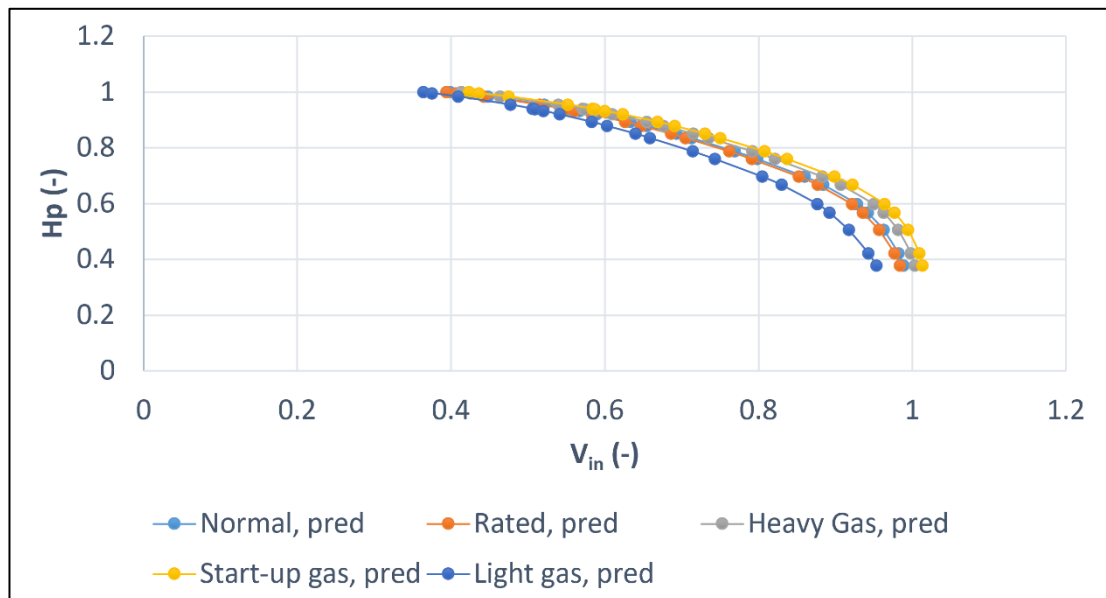
Figure 61. Scaled predicted performance map of compressor A. Predictions are based on the exit flow coefficient curve of the rated case.
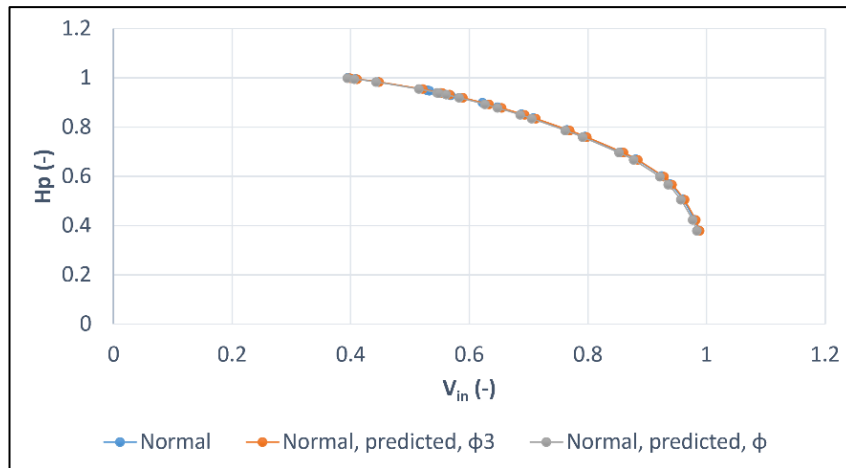
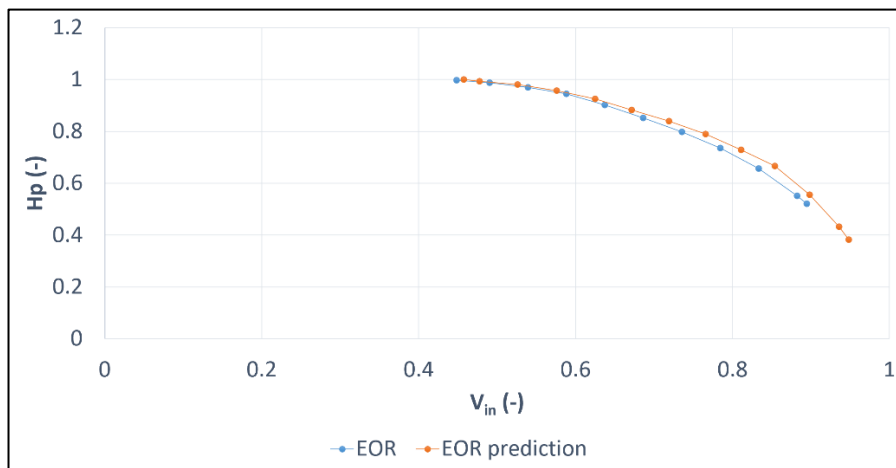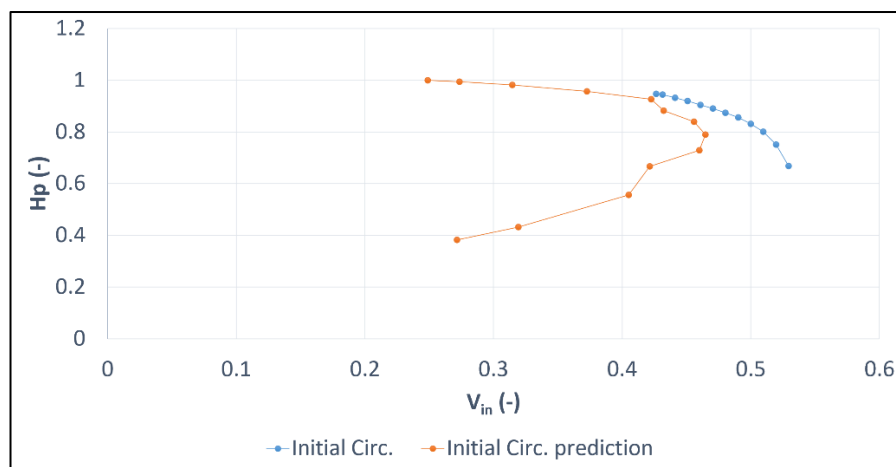Figure 62. A comparison of the scaled manufacturer performance curve and the predictions of the inlet and exit flow coefficient curves for the normal case. The predictions are based on the dimensionless curves of the rated case.
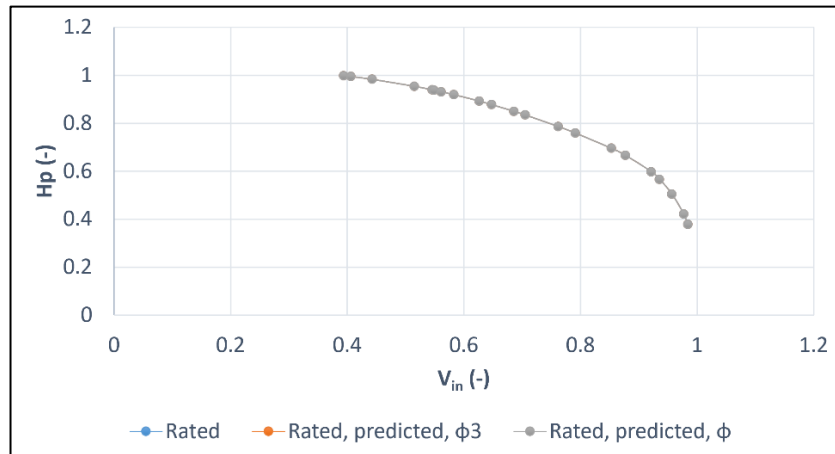
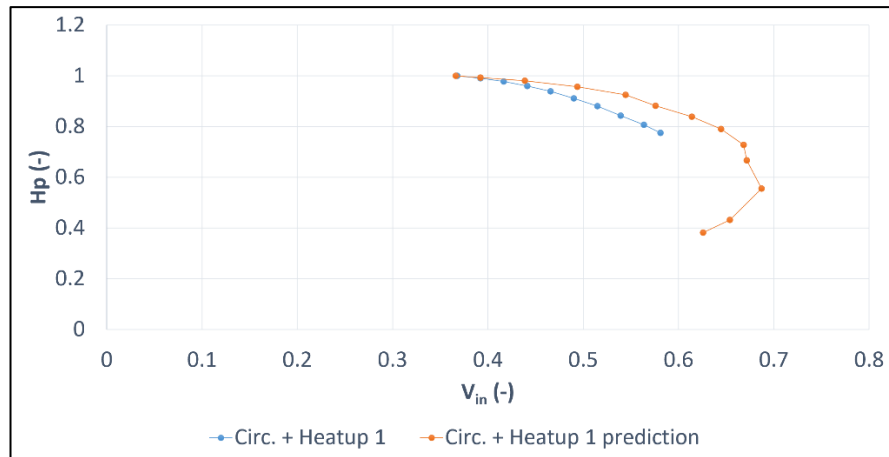
Figure 63. A comparison of the scaled manufacturer performance curve and the predictions of the inlet and exit flow coefficient curves for the rated case.
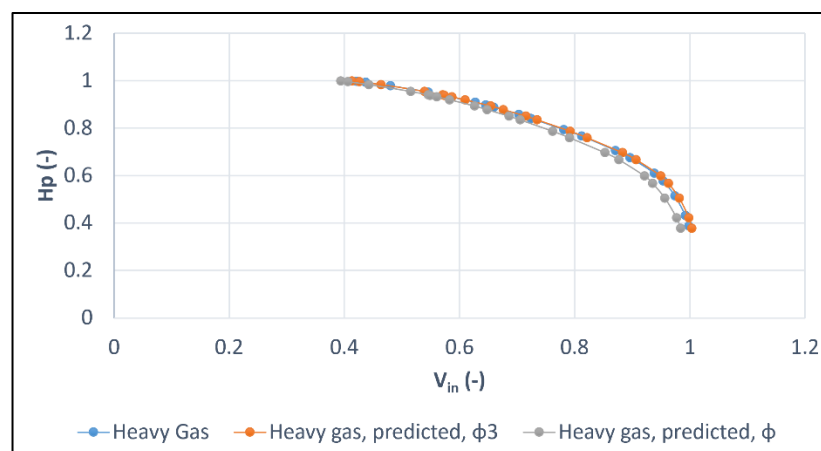
Figure 64. A comparison of the scaled manufacturer performance curve and the predictions of the inlet and exit flow coefficient curves for the heavy gas case.
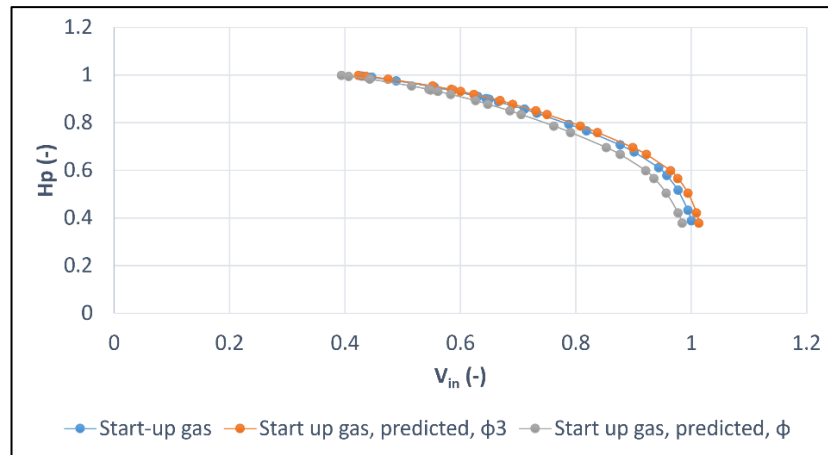
Figure 65. A comparison of the scaled manufacturer performance curve and the predictions of the inlet and exit flow coefficient curves for the startup gas case.
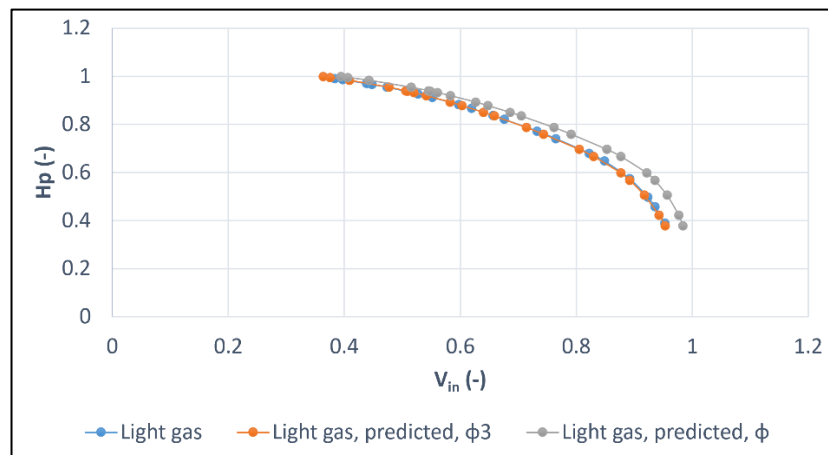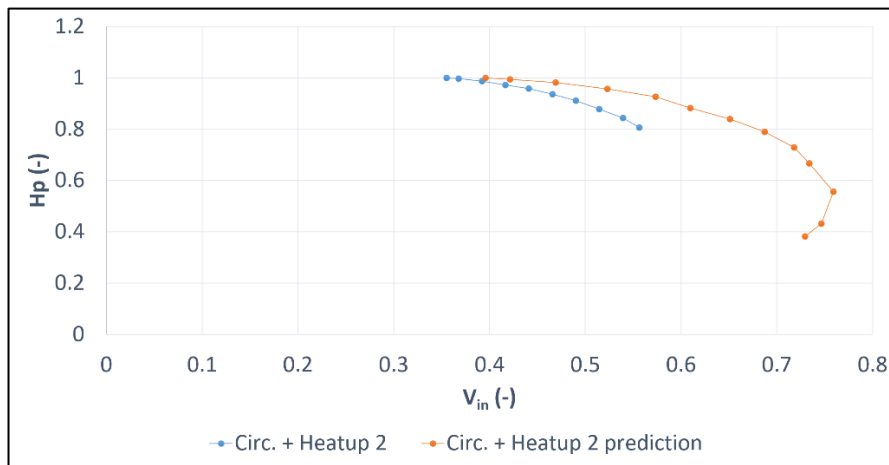

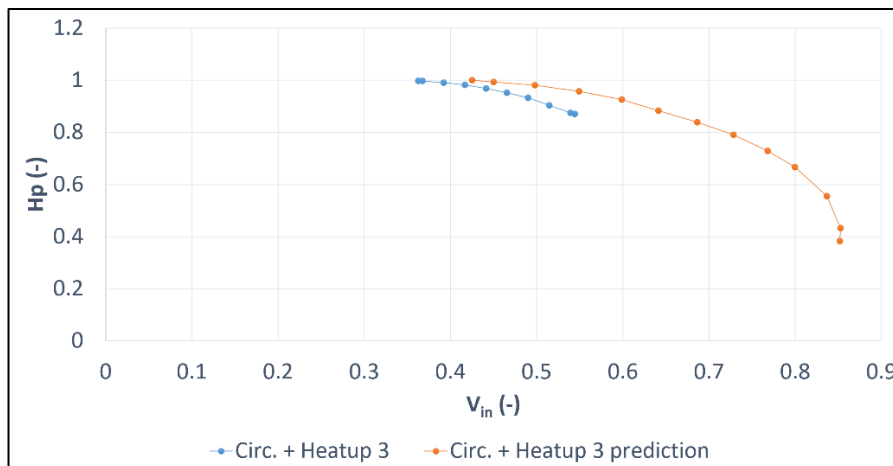Figure 66. A comparison of the scaled manufacturer performance curve and the predictions of the inlet and exit flow coefficient curves for the light gas case.

Appendix K – Predicted performance curves of compressor B
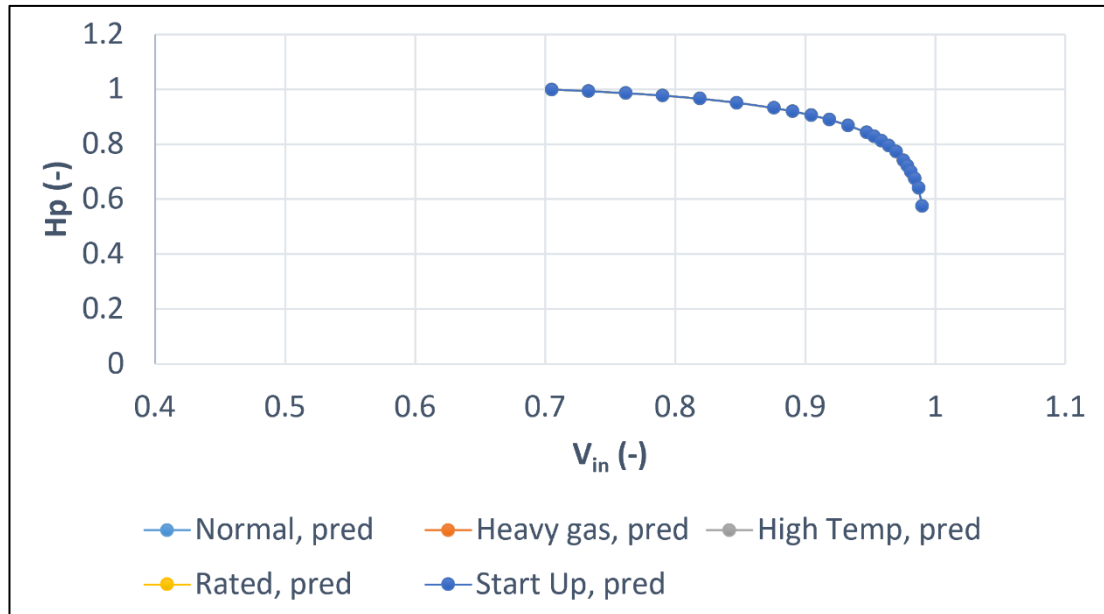
Figure 67. Scaled predicted performance map of compressor B. Predictions are based on the inlet flow coefficient curve of the rated case.
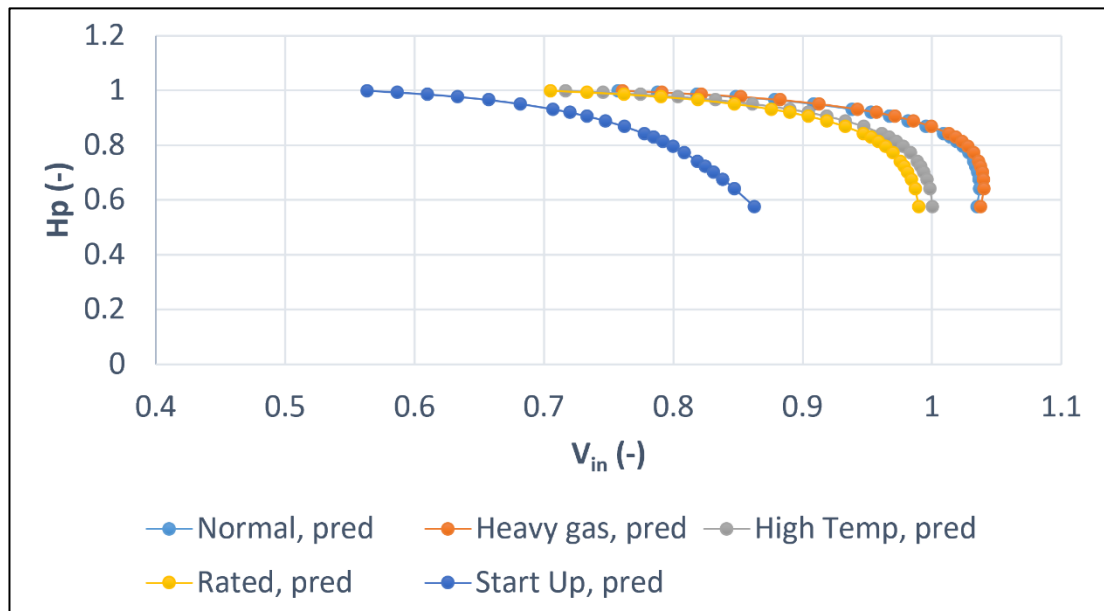
Figure 68. Scaled predicted performance map of compressor B. Predictions are based on the exit flow coefficient curve of the rated case.
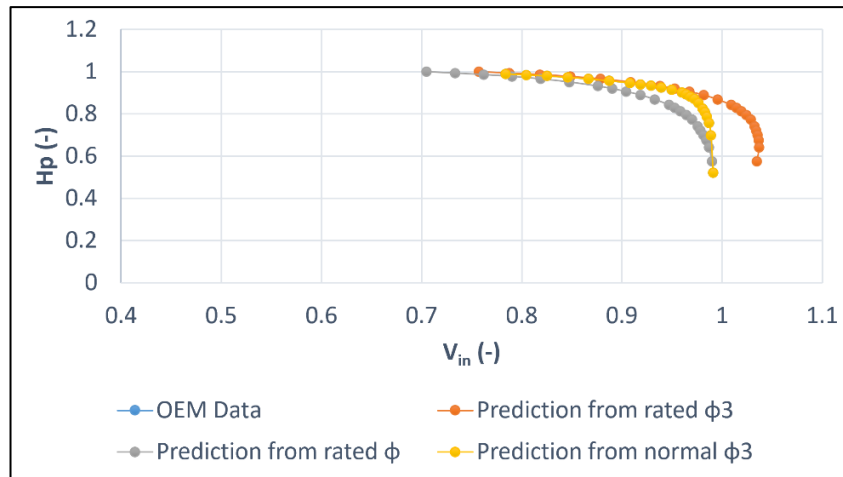
Figure 69. A comparison of the scaled manufacturer performance curve and the predictions of the inlet and exit flow coefficient curves for the normal case.
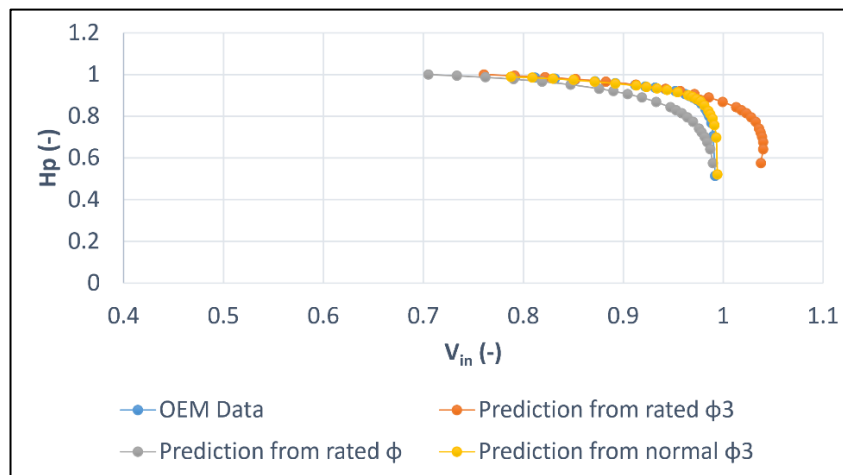
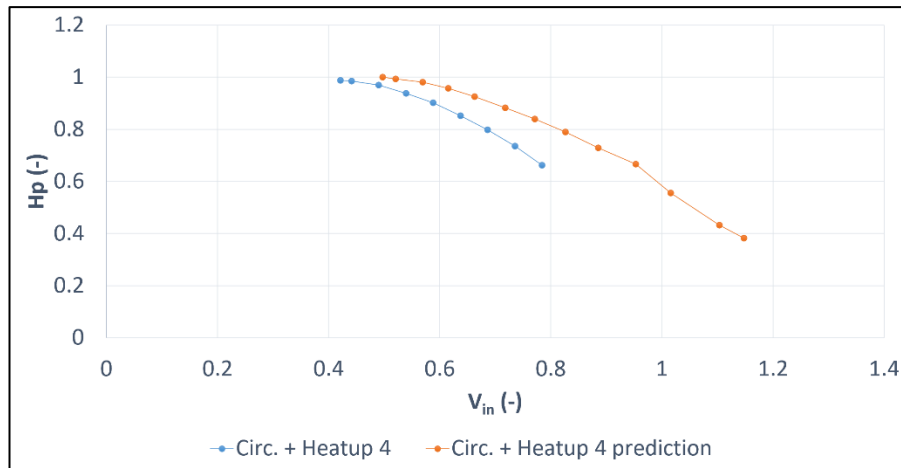Figure 70. A comparison of the scaled manufacturer performance curve and the predictions of the inlet and exit flow coefficient curves for the heavy gas case.
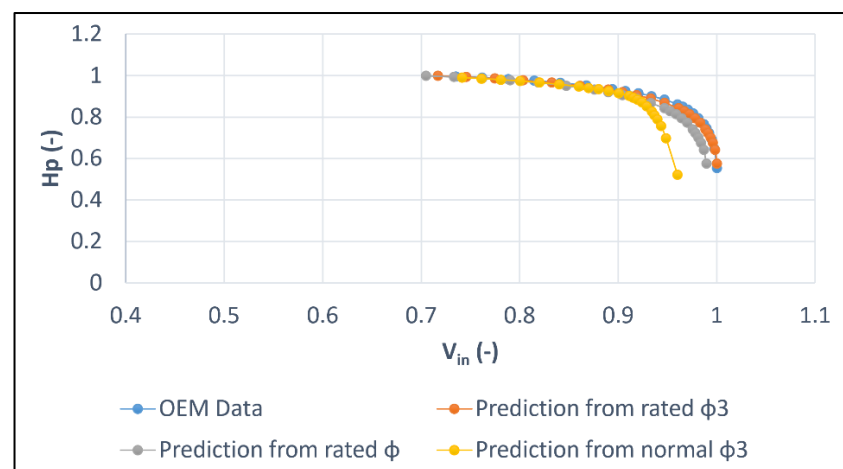
Figure 71. A comparison of the scaled manufacturer performance curve and the predictions of the inlet and exit flow coefficient curves for the high temperature case.
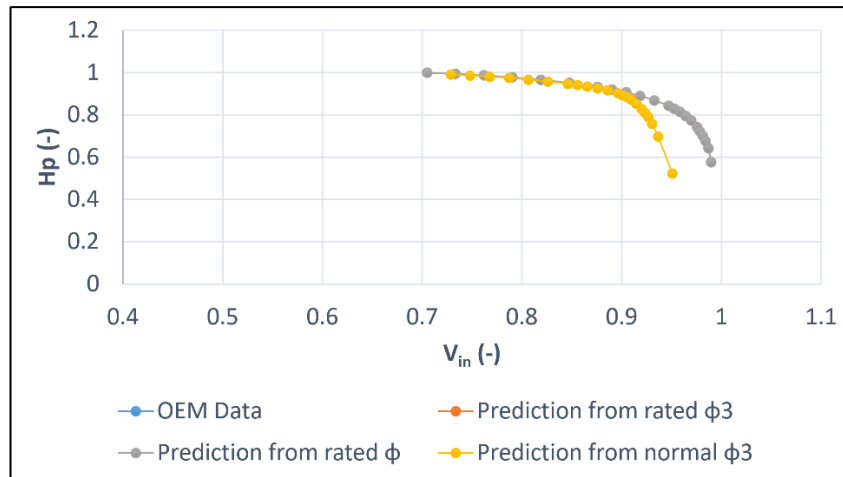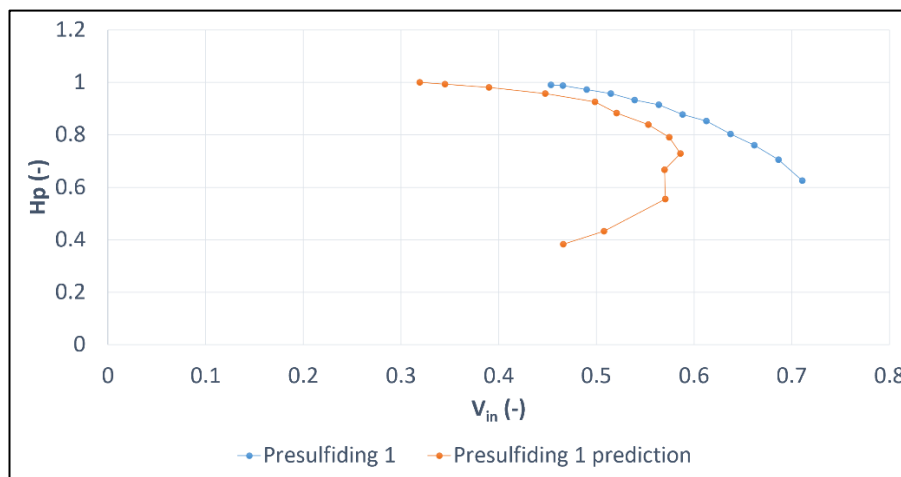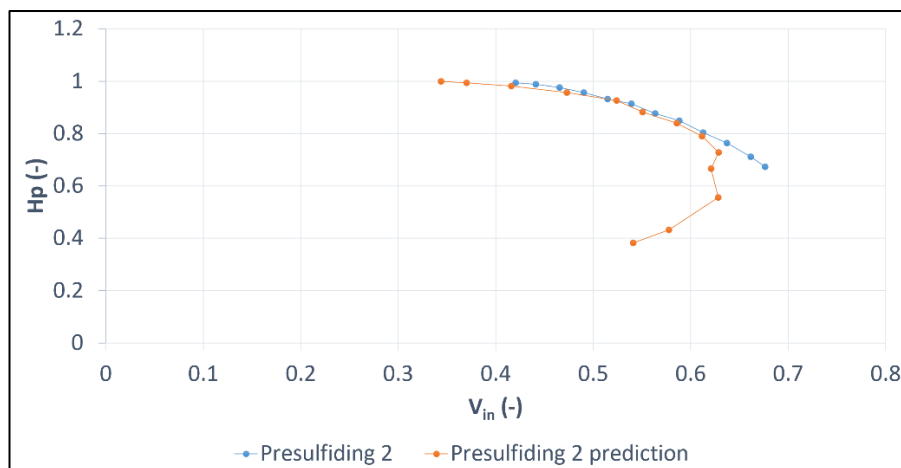
Figure 72. A comparison of the scaled manufacturer performance curve and the predictions of the inlet and exit flow coefficient curves for the rated case.
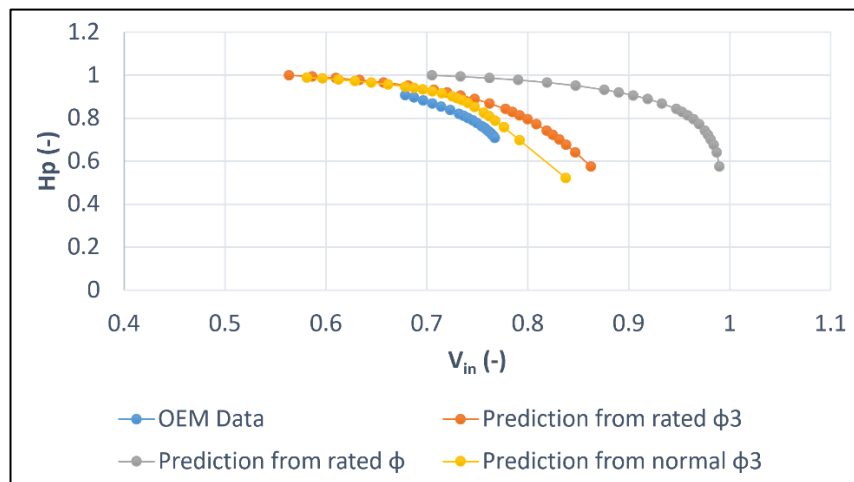
Figure 73. A comparison of the scaled manufacturer performance curve and the predictions of the inlet and exit flow coefficient curves for the startup case.

Appendix L – Predicted performance curves of compressor C
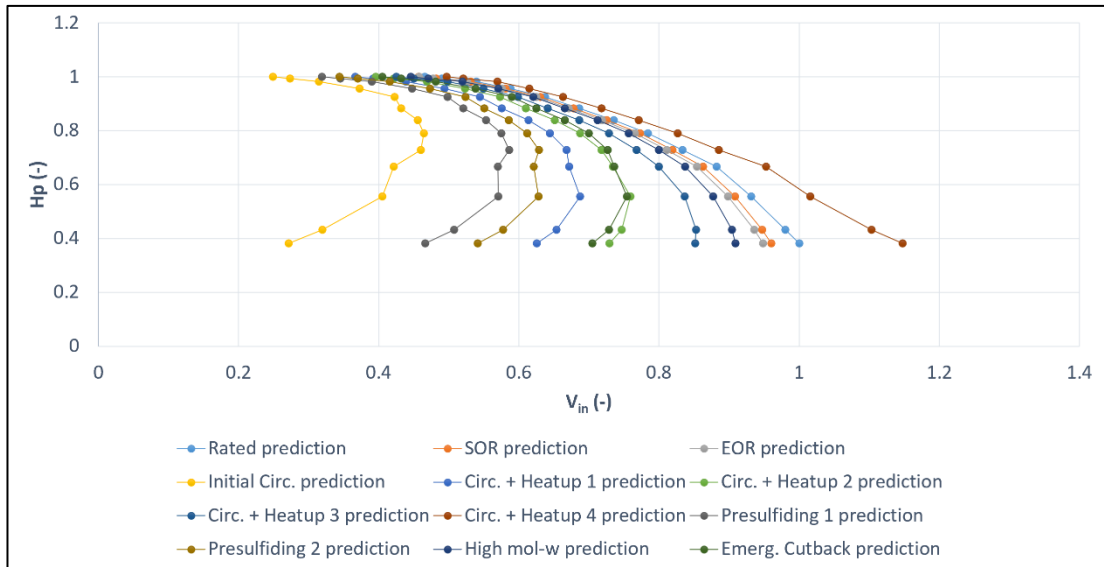
Figure 74. Scaled predicted performance map of compressor C. Predictions are based on the exit flow coefficient curve of the rated case.
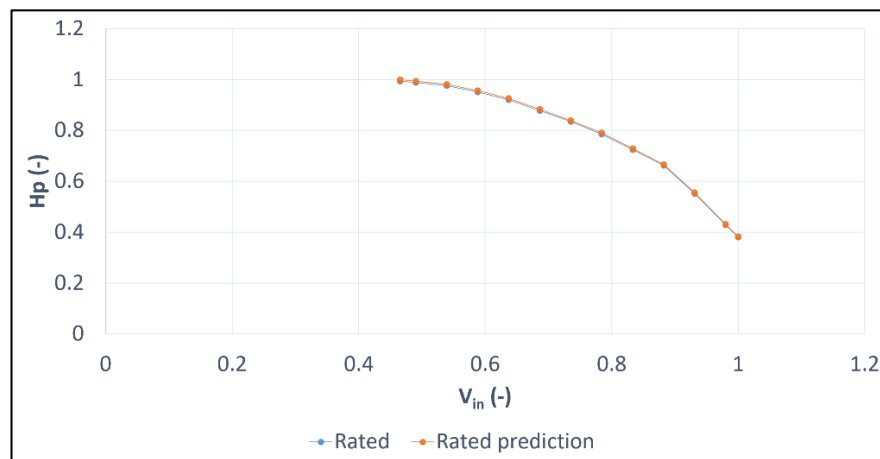
Figure 75. A comparison of the scaled manufacturer performance curve and the prediction of the exit flow coefficient curve for the rated case.
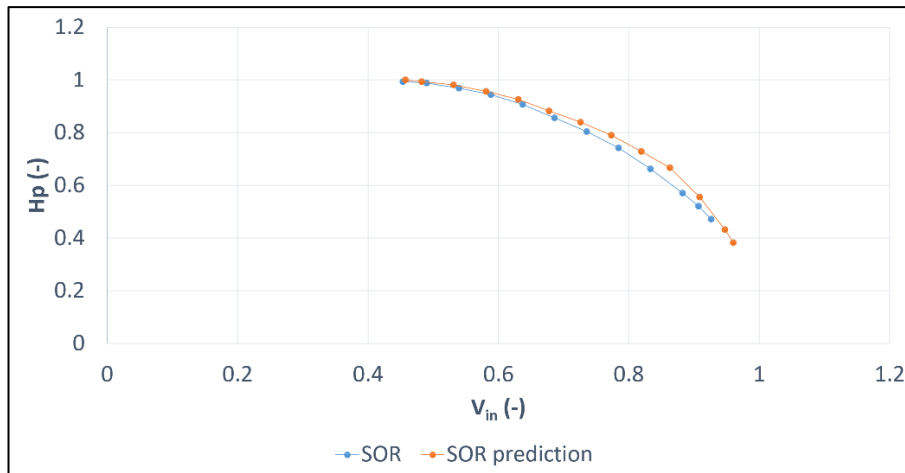
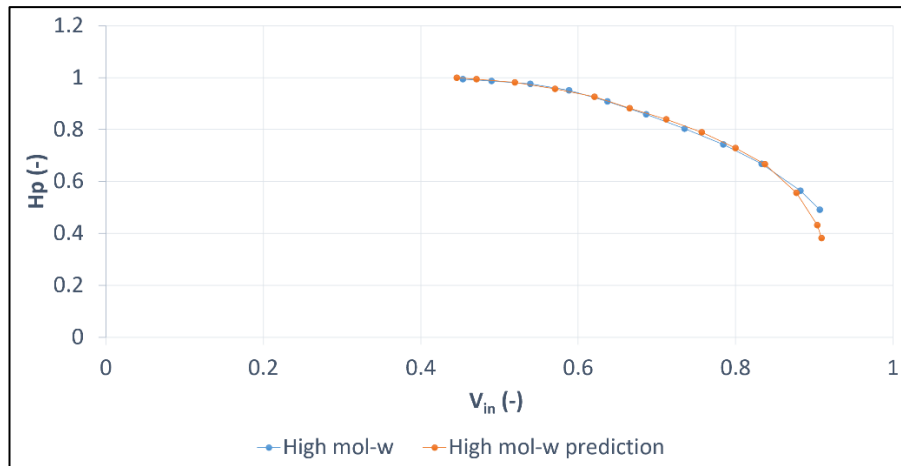Figure 76. A comparison of the scaled manufacturer performance curve and the prediction of the exit flow coefficient curve for the SOR case.
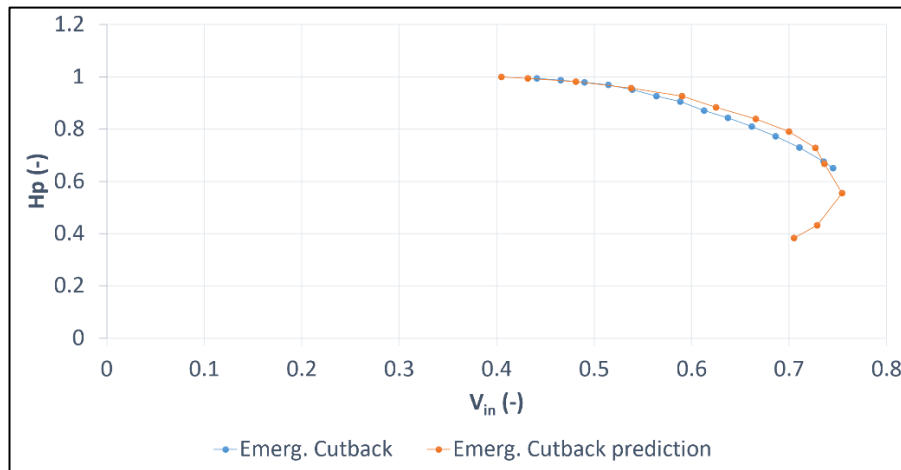

Figure 77. A comparison of the scaled manufacturer performance curve and the prediction of the exit flow coefficient curve for the EOR case.

Figure 78. A comparison of the scaled manufacturer performance curve and the prediction of the exit flow coefficient curve for the initial circulation case.

Figure 79. A comparison of the scaled manufacturer performance curve and the prediction of the exit flow coefficient curve for the circulation and heatup 1 case.

Figure 80. A comparison of the scaled manufacturer performance curve and the prediction of the exit flow coefficient curve for the circulation and heatup 2 case.

Figure 81. A comparison of the scaled manufacturer performance curve and the prediction of the exit flow coefficient curve for the circulation and heatup 3 case.

Figure 82. A comparison of the scaled manufacturer performance curve and the prediction of the exit flow coefficient curve for the circulation and heatup 4 case.

Figure 83. A comparison of the scaled manufacturer performance curve and the prediction of the exit flow coefficient curve for the presulfiding 1 case.

Figure 84. A comparison of the scaled manufacturer performance curve and the prediction of the exit flow coefficient curve for the presulfiding 2 case.

112

Figure 85. A comparison of the scaled manufacturer performance curve and the prediction of the exit flow coefficient curve for the high molar weight case.

Figure 86. A comparison of the scaled manufacturer performance curve and the prediction of the exit flow coefficient curve for the emergency cutback case.

Appendix M – Process data
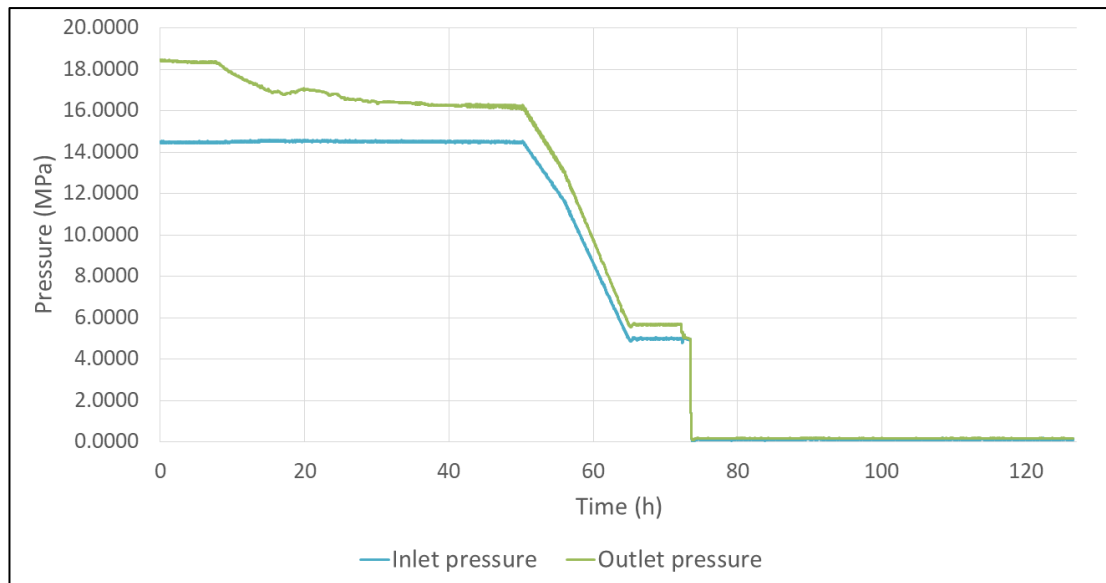
Figure 87. Pressure process data of the shutdown case.
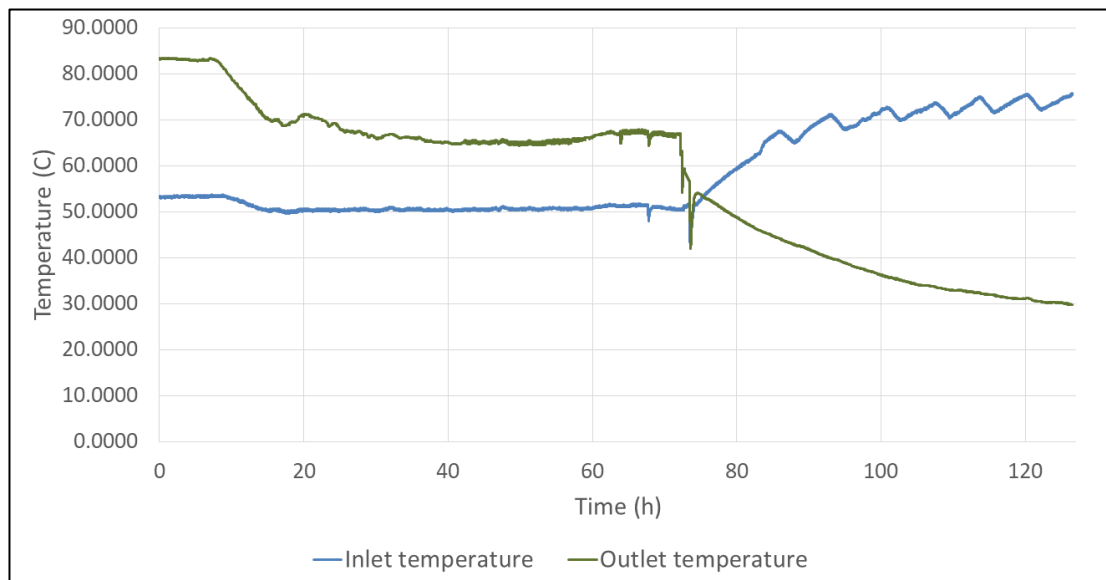
Figure 88. Temperature process data of the shutdown case.
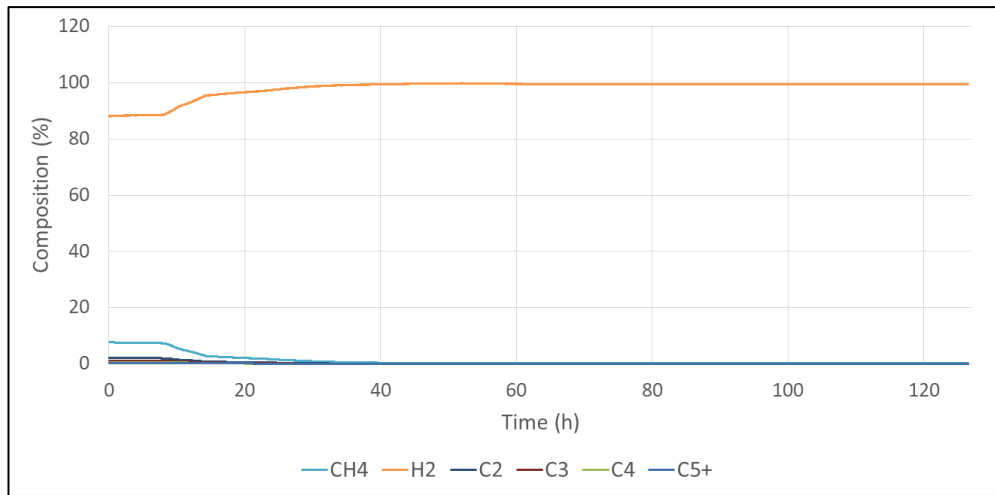
Figure 89. Composition process data of the shutdown case.
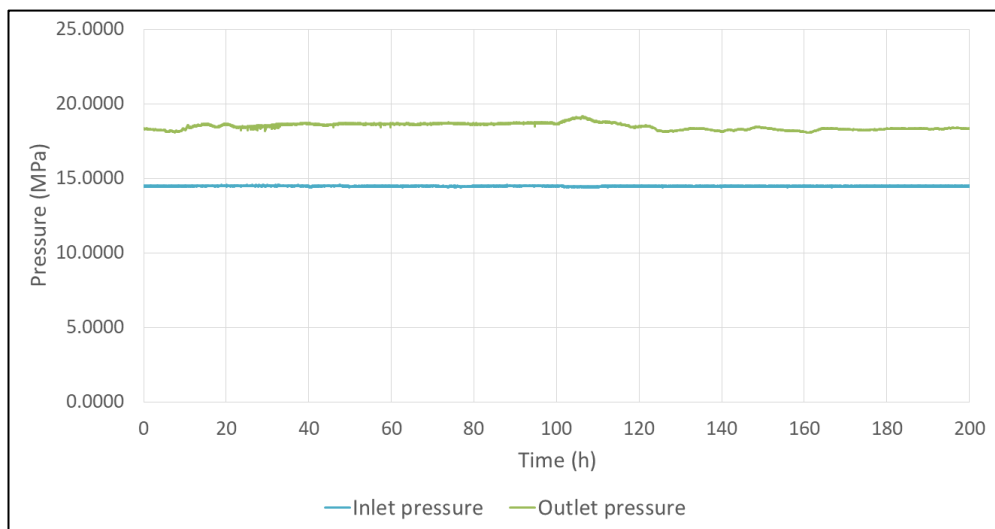
Figure 90. Pressure process data of the normal operation case.
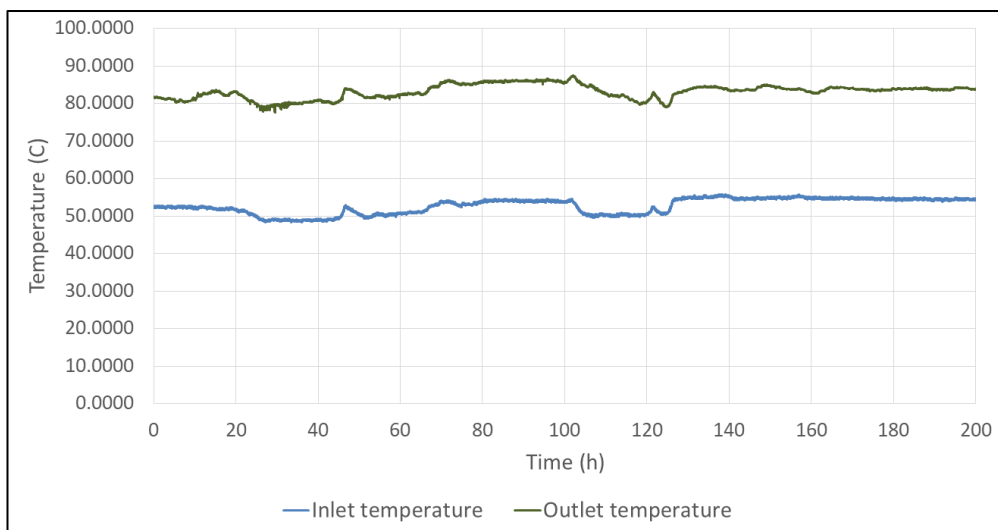
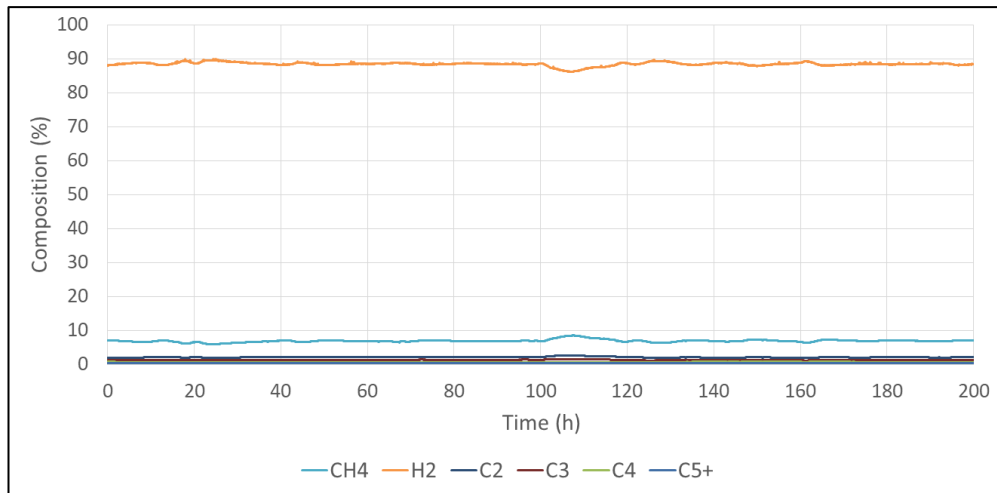Figure 91. Temperature process data of the normal operation case.

115

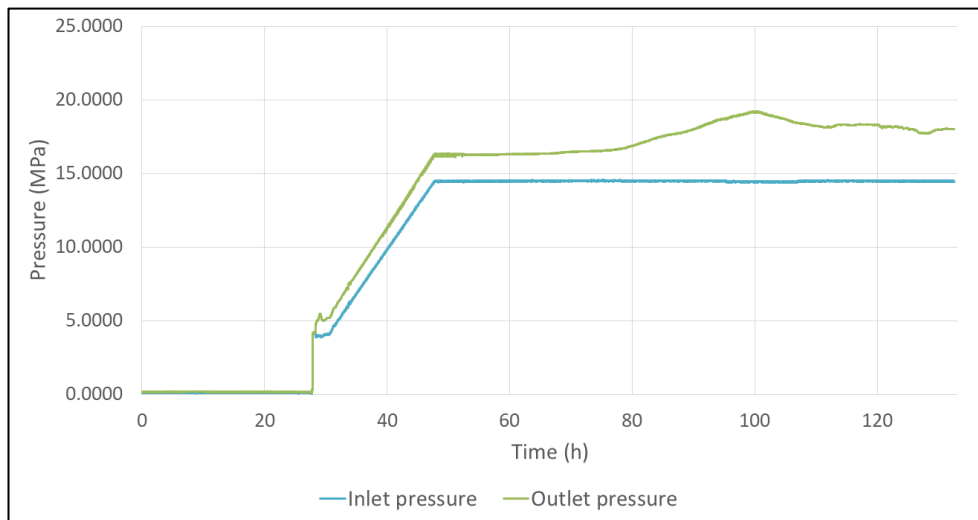Figure 92. Composition process data of the normal operation case.

Figure 93. Pressure process data of the startup case.
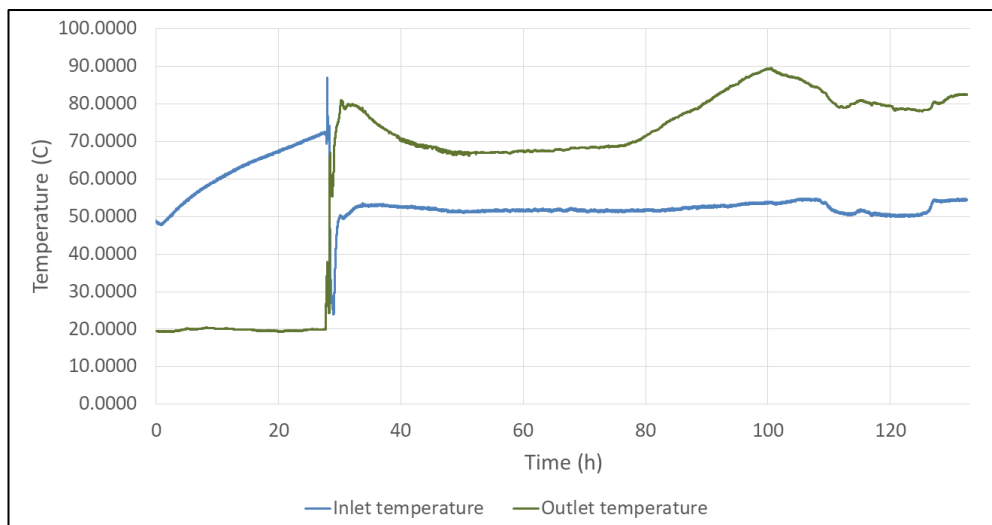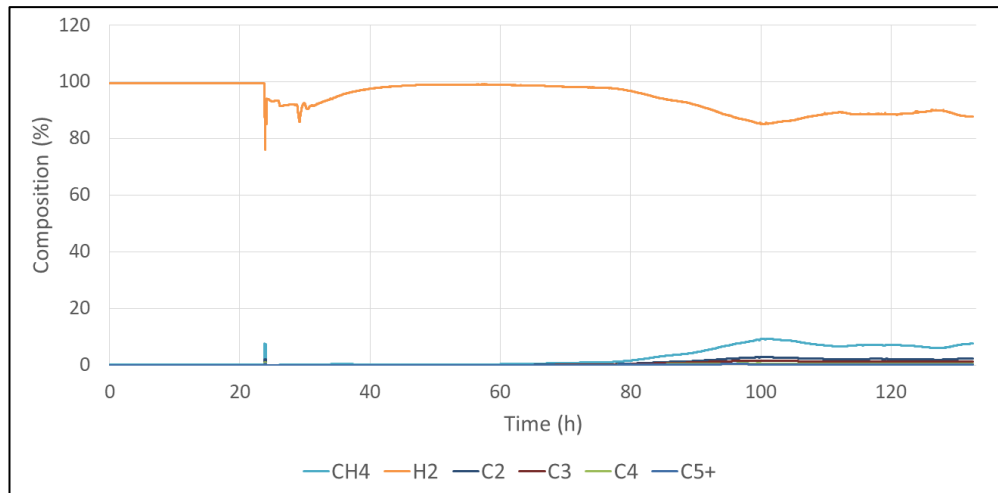

Figure 94. Temperature process data of the startup case.

Figure 95. Composition process data of the startup case.